Acute and Chronic Cellular Effects of Systemic Inflammation on the Central Nervous System

Dissertation

zur Erlangung des Doktorgrades (PhD)

der Medizinischen Fakultät

der Rheinischen Friedrich-Wilhelms-Universität

Bonn

Tatsuya Manabe

aus Nagoya, Japan

2021

Angefertigt mit der Genehmigung

der Medizinischen Fakultät der Universität Bonn

1. Gutachter: Prof. Dr. med. Michael T. Heneka

2. Gutachter: Prof. Dr. Martin Korte

Tag der Mündlichen Prüfung: 19 August 2021

Aus der Klinik für Neurodegenerative Erkrankungen

Direktor: Prof. Dr. med. Michael T. Heneka

Abstract

Sepsis-associated encephalopathy represents an acute cerebral dysfunction caused by systemic inflammation associated with sepsis. Emerging evidence suggests that these neurological complications are common in patients with sepsis at the time of hospital presentation and in elderly patients who survive sepsis for several years after the initial onset of sepsis. However, previous preclinical studies reported mixed effects of systemic inflammation on neuronal and synaptic damage. Likely confounds of these findings are the use of juvenile mice and inconsistent use of bacterial strains of lipopolysaccharide (LPS). On this basis, we intraperitoneally injected LPS either from *Salmonella* or from *E. coli* into 14- to 16-month-old mice and compared acute and chronic neuroinflammatory responses and cerebral damages in the LPS-tolerated mice at 7 and 63 days post-injection (dpi). Our data suggested that LPS could induce neuroinflammatory responses in aged mice for more than a week, and the extent of neuroinflammation tended to be higher after the *E. coli* LPS injection than upon a challenge by the *Salmonella* LPS injection. Cerebral damages caused by LPS injections, however, seemed to be mild because the neuron density in the hippocampus and global synaptic protein levels were found to indistinguishable from the controls at 7 dpi and 63 dpi. We also presented that both LPS serotypes led to a delayed reduction of excitatory, but not inhibitory, synaptic puncta in the CA3 subfield of the hippocampus at 63 dpi. We postulated that this local synapse loss in CA3 might increment the inhibitory tone of the Schaffer collaterals and a gradual decline of the neuronal activity in the CA1 apical dendrites. Furthermore, when the complement tagging at synapses was studied, both C3-coated synapses and synaptic C3 were reduced only in the area CA3. Because our histological analysis did not reveal the enhancement of synaptic pruning by microglia in CA3 at 7 dpi and 63 dpi, these results may indicate that our analysis of synaptic pruning was too late to detect the changes that caused the CA3 synapse loss.

Accumulating evidence suggests that several complement-independent molecular mechanisms exist for synaptic pruning by microglia. One of these pathways is the triggering receptor expressed on myeloid cells 2 (TREM2) pathway. Notably, loss of synapse is one of the earliest pathological hallmarks in Alzheimer's disease (AD), and

the animal models recapitulate the synaptic destruction from the early stage of disease progression. The roles of microglia in synapse loss via synaptic pruning have been recently found, and the loss-of-function mutation of the *TREM2* gene can increase the onset of sporadic AD. However, it remains unclear whether the absence of functional TREM2 proteins can modify the synapse pathology in APP/PS1 mice. To this end, using a T66M loss-of-function mutation of the *Trem2* gene (associated with the frontotemporal dementia-like syndrome), we found that the T66M mutation reduced the Aβ plaque load but incremented the oligomer levels in the cortex of 12-month-old APP/PS1 mice. These results indicated that *Trem2*-mutated microglia failed to compact the Aβ plaques, allowing for spreading the potentially synaptotoxic oligomeric Aβ in the cortex. Yet, our data also demonstrated that the synaptic puncta density was higher if APP/PS1 mice harboured this *Trem2* mutation. This highlighted the possibility that synaptic pruning by microglia was impeded during the disease progression.

Table of Contents

List of Abbreviations

Abe, abequose;

AD, Alzheimer's disease;

AKI, acute kidney injury;

AMPA, α-amino-3-hydroxy-5-methyl-4-isoxazole propionic acid;

ANOVA, analysis of variance;

APP, amyloid precursor protein;

ASC, apoptosis-associated speck-like protein containing a C-terminal caspase recruitment domain;

AU, arbitrary unit;

BBB, blood-brain barrier;

BCA, bicinchoninic acid;

BDNF, brain-derived neurotrophic factor;

BSA, bovine serum albumin;

C3R, C3 receptor;

C5aR, C5a anaphylatoxin receptor;

CAM-ICU, confusion assessment method for the intensive care unit;

CIs, confidence intervals;

CKD, chronic kidney disease;

CLP, caecal ligation and puncture;

CLRs, C-type lectin receptors;

CMV, cytomegalovirus;

CNS, central nervous system;

Col, colitose;

CRP, C-reactive protein;

CSF, cerebrospinal fluid;

CSF1R, colony stimulating factor 1 receptor;

CTCF, corrected total cell fluorescence;

CXCL, C-X-C motif chemokine ligand;

DAMPs, damage-associated molecular patterns;

DAP12, DNAX-activating protein of 12 kDa;

DG, dentate gyrus;

DPBS, Dulbecco’s phosphate-buffered saline;

dpi, days post-final injection;

DSM-5, diagnostic and statistical manual of mental disorders;

EAE, experimental autoimmune encephalomyelitis;

EBV, Epstein-Barr virus;

EEG, electroencephalography;

ELISA, enzyme-linked immunosorbent assay;

FER, Fps/Fes related tyrosine kinase;

FFU, focus forming unit;

FTD, frontotemporal dementia;

Gal, galactose;

GalNAc, *N*-acetyl-glucosamine;

GCS, Glasgow coma scale;

GFAP, glial fibrillary acidic protein;

Glc, glucose;

GlcNAc, *N*-acetyl-glucosamine;

GPR56, G protein-coupled receptor 56;

GWAS, genome-wide association study;

HIF-1, hypoxia-inducible factor 1;

HMGB1, high-mobility group box 1;

HR, heart rate;

HSV, herpes simplex virus;

i.p., intraperitoneal;

ICU, intensive care unit;

IFN, interferon;

IL, interleukin;

IQR, interquartile range;

Kdo, keto-deoxyoctulosonate;

LPS, lipopolysaccharide;

LTP, long-term potentiation;

Man, mannose;

MAP, mean arterial pressure;

MAPT, microtubule-associated protein tau;

MCI, mild cognitive impairment;
MDSCs, myeloid-derived suppressor cells;
mo, months old;
MODS, multiple organ dysfunction syndrome;
MOG, myelin oligodendrocyte glycoprotein;
MPO, myeloperoxidase;
MRI, magnetic resonance imaging;
MyD88, myeloid differentiation factor 88;
NF-κB, nuclear factor-κB;
NFTs, neurofibrillary tangles;
NLRP3, nucleotide-binding domain, the leucine-rich repeat, and the pyrin domain containing protein 3;
NLRs, nucleotide-binding and oligomerisation domain-like receptors;
NMDA, N-methyl-D-aspartate;
NO, nitric oxide;
O-Ac, O-acetylation;
PAMPs, pathogen-activated molecular patterns;
PBS, phosphate-buffered saline;
PBST, PBS with Triton X-100;
PET, positron emission tomography;
PFA, paraformaldehyde;
PICS, persistent inflammation, immunosuppression and catabolism syndrome;
Poly(I:C), polyinosinic-polycytidylic acid;
PRRs, pattern recognition receptors;
PS, phosphatidylserine;
PSD95, postsynaptic protein density 95;
PSEN1, presenilin 1;
PV, parvalbumin;
Rha, rhamnose;
RIPA, radioimmunoprecipitation assay;
ROS, reactive oxygen species;
SAE, sepsis-associated encephalopathy;
SARS-CoV-2, severe acute respiratory syndrome coronavirus type 2;

SASP, senescence-associated secretory phenotype;

SEM, standard error of measurement;

SIRS, systemic inflammatory response syndrome;

SIRT2, sirtuin 2;

SNPs, single nucleotide polymorphisms;

SOFA, sequential organ failure assessment;

sPD-L1, soluble programmed death ligand-1;

SV2A, synaptic vesicle glycoprotein 2A;

TBST, Tris-buffered saline with Tween-20;

TLRs, Toll-like receptors;

TNF, tumour necrosis factor;

TREM2, triggering receptor expressed on myeloid cells 2;

TSPO, translocator protein;

TUNEL, terminal deoxynucleotidyl transferase dUTP nick end labelling;

UPS, ubiquitin-proteasome system;

VGAT, vesicular GABA transporter;

VGLUT2, vesicular glutamate transporter 2.

Chapter 1: Introduction

1.1 An introduction to the study

In 2016, a new definition of sepsis was introduced as the third international consensus definitions for sepsis and septic shock ('Sepsis-3' criteria) and defined sepsis as "life-threatening organ dysfunction caused by a dysregulated host response to infection" (Singer *et al.* 2016b). Compared with the previous definitions (introduced as Sepsis-1 criteria in 1991 (Bone *et al.* 1992) and Sepsis-2 criteria in 2001 (Levy *et al.* 2003)), this novel definition abandons systemic inflammatory response syndrome (SIRS) (characterised by tachycardia, fever/hypothermia, tachypnoea and an abnormal number of leukocytes) and places greater importance on the organ dysfunction as measured by the sequential organ failure assessment (SOFA) (Vincent *et al.* 1996). Sepsis is imposing a significant burden on the healthcare system worldwide because 49 million individuals were affected by sepsis, and 11 million patients died from sepsis in 2017 (Rudd *et al.* 2020). In parallel, the age-standardised mortality rate gradually declined from 1990 to 2017 with a concomitant increase in the number of sepsis survivors (Rudd *et al.* 2020), indicating that improved quality of guidelines and cares helps to reduce mortality in patients with sepsis. However, evidence is accumulating for the long-lasting effects of sepsis among survivors because about half of those survivors (56% of them are over 65 years old) develop new functional impairments (Prescott and Angus 2018) and the inflammatory mediators in the plasma are found to be higher than those who have never developed sepsis for up to one year (Yende *et al.* 2019). Such functional impairments include neurological symptoms affecting memory and attention (Widmann and Heneka 2014). Given that the central nervous system (CNS) is no longer regarded as an immune-privileged organ (Louveau *et al.* 2015), it seems reasonable to speculate that the innate immunity in the CNS is chronically affected for more than a month after the sepsis. This phenomenon requires new research which investigates long-term consequences of sepsis on peripheral organs and the CNS using relevant animal models, samples derived from patients and clinical information.

1.2 Long-term sequelae of sepsis

1.2.1 Acute phase: Cytokine storm

Many kinds of pathogenic infections can cause sepsis in humans. A large-scale seminal work in the United States (n=10,319,418) from 1979 to 2001 showed that bacterial infection represents almost all the cases of sepsis (90%) (consisting 52% of gram-positive bacterial infection and 38% of gram-negative bacterial infection) with 4.7% of polymicrobial infection and 4.6% of fungal infection (Martin *et al.* 2003). However, it should be noted that many (73%) of the cohort in this study did not meet the current Sepsis-3 criteria due to the absence of organ failure and did not consider viruses to be a causative pathogen of sepsis. In contrast, the importance of viral sepsis has been suggested by a recent study in Southeast Asia (n=815, 56% of the study cohort meeting the Sepsis-3 criteria), and the investigators found that bacterial infections account for 72% of all the detected pathogens, whereas viral infections for 32% and co-infections for 7.5% (Southeast Asia Infectious Disease Clinical Research Network 2017). Of note, commonly detected viruses in this study were Dengue virus and influenza virus (accounting for 54% and 16% of all the detected viruses, respectively) (Southeast Asia Infectious Disease Clinical Research Network 2017). More recently, severe acute respiratory syndrome coronavirus type 2 (SARS-CoV-2) can also cause viral sepsis in 59% of hospitalised patients with severe COVID-19 (n=191) (Zhou *et al.* 2020). Therefore, it is becoming increasingly clear that some portion of patients with sepsis is caused by viral infections, which used to be overlooked by both clinical and preclinical researchers (Lin *et al.* 2018).

As an initial immune response to these infections, excessive inflammation, a so-called cytokine storm, is induced in patients with sepsis (**Fig. 1A**). This is characterised by excess production of proinflammatory cytokines, acute phase proteins and chemokines (for example, interleukin (IL)-1β, IL-6, interferon (IFN)-γ, tumour necrosis factor (TNF), complement factors, C-reactive protein (CRP), C-X-C motif chemokine ligand (CXCL)) (Fajgenbaum and June 2020). This is orchestrated by the activation of pattern recognition receptors (PRRs) for pathogen-activated molecular patterns (PAMPs) and damage-associated molecular patterns (DAMPs), including but not restricted to Toll-like receptors (TLRs) and nucleotide-binding and oligomerisation domain-like receptors (NLRs), and the consequent activation of the innate immune

system (Hotchkiss *et al.* 2016). Cytokine storm should be an immediate event within minutes after DAMPs or PAMPs activation (Hotchkiss *et al.* 2016) and cause fever, leucocytosis, multiple organ failure syndromes (MODS) and coagulation abnormality in patients (Fajgenbaum and June 2020). Paradoxically, cytokine storm does not threaten the lives of many patients with sepsis because less than 10% of all the patients die during this acute phase (Hawkins *et al.* 2018). At the same time — instead of in the next phase of sepsis — suppression of the immune system progressively increases (**Fig. 1A**), and it is believed that this immunosuppression contributes to hampering the onset of the additional cytokine storms caused by infections after the sepsis onset (Hotchkiss *et al.* 2016).

1.2.2 Chronic phase: PICS

Whilst half of the patients with sepsis who survive the cytokine storm completely recover, the other patients develop a chronic illness lasting for more than a year (**Fig. 1A**) (Prescott and Angus 2018; Stortz *et al.* 2018). This chronic condition seen in patients with sepsis after the intensive care unit (ICU) discharge is denoted as persistent inflammation, immunosuppression and catabolism syndrome (PICS) and characterised by prolonged mild inflammation, a moderate immune suppression or both of these immune alterations (Gentile *et al.* 2012). This first introduction of PICS and a more recent follow-up study demonstrated that the sustained inflammation is associated with the elevated levels of proinflammatory proteins in the plasma (for instance, IL-6, IL-8 and CRP) compared with the healthy controls and the expansion of myeloid-derived suppressor cell (MDSC) population for 28 days after the sepsis onset (Stortz *et al.* 2018; Gentile *et al.* 2012). In contrast, the immunosuppression is evidenced by higher levels of immunosuppressive proteins (for example, soluble programmed death ligand-1 (sPD-L1) and IL-10) than the healthy controls and lymphopaenia for more than 21 days after the sepsis onset (Stortz *et al.* 2018; Gentile *et al.* 2012). A recent one-year longitudinal follow-up of sepsis survivors also showed that CRP and sPD-L1 levels in the serum reduced from the initial cytokine storm but stayed at higher levels than the healthy controls for a year (Yende *et al.* 2019). In particular, IL-6 showed a unique inflammatory signature in 74% of these survivors because IL-6 levels in this group of survivors started to increase at 3 months after the initial hospital admission, continuing to raise until 12 months post-sepsis (Yende *et al.*

2019). In addition, sepsis survivors are frequently readmitted to the hospital because of recurrence of sepsis (Prescott *et al.* 2015) and present the increased risk of fungal infections, opportunistic bacterial infections (Hotchkiss *et al.* 2009) and reactivation of latent viruses (such as Herpes simplex virus (HSV), Epstein-Barr virus (EBV) and cytomegalovirus (CMV)) (Walton *et al.* 2014). All of these findings support the suppressed immune system among sepsis survivors after discharge from the hospital or ICU. The underlying molecular or epigenetic mechanisms remain elusive, but one highlighted pathway based on transcriptomic analysis of leukocytes and monocytes from immunosuppressive patients with sepsis is the hypoxia-inducible factor 1 (HIF-1) pathway (Davenport *et al.* 2016; Shalova *et al.* 2015).

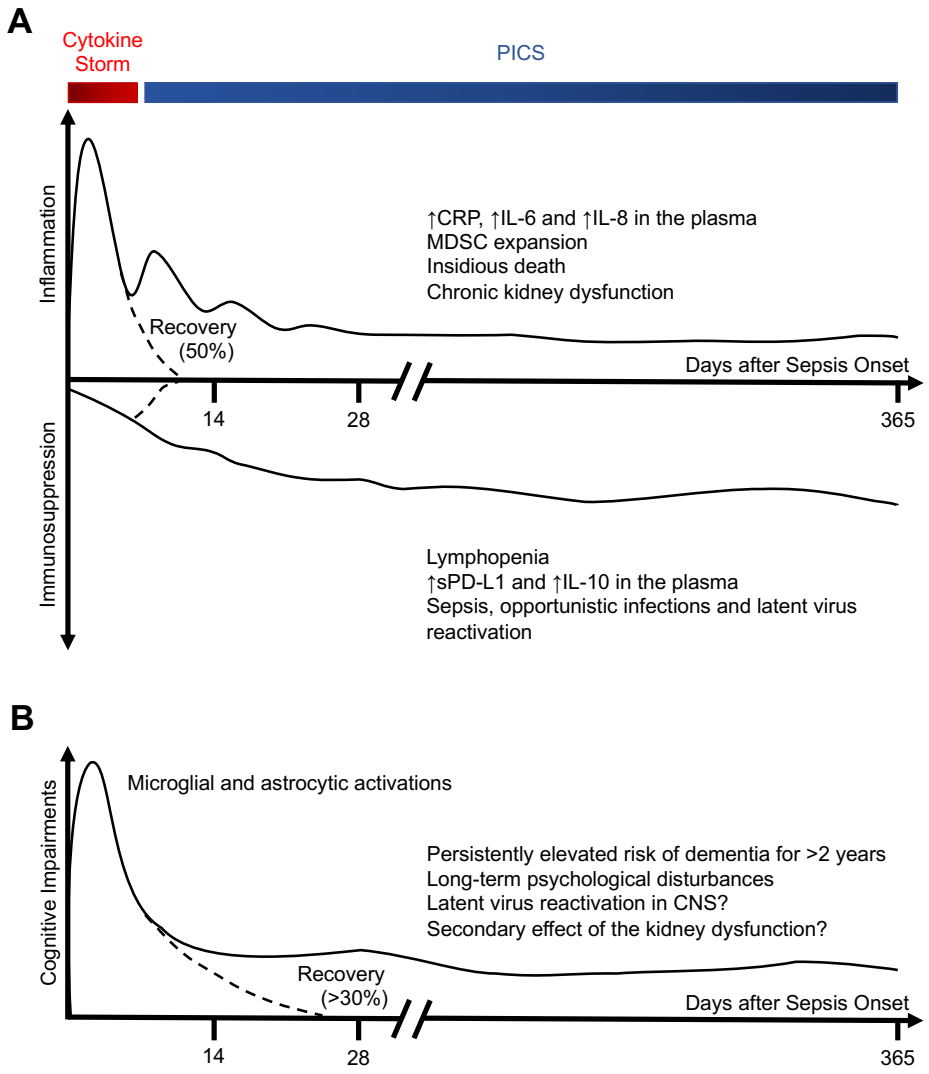

Figure 1. Clinical trajectory of sepsis and sepsis-associated encephalopathy.
(See figure legend on next page.)

(A) Acute and long-lasting changes in the immune profiles after the onset of sepsis. Excessive inflammation (cytokine storm) in the periphery is initially triggered after the infections by various pathogens (most commonly, bacteria and viruses). Half of the patients with sepsis who survive the initial cytokine storm develop chronically altered inflammatory conditions (known as PICS) with increased mortality for a year (Stortz *et al.* 2018; Gentile *et al.* 2012). PICS is characterised by the sustained peripheral inflammation (elevated levels of peripheral proinflammatory mediators (such as CRP, IL-6 and IL-8) and MDSC expansion) and the progressive increase in the immunosuppression (elevated levels of the immune suppressive mediators (such as sPD-L1 and IL-10), lymphopaenia and increased risk of infections and latent viral reactivation) (Stortz *et al.* 2018; Yende *et al.* 2019; Gentile *et al.* 2012; Prescott *et al.* 2015).
(B) A model of changes in the cognitive functions after sepsis. Many sepsis patients present delirium and coma at ICU, and some appear to recover from these neurological symptoms (Fritze *et al.* 2021; Yang *et al.* 2011). However, the rest show prolonged cognitive impairments for several years after the onset (Iwashyna *et al.* 2010; Yang *et al.* 2011; Shah *et al.* 2013; Fritze *et al.* 2021).
Abbreviations: CRP, C-reactive protein; CNS, central nervous system; ICU, intensive care unit; IL, interleukin; MDSC, myeloid-derived suppressor cell; PICS, persistent inflammation, immunosuppression and catabolism syndrome; sPD-L1, soluble programmed death ligand-1.

1.3 Sepsis-associated encephalopathy from a clinical perspective

1.3.1 Definition of sepsis-associated encephalopathy

A landmark study led by Eidelman *et al.* described the neurological abnormalities in patients with sepsis and defines sepsis-associated encephalopathy (SAE) as acute cerebral dysfunctions characterised by delirium and coma following the onset of sepsis without evidence for CNS infection by pathogens (Eidelman *et al.* 1996). Despite there being no diagnostic guideline of SAE as of now, frequently used methods to determine SAE in the research settings is either DSM-5 (diagnostic and statistical manual of mental disorders) or CAM-ICU (confusion assessment method for the intensive care unit) to diagnose delirium (Inouye *et al.* 2015) and Glasgow coma scale (GCS) to measure the levels of a patient's consciousness (Eidelman *et al.* 1996).

1.3.2 Progressive changes in cognitive disturbances

The incidence of SAE in patients with sepsis is high at the time of ICU admission, but accumulating epidemiological analyses suggested that the changes in the cognitive functions seemed to be dynamic after the onset of sepsis (**Fig. 1B**). A large-scale multicentre analysis (n=2,513) showed that about half (53%) of patients with sepsis displayed SAE at ICU (Sonneville *et al.* 2017), confirming the initial study of SAE (Eidelman *et al.* 1996). As the definition of delirium implies the reversibility of SAE (namely, acute disturbances of awareness, attention and cognition lasting for hours to days) (Inouye *et al.* 2015), another study found that more than one-third (37%) of patients with sepsis exhibited recovery from the neurological symptoms within a month after the onset of sepsis (Yang *et al.* 2011). A recent retrospective analysis using the German health claims data of patients with sepsis (n=161,567) provided further insight on the trajectory of cognitive functions over time (Fritze *et al.* 2021). When the investigators examined the incidence of dementia diagnosis for more than six years after the onset of sepsis, they found that diagnosis of dementia was peaked at the time of sepsis onset but sharply declined within the next six months (Fritze *et al.* 2021). Nevertheless, a striking difference was noted among patients who were older than 85 years old because this elderly group of survivors displayed an elevated incidence of dementia for two years after the initial diagnosis of sepsis (Fritze *et al.* 2021). This finding is consistent with the earlier US Health and Retirement Study (n=1,194) and the subgroup analysis of Cardiovascular Health Study (n=198). These studies reported that the risk of developing cognitive impairments and dementia was higher in patients who survived sepsis than in patients hospitalised for the other causes, and this difference was observed for up to ten years after the initial hospital admission (Iwashyna *et al.* 2010; Shah *et al.* 2013). Of note, which type(s) of dementia are more susceptible to the survivors require further investigations, and the reasons why some, but not all, patients with sepsis recover SAE will need to be explored in the future. One possible way to approach this question might be a genome-wide association study (GWAS). Notably, a previous GWAS study did identify that survival from sepsis is associated with the single nucleotide polymorphisms (SNPs) in the intronic region of the *FER* gene (which encodes Fps/Fes related tyrosine protein kinase), and patients with these SNPs increase their survival by 44% (Rautanen *et al.* 2015). Thus, it might be possible that there might be genetic relationships between the risk of developing SAE and genes associated with the survival from sepsis.

1.3.3 Frontal cortex and medial temporal lobe under the risk of sepsis

Evidence for the damages to the CNS in patients with sepsis is accumulating based on neuroimaging findings, abnormal electroencephalography (EEG) recordings and circulating biomarker changes in patients with SAE. For instance, general cerebral effects are evidenced by the frequent magnetic resonance imaging (MRI) findings of cytotoxic oedema in patients with SAE, which likely represents ischaemia and the consequent cellular damages (Stubbs *et al.* 2013). When 17 studies were systematically reviewed, EEG abnormalities (such as slowing of the delta wave and continuous theta wave) were also common in patients with SAE, suggesting the alterations of the neuronal activity following the onset of sepsis (Hosokawa *et al.* 2014). However, it should be noted that cognitively normal patients with sepsis can exhibit such abnormal EEG recordings, indicating that EEG findings are not specific to the onset of SAE (Hosokawa *et al.* 2014). When the serum biomarkers were assessed in ICU, S100B (a protein produced by astrocytes that indicates brain injury) was found to be higher in patients with SAE than in cognitively intact patients with sepsis (Wu *et al.* 2020).

Meanwhile, as the relevant cognitive domains are affected in patients with SAE, sepsis seems to damage specific brain regions, particularly the frontal cortex and medial temporal lobe. Previous studies of the affected cognitive domains in patients who survived sepsis suggested that spatial recognition memory (Andonegui *et al.* 2018), verbal learning and memory (Semmler *et al.* 2008), executive function and visual attention (Gunther *et al.* 2012) were impaired after the hospital discharge. In line with this, patients with SAE showed a reduced volume of the amygdala, hippocampus and cortex during the ICU stay (Orhun *et al.* 2020), and those who died from sepsis displayed apoptotic neurons in the amygdala, hypothalamus and medulla on a *post-mortem* investigation (Sharshar *et al.* 2004; Sharshar *et al.* 2003). Further, patients who survived from sepsis also showed a lower volume of the superior frontal cortex and hippocampus than patients who were admitted to ICU for other causes within two years after the hospital discharge (Semmler *et al.* 2013; Gunther *et al.* 2012). Although some studies reported conflicting findings using animal models (**Table 1**), these clinical data were corroborated by neuronal cell death observed in the hippocampus of rats (Semmler *et al.* 2007; Semmler *et al.* 2008) and mice following the induction of systemic inflammation (Lee *et al.* 2008).

Table 1. Cerebral dysfunction in mouse models of systemic inflammation.

Type of sepsis model	Specific bacterial component	Protocol	Age of mice	Brain pathology observed	Reference
Gram-negative bacterial infection	*E. coli* O55:B5 LPS	8 mg/kg via i.p. route	2 months	Impaired spatial memory and transient reduction of NMDA and AMPA receptor expression without neuronal cell death in the hippocampus	(Zhang *et al.* 2017)
	E. coli O55:B5 LPS	1 mg/kg via i.p. route on 4 consecutive days	2-3 months	Normal neuron and synapse density in the hippocampus	(Chen *et al.* 2012; Chen *et al.* 2014)
	E. coli O55:B5 LPS	0.25 mg/kg via i.p. route on 7 consecutive days	Unknown	Neuronal apoptosis in the CA1 region of the hippocampus	(Lee *et al.* 2008)
	E. coli O127:B8 LPS	5 mg/kg via i.p. route	5 months	Increased working memory errors and chronic reduction of synaptic proteins without neuronal cell death in the hippocampus at two months post-injection	(Weberpals *et al.* 2009)
	Unknown	5 mg/kg via i.p. route	2 months	Impaired spatial memory at a month, but not at a week, post-injection with the impaired hippocampal neurogenesis	(Ormerod *et al.* 2013)
	E. coli O127:B8 LPS	0.2 mg/kg via i.p. route on 2	7 months (young) and 19	Normal dendritic spine density in the hippocampus of	(Beyer *et al.* 2020)

	and *Salmonella enterica* LPS	consecutive days	months (aged)	young mice but chronic reduction in the aged mice	
Gram-positive bacterial infection	*S. pneumoniae*	OD600 = 0.63, via intratracheal route	1-2 months	Monocyte infiltration to the brain and chronic spatial memory deficits	(Andonegui *et al.* 2018)
Polymicrobial sepsis	Caecal contents	Caecal ligation and puncture	1-2 months	Long-term spatial memory deficits and reduced dendritic spine density in the CA1 region	(Chavan *et al.* 2012)
			1-2 months	Long-term impairments of contextual fear conditioning and reduced dendritic spine density in the amygdala and dentate gyrus, but not CA1, of the hippocampus	(Huerta *et al.* 2016)
			1-2 months	Persistently impaired extinction of fear conditioning and monocyte infiltration without dendritic spine loss or neuronal cell death	(Singer *et al.* 2016a)
Viral infection	Influenza A virus subtypes H3N2	10 FFUs via intranasal route	2-3 months	Impaired spatial memory and temporal reduction of dendritic spine density in the hippocampus at 30 days post-infection	(Hosseini *et al.* 2018)
	Poly(I:C)	5 mg/kg via i.p. route	1-2 months	Impaired motor learning after the	(Garré *et al.* 2017)

				rotarod training and the elevated rate of dendritic spine elimination in the motor cortex *in vivo*	

Abbreviations: AMPA, α-amino-3-hydroxy-5-methyl-4-isoxazole propionic acid; FFU, focus forming unit; i.p., intraperitoneal; LPS, lipopolysaccharide; NMDA, N-methyl-D-aspartate; poly(I:C), polyinosinic-polycytidylic acid.

1.4 Cerebral damages caused by sepsis

1.4.1 Evidence for the induction of neuroinflammation

Following the onset of sepsis, the innate immune system is activated by circulating immune mediators that can cross the blood-brain barrier (BBB) (Dantzer and Kelley 2007) without neuroinvasion of the bacteria and viruses that cause sepsis (Sonneville *et al.* 2013). Subsequently, as murine models of systemic inflammation suggest, activated microglia, astrocytes and endothelial cells produce various inflammatory proteins (such as IL-1β, IL-6, nitric oxide (NO) and TNF) in the brain (Widmann and Heneka 2014). This microglial activation is inferred by the less ramified morphology of microglia with the increased CD68 immunoreactivity in the brains of deceased patients with sepsis (Zrzavy *et al.* 2019; Lemstra *et al.* 2007). Recent technical advancement of positron emission tomography (PET) imaging allows us to longitudinally observe the occurrence of neuroinflammation via a radioactively labelled glial translocator protein (TSPO) (such as [^{18}F]FEPPA and [^{11}C]PBR28) (Sandiego *et al.* 2015; Chang *et al.* 2021). Using these methods, systemic injection of lipopolysaccharide (LPS) (a well-known gram-negative bacterial cell wall component) into healthy human volunteers at low doses or rodents at high doses resulted in global increases in the TSPO signals (that is, microglial and astrocytic activations) across the brain regions (Sandiego *et al.* 2015; Chang *et al.* 2021). This provides unambiguous evidence for the induction of neuroinflammation after the systemic inflammation without the brain infection and indicates that the brain regions commonly affected by sepsis (i.e. the medial temporal lobe and frontal cortex) may not be attributed to different degrees of neuroinflammation in these brain regions.

1.4.2 Elevated cytokines in the brain and their effects on the cognition

Altered cognition in patients with sepsis may result from cytokine toxicity in the brain. This is because (1) various proinflammatory cytokines (such as TNF, IL-1β and IL-6) can modulate learning and memory in mice and humans (Yirmiya and Goshen 2011), and (2) peripheral IL-6 levels are elevated immediately after onset and during the recovery of sepsis (Yende *et al.* 2019). Notably, many pieces of previous literature suggested an association of circulating IL-6 levels with cognitive impairments in humans. For instance, higher IL-6 levels were detected when the individuals presented age-dependent cognitive decline when the same individuals were followed up for ten years (Singh-Manoux *et al.* 2014). Others found that IL-6 levels were correlated with the impaired episodic memory in healthy individuals who had been challenged with low doses of LPS (Reichenberg *et al.* 2001). In patients with sepsis at ICU, elevated IL-6 levels were detected in those cognitively impaired patients compared with cognitively normal patients (Wu *et al.* 2020). Similar observations were also documented in hospitalised patients with delirium associated with non-sepsis causes (for example, hip fracture surgery) (van Munster *et al.* 2008; de Rooij *et al.* 2007). Intriguingly, patients with delirium symptoms for eight days displayed that the peripheral cytokine levels were normalised at an earlier point of time (van Munster *et al.* 2008). This indicated that the initial increase of IL-6 may be sufficient for impairing cognitive functions in patients with delirium or SAE. Alternatively, despite the normal levels in the blood circulation, the elevated levels of IL-6 may persist, thereby disturbing the cognitive functions of the patients. The importance of IL-6 was further confirmed in animal models showing that IL-6 deficiency rescued the onset of endotoxin-induced spatial memory deficits without affecting the TNF and IL-1β increase in the plasma (Sparkman *et al.* 2006). Although it remains largely unknown how IL-6 negatively affects the cognitive functions in humans and mice, it seems plausible that proinflammatory cytokines, particularly IL-6, can induce cognitive disturbances.

1.4.3 Synaptic alterations after sepsis

Cerebral damages and the consistent cognitive disturbances following sepsis may be a consequence of loss of synapses because the abundance of synapses in the brain strongly correlate with cognitive functions across the species. For instance, patients

with mild cognitive impairment (MCI) and Alzheimer's disease (AD) displayed loss of synapses in the hippocampus (Terry *et al.* 1991; Scheff *et al.* 2007; Vanhaute *et al.* 2020). Likewise, synapse loss is found in the hippocampus of aged mice and frontal cortex of aged non-human primates, significantly correlated with behaviours indicating the memory deficits (Shi *et al.* 2015; Dumitriu *et al.* 2010). Animal models of bacterial and viral sepsis demonstrated that systemic inflammation (for example, endotoxin challenge, viral dsRNA injection (namely, polyinosinic-polycytidylic acid (poly(I:C)), influenza virus A infection) contributed to declining the synapse density in the brain (Weberpals *et al.* 2009; Zhang *et al.* 2017; Beyer *et al.* 2020; Hosseini *et al.* 2018; Garré *et al.* 2017; Chavan *et al.* 2012) (**Table 1**). Although some claimed the reversible changes of synapse density within a week (Zhang *et al.* 2017), others found a chronic reduction lasting for more than a month (Weberpals *et al.* 2009; Beyer *et al.* 2020; Hosseini *et al.* 2018). This suggested that if the number of synapses decreases following the onset of sepsis, synapse loss may persist for several months and contribute to developing sustained cognitive impairments as observed in patients who survived sepsis (Fritze *et al.* 2021).

However, to our best knowledge, studies about cerebral damages in patients with SAE at the levels of synapses are not available. A recent analysis of the cerebrospinal fluid (CSF) suggested that synapse-related proteins are downregulated in patients with delirium caused by infection (Peters van Ton *et al.* 2020). This study indicated the potential links of synapse degeneration to the cognitive alterations in patients with sepsis. To confirm this, future investigations are required for testing whether synapse loss might be induced over time in patients with sepsis and those who survive sepsis. Preferably, this should be analysed using a new PET tracer to visualise the number of synapses in living humans *in vivo.* This PET imaging method utilises a radiotracer for synaptic vesicle glycoprotein 2A (SV2A) (known as [^{11}C]UCB-J) (Nabulsi *et al.* 2016) and successfully detected the synapse loss in patients with epilepsy and MCI (Finnema *et al.* 2016; Vanhaute *et al.* 2020). This method allows the longitudinal observations in the same patients but also eliminates the potential confounding factors that can complicate the *post-mortem* analysis of synapses (such as *post-mortem* delay, the onset of the lethal MODS and premorbid pathology).

1.5 Endotoxin challenges to model the gram-negative bacterial infection

1.5.1 Heterogeneous structure of lipopolysaccharide

The biochemical compositions of LPS are highly varied, especially at O-antigen (that is, repeating units of three to five sugar units), and such a structural heterogeneity determines the bacterial serotypes (Lerouge and Vanderleyden 2002) (**Fig. 2**). Some studies found that distinct bacterial strains can produce varying degrees of inflammatory responses *in vitro* and *in vivo* as a result of activation of different signalling cascades (Netea *et al.* 2001; Kayagaki *et al.* 2013). Recently, serotype-related cerebral effects were also found, and these authors reported that *Salmonella* LPS injection in 16-month-old mice tended to show a greater loss of the dendritic spines in the CA1 hippocampal subfield and more severe induction of the long-term potentiation (LTP) deficits (at three months post-injection) than *E. coli* LPS (Beyer *et al.* 2020). To our knowledge, previous literature that examined the effects of different LPS serotypes is currently sparse, and the effects of endotoxin challenge on neurons and synapses are debated (**Table 1**). One possible explanation for this discrepancy might be the inconsistent use of different bacterial serotypes across studies, and standardisation of the injection paradigms is strongly encouraged in this field.

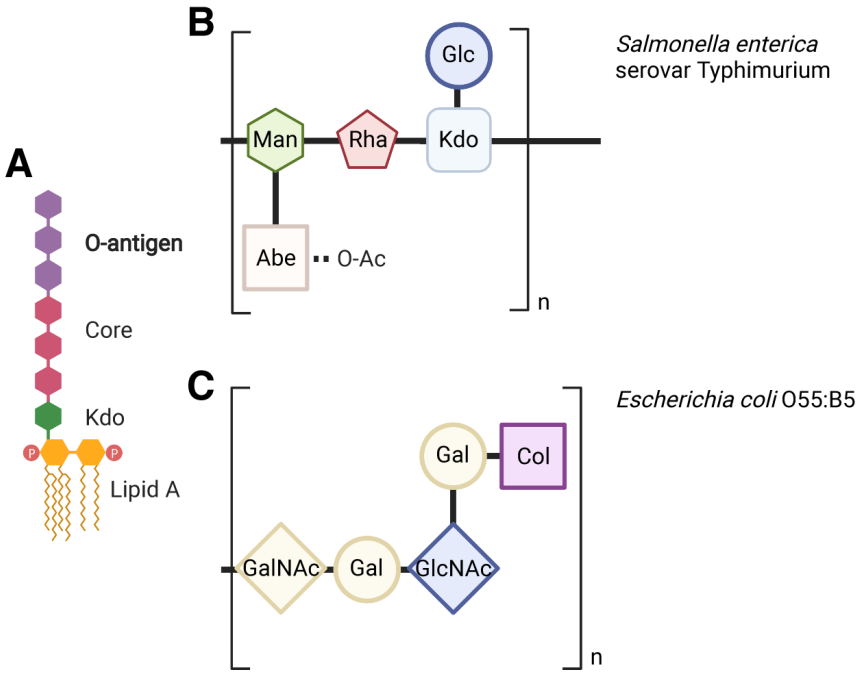

Figure 2. Structural heterogeneity of lipopolysaccharide.

(See figure legend on next page.)

(A) Schematic of the S ('smooth') LPS containing the O-antigen. The other type of LPS without O-antigen is known as R ('rough') LPS (Lerouge and Vanderleyden 2002).
(B, C) Heterogeneous chemical compositions of the repeating units at O-antigen of LPS. Structure of (B) *Salmonella enterica* serovar Typhimurium (Whitfield *et al.* 2020) and (C) *Escherichia coli* O55:B5 (Rodriguez-Loureiro *et al.* 2018) are shown as an example.
This figure was created using BioRender (https://biorender.com/).
Abbreviations: Abe, abequose; Col, colitose; Gal, galactose; GalNAc, *N*-acetyl-glucosamine; Glc, glucose; GlcNAc, *N*-acetyl-glucosamine; Kdo, keto-deoxyoctulosonate; LPS, lipopolysaccharide; Man, mannose; O-Ac, O-acetylation; Rha, rhamnose.

1.5.2 Systemic lipopolysaccharide injection as a model of sepsis

Endotoxin challenge has been widely used as an animal model of sepsis and the related systemic inflammation. One of the most compelling pieces of evidence that support the use of LPS to simulate sepsis is a case study of a middle-aged (unknown exact age of this patient) man who self-administered high doses (1 mg via intravenous route) of LPS and developed MODS (Taveira da Silva *et al.* 1993). At the hospital presentation, this patient showed a severe cardiovascular dysfunction (SOFA score of four), coagulation abnormality (SOFA score of two), respiratory dysfunction (estimated SOFA score of two) and renal dysfunction (SOFA score of one) (Taveira da Silva *et al.* 1993; Vincent *et al.* 1996). This indicated the onset of sepsis based on the current Sepsis-3 criteria, which requires a total SOFA score of at least two points (Singer *et al.* 2016b). Consistently, endotoxin injections into mice induced not only damages to the brain (**Table 1**) but also various peripheral organ failures at the same time, which include dysfunctions of the kidney (Ghaly *et al.* 2011), heart (Knuefermann *et al.* 2002) and lung (Parsey *et al.* 1998; Mullaly and Kubes 2006) (**Table 2**). This reflects that endotoxin injection recapitulates various pathology seen in patients with sepsis as animal models.

Table 2. Endotoxin injection as a mouse model of sepsis.

Specific bacterial component	Protocol	Age of mice	Pathology related to organ dysfunction [organs with the impaired functions]	Reference
E. coli O127:B8 LPS	3.5 mg/kg via i.p. route	4 months	[Kidney] Increased creatinine levels in the plasma and chronic renal fibrosis	(Ghaly *et al.* 2011)
E. coli O111:B4 LPS	25 mg/kg via i.p. route	2 months	[Heart] Reduced MAP and systemic vascular resistance; increased HR	(Knuefermann *et al.* 2002)
E. coli O111:B4 LPS	0.5-25 mg/kg via i.p. route	1-3 months	[Lung] Increased MPO activity	(Parsey *et al.* 1998; Mullaly and Kubes 2006)

Abbreviations: HR, heart rate; i.p., intraperitoneal; LPS, lipopolysaccharide; MAP, mean arterial pressure; MPO, myeloperoxidase.

1.6 Adult sepsis mostly affecting the elderly individuals

1.6.1 Adult sepsis mostly affecting the elderly individuals

While children and juvenile humans (younger than 18 years old) can develop sepsis (Southeast Asia Infectious Disease Clinical Research Network 2017), adult sepsis is common especially among elderly patients as the majority of adult survivors (56%) are older than 65 years old (Prescott and Angus 2018). This indicated that adult sepsis is an age-related disease. Similarly, cognitive disturbances are associated with the age of the patients with sepsis. A recent Fritze *et al*.'s (2021) study demonstrated that the incidence rate of dementia was higher in elderly patients aged older than 85 years both at the time of hospital presentation and for up to two years after the onset than in younger groups of patients (namely, patients aged at 65-74 years and 75-84 years). This suggested that age-related changes in the brain might act as predisposing factors of cerebral damages caused by sepsis.

1.6.2 Age-related neuron and synapse loss with a possible role of synaptic pruning

Ageing can affect neurons and synapses in the hippocampus of mice and affect their behaviours associated with the hippocampus-dependent memory. For instance, the number of neurons and synapses is reduced in the area CA3 of the hippocampus of

aged mice (at >16 months of age) (Shi *et al.* 2015; Linnartz-Gerlach *et al.* 2019). Consistently, age-related spatial memory deficits became apparent even earlier (at 8-12 months of age) (Shoji *et al.* 2016), and these behavioural changes were confirmed using 16-month-old mice (Shi *et al.* 2015). These data indicated that the CA3 neurons are highly vulnerable to ageing, thereby ultimately impairing the cognitive functions of rodents. Nonetheless, during the ageing of humans, a stereological analysis demonstrated that pyramidal cell density decreased in the hilus and subiculum, but not in the CA3 subfield (West 1993). This suggested that the recent data obtained from aged rodents may be less relevant for ageing of the human brains.

Notably, the complement pathway is associated with the age-dependent loss of CA3 neurons and synapses in mice, and the complement activation by systemic inflammation may worsen the neuronal and synaptic damages. Indeed, it is known that the complement pathway is progressively activated during normal ageing (Stephan *et al.* 2013; Shi *et al.* 2015) and robustly stimulated in the CNS following an endotoxin challenge in young mice (Li *et al.* 2020a; Jacob *et al.* 2007; Bodea *et al.* 2014). Deficiency of a complement factor C3 prevented age-related reductions of neurons and synapses in CA3, as well as deficits of LTP and behavioural changes at 16 months of age (Shi *et al.* 2015). Similarly, endotoxin-induced inhibitory synapse loss in CA3 of young mice was prevented by a prior treatment with C3 receptor (C3R) antagonist (Li *et al.* 2020a).

However, the exact molecular and cellular mechanisms that confer the CA3-specific vulnerability via C3 remain elusive. Because the complement pathway is frequently required for synaptic pruning by microglia during development and in the presence of additional pathology such as AD (Schafer *et al.* 2012; Hong *et al.* 2016), it is reasonable to assume that this mode of microglia-synapse interactions is involved in CA3 synapse loss, and sepsis might enhance the synaptic pruning by microglia (**Fig. 3A**). Recent studies found that phosphatidylserine (PS) needs to be exposed on the synaptic surface from the inner leaflet of the plasma membrane in order for microglia to determine and eliminate specific, weakened synapses (Scott-Hewitt *et al.* 2020; Li *et al.* 2020b). Given that this PS exposure is seen when primary neurons are exposed to LPS-stimulated microglia *in vitro* (Fricker *et al.* 2012), and that neuronal apoptosis (a potent inducer of PS exposure) has been documented following LPS injection in

rodents (Lee *et al.* 2008; Semmler *et al.* 2008), PS may be exposed following systemic inflammation *in vivo*. Consequently, PS on the synaptic surface recruits and condenses C1q proteins at synapses (Scott-Hewitt *et al.* 2020) which cleave C3 proteins (released by reactive astrocytes) into active forms (C3a and C3b) (Stevens *et al.* 2007). Finally, these C3 cleavage products activate C3R, expressed by microglia, leading to the induction of synaptic pruning by microglia (Schafer *et al.* 2012). Of note, several studies reported that C3 can also be accumulated at synapses (Hong *et al.* 2016; Shi *et al.* 2015), and it remains unclear what molecular mechanisms are involved in this C3 accumulation. Furthermore, microglia do not always rely on the complement pathway to remove synapses (Weinhard *et al.* 2018), and emerging evidence identified that the exposed PS is recognised by other microglial receptors (including triggering receptor expressed on myeloid cells 2 (TREM2) (Scott-Hewitt *et al.* 2020; Filipello *et al.* 2018) and G protein-coupled receptor 56 (GPR56) (Li *et al.* 2020b)).

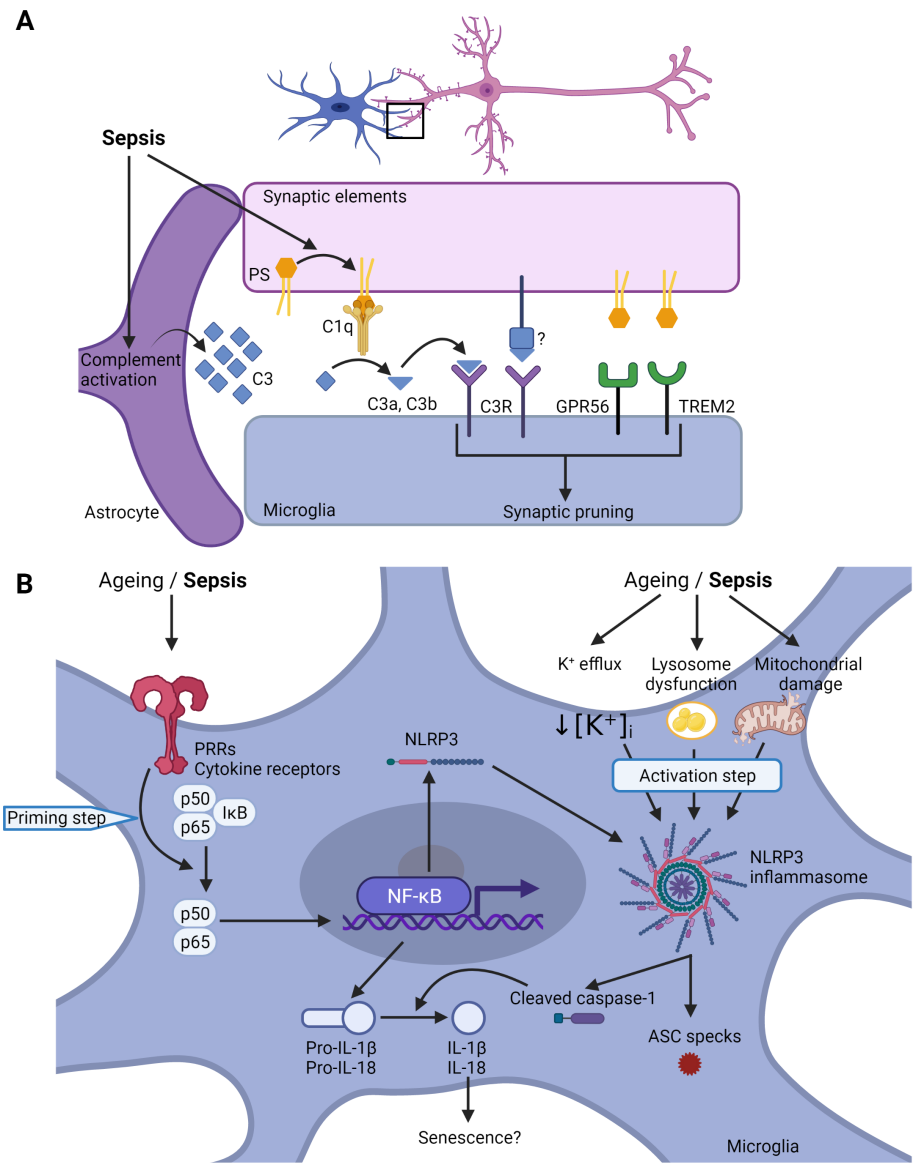

Figure 3. The complement and NLRP3 inflammasome pathways in microglia. **(A)** The complement pathway playing a role in synaptic pruning by microglia. Cytokine storm elicited by sepsis onset leads to the complement activation across the body, including in the brain (Li *et al.* 2020a). If phosphatidylserine (PS) is exposed on the outer synaptic membrane, C1q is recruited at synapses and induces synaptic pruning by microglia (Scott-Hewitt *et al.* 2020) likely via C3 cleavage and the consequent C3 receptor (C3R) activation on microglia (Stevens *et al.* 2007; Litvinchuk *et al.* 2018; Li *et al.* 2020a). Some studies also found C3 accumulation at synapses for unknown mechanisms (Hong *et al.* 2016; Shi *et al.* 2015). The exposed PS can also be recognised by other microglial receptors (such as GPR56 (Li *et al.* 2020b) and TREM2 (Scott-Hewitt *et al.* 2020)).

(B) The canonical NLRP3 inflammasome pathway activated by systemic inflammation and ageing via the priming and activation steps. The priming step involves activation of pattern recognition receptors (PRRs) and cytokine receptors by cytokine storm or age-related accumulation of DAMPs (Franceschi *et al.* 2017; Dantzer and Kelley 2007; Rivest 2009). This results in the nuclear translocation of nuclear factor κB (NF-κB), which in turn induces the transcription of the NLRP3 monomer, interleukin (IL)-1β precursor (pro-IL-1β) and IL-18 precursor (pro-IL-18) (He *et al.* 2016). The assembly of the NLRP3 inflammasome (activation step) requires additional signals, and the proposed signals during ageing and sepsis were: mitochondrial damages (Mecocci *et al.* 1993; Harland *et al.* 2020), K^+ efflux via P2X7 purinergic receptor and other signals (Muñoz-Planillo *et al.* 2013; Choi *et al.* 2007; Mingam *et al.* 2008) and lysosomal dysfunctions (Heneka *et al.* 2015; Marschallinger *et al.* 2020). Consequently, the NLRP3 inflammasome activates caspase 1 via its cleavage, which in turn produces IL-1β and IL-18 from pro-IL-1β and pro-IL-18, respectively (He *et al.* 2016). At the same time, the oligomerisation of ASC generates ASC specks (He *et al.* 2016).
This figure was created using BioRender (https://biorender.com/).
Abbreviations: ASC, apoptosis associated speck-like protein containing a caspase recruitment domain; DAMPs, damage-associated molecular patterns; GPR56, G protein-coupled receptor 56; NLRP3, NOD-, LRR- and pyrin domain-containing protein 3; TREM2, triggering receptor expressed on myeloid cells 2.

1.6.3 The NLRP3 inflammasome activation with a possible link to senescence

Ageing is associated with the imbalance of the proinflammatory and anti-inflammatory equilibrium across the body, thereby generating persistent, low-grade proinflammatory conditions (termed ‘inflammaging’) (Franceschi *et al.* 2007). This requires activation of the innate immune system partly orchestrated by the NOD-, LRR- and pyrin domain-containing protein 3 (NLRP3) inflammasome pathway (Franceschi *et al.* 2017). This is because NLRP3 deficiency prevented the onset of age-related cognitive, metabolic and motor dysfunctions, as well as glial activation in the hippocampus, in mice at 20-24 months of age (Youm *et al.* 2013).

In general, the canonical NLRP3 inflammasome pathway is divided into two steps: priming and activation step (**Fig. 3B**). The priming step is initiated once DAMPs and PAMPs activate PRRs (such as TLRs, NLRs and C-type lectin receptors (CLRs)) and cytokine receptors (such as IL-1 receptors and TNF receptors), usually located on the microglial or macrophage surface in the CNS (Venegas and Heneka 2017). This in turn activates the myeloid differentiation factor 88 (MyD88) and the nuclear factor κB (NF-κB) pathway (priming step), leading to the expression of cytokine precursors (such as pro-IL-1β and pro-IL-18) and NLRP3 monomer (He *et al.* 2016). The subsequent NLRP3 assembly requires additional signals (activation step), and various molecules are known to act as activation signals (as reviewed by He *et al.* (2016)). Such activation signals include a reduction of cytosolic K^+ concentration (caused by ATP (via activation of the purinergic P2X7 receptor), nigericin and bacterial pore-forming toxins) (Muñoz-Planillo *et al.* 2013) and mitochondrial reactive oxygen species (ROS) and oxidised mitochondrial DNA (caused by mitochondrial dysfunctions) (He *et al.* 2016). As a consequence, caspase-1 is cleaved and activated, leading to the maturation of IL-1β and IL-18 from the respective precursors (He *et al.* 2016). At the same time, apoptosis associated speck-like protein containing a caspase recruitment domain (ASC) protein is oligomerised as ASC specks (He *et al.* 2016).

Nevertheless, less is clear about how the NLRP3 inflammasome pathway contributes to inflammaging. The priming step during ageing is likely linked to a progressive accumulation of so-called 'molecular garbage' in the brain. Notably, the clearance mechanism of cell debris and misfolded proteins (such as autophagy and the ubiquitin-proteasome system (UPS)) gradually decline over time (Franceschi *et al.* 2017). Some are known to activate the PRRs (for example, ceramide, cholesterol crystals, ROS, urate crystals and Aβ), which should aid the maintenance of low-grade inflammation (Goldberg and Dixit 2015; Heneka *et al.* 2015). By comparison, the activation step can be mediated by distinct pathways from molecular garbage. For instance, while aged microglia express similar levels of inward rectifier K^+ channels to young microglia in mice, outward rectifier K^+ channels are found upregulated in the aged microglia, increasing the propensity to K^+ efflux from these cells (Schilling and Eder 2015). Accumulation of lipid droplets, cell debris and damaged proteins in lysosomes was found in the aged microglia with altered functions (such as impaired phagocytosis and producing elevated levels of proinflammatory cytokines and ROS) (Marschallinger *et*

al. 2020; Safaiyan *et al.* 2016). Since lysosomal damages caused by Aβ can activate the NLRP3 inflammasome in AD (Heneka *et al.* 2015), it is plausible that age-related dysfunctions of lysosomes might contribute to the inflammasome activation. In parallel, age-dependent mitochondrial damages are widely acknowledged owing to the downregulation of genes responsible for mitochondrial functions and robust increase in the oxidised mitochondrial DNA in aged human brains (Lu *et al.* 2004; Mecocci *et al.* 1993). In addition, emerging evidence highlighted the role of NLRP3 acetylation as a predisposing factor to the NLRP3 inflammasome activation (He *et al.* 2020). The authors found that expression of sirtuin 2 (SIRT2) (cytosolic deacetylase) was halved in bone-marrow derived macrophages from aged mice (He *et al.* 2020). This promotes NLRP3 acetylation and makes it more prone to form the NLRP3 assembly when the isolated cells were treated with LPS and nigericin (He *et al.* 2020).

The NLRP3 inflammasome pathway is activated in microglia and macrophages in the CNS following systemic inflammation. Proinflammatory cytokines produced in the periphery are known to pass through the BBB and consequently activate the cytokine receptors on microglia (Dantzer and Kelley 2007). Alternatively, circulating LPS and other TLR ligands should have access to the brain regions where the BBB is absent (for example, the circumventricular organs, leptomeninges and choroid plexus) and activate microglia and macrophages in these regions (Rivest 2009). Subsequently, TNF and other proinflammatory mediators are synthesised and simulate microglia across the parenchyma in an autocrine and paracrine manner (Rivest 2009). Endotoxin challenge into young mice impaired neuronal mitochondrial functions (as evidenced by the shorter length) (Harland *et al.* 2020) and promoted the lipid droplet formation inside microglia (Marschallinger *et al.* 2020). While systemic LPS challenge upregulated the P2X7 receptor in the rat brain (Choi *et al.* 2007), endotoxin injection into P2X7 receptor-deficient mice attenuated the proinflammatory cytokine production in the brain (Mingam *et al.* 2008). These data collectively indicated that systemic inflammation can prime the NLRP3 inflammasome but also produce various activation signals for the assembly. In line with the hypothesis that neuroinflammation contributes to the cerebral damages in patients with sepsis, a recent study showed that treating mice with an NLRP3 inflammasome inhibitor before the endotoxin challenge hindered the loss of dendritic spines in the hippocampus of aged mice at three months post-injection (Beyer *et al.* 2020).

On a separate note, there exists another pathway where LPS generates the NLRP3 inflammasome, called the non-canonical NLRP3 inflammasome pathway. A major difference from the canonical pathway is the requirement of intracellular LPS (Yang *et al.* 2015). Once LPS enters cells via infection or transfection, caspase-11 is activated by LPS to cleave the pannexin-1 channel (Yang *et al.* 2015). This allows for ATP release and the subsequent P2X7 receptor activation on the same or neighbouring cells, leading to the K^+ release and the NLRP3 assembly (Yang *et al.* 2015). However, it is important to emphasise that this non-canonical pathway is less relevant to SAE because the cerebral damages are mediated by neuroinflammatory responses to systemic inflammation, rather than the direct infection of CNS cells by pathogens (Eidelman *et al.* 1996; Widmann and Heneka 2014).

In the meantime, cellular senescence is defined as the proinflammatory fate of aged cells when their cell cycles are permanently arrested, but they produce a collection of proinflammatory cytokines, chemokines, growth factors and proteases (known as senescence-associated secretory phenotype (SASP)) (Baker and Petersen 2018). In the CNS, previous studies found that many cell types can adapt this senescent phenotype (including neurons, microglia and astrocytes), and their roles in neuropathology have been proposed (Baker and Petersen 2018). Notably, some of the cytokines that characterise SASP are released by the NLRP3 inflammasome pathway (for instance, IL-1β, IL-18, high-mobility group box 1 (HMGB1)) (He *et al.* 2016; Lamkanfi *et al.* 2010; Gorgoulis *et al.* 2019). As discussed earlier, deletion of *Nlrp3* prevented the onset of inflammaging in the hippocampus (Youm *et al.* 2013) and increased the proliferative capacity of splenic T lymphocytes in aged mice (indicative of the rescue of T cell senescence) (Youm *et al.* 2012). Therefore, it is likely that cellular senescence in the CNS may be induced or promoted by activation of the NLRP3 inflammasome pathway following sepsis in the aged brains, and senescent cells may contribute to the sustained inflammation thereafter.

1.7 Aims

The main aims of the present study are as follows:

1. To investigate whether sepsis-like systemic inflammation can produce acute or chronic cerebral damage in the hippocampus of aged (14-16 months old) mice with an interest in the induction of global or region-specific changes in excitatory and inhibitory synapses
2. To explore whether different bacterial strains of LPS may produce varying degrees of the neuroinflammatory responses and cerebral damage
3. To study whether the synapse loss may be associated with the increased synaptic pruning by microglia
4. To examine whether the complement and NLRP3 inflammasome pathway may be activated following systemic inflammation and whether their activations are associated with the cerebral damage
5. To investigate whether the systemic inflammation in aged mice can drive cellular senescence in the wake of the NLRP3 inflammasome activations
6. To study whether the absence of functional TREM2 proteins in microglia may modify the synapse pathology in aged (12 months old) APP/PS1 mice (animal model of AD) possibly via the impaired synaptic pruning

Chapter 2: Materials and Methods

2.1 Materials

2.1.1 Animals and husbandries

2.1.1.1 C57BL/6N mice for endotoxin injection

Female C57BL/6N mice (Charles River, RRID: IMSR_JAX:000,664) were housed together in the University of Bonn Medical Center animal facility. Up to five mice were maintained in the same cage with *ad libitum* access to water and food. All the animals were housed on 12-hour light/dark cycles at the temperature of 21 ± 1˚C and relative humidity of 55 ± 10%.

2.1.1.2 APP/PS1 mice and APP/PS1; *Trem2*^{T66M} mice

The following transgenic and knock-in lines were bred and maintained at an external breeding facility (Taconic Biosciences, Silkeborg, Denmark) until 11-12 months of age, transported to the University of Bonn Medical Center and housed in the same room as the C57BL/6N mice. Both male and female mice were used.

APP/PS1 mice are a transgenic mouse line harbouring human *APP* (amyloid precursor protein) Swedish mutations (K595N/M596L) and a *PSEN1* (presenilin 1) mutation (ΔE9) under the mouse prion protein promoter (Jankowsky *et al.* 2001). At the age of 12 months, Aβ depositions become abundant in the cortex (Venegas *et al.* 2017). Meanwhile, *Trem2*^{T66M} mutant mice are a knock-in mouse line containing a T66M mutation associated with frontotemporal dementia (FTD)-like syndromes (Kleinberger *et al.* 2017). Since this mutation is a loss-of-function point mutation (Guerreiro *et al.* 2013a), *Trem2*^{T66M} mutant mice are functionally equivalent to the *Trem2* knockout mice.

2.1.2 Drugs injected into mice

The following LPS were used at the respective dosages to model systemic inflammation in mice *in vivo* while Dulbecco's phosphate-buffered saline (DPBS) was injected into the control group (**Table 3**).

Table 3. Drugs injected into mice.

Drugs	Dosage	Manufacture	Cat. no.
LPS from *Salmonella enterica* serotype Typhimurium	2x, 4x, 7x 1.5 mg/kg	Sigma-Aldrich (Munich, Germany)	L6511
LPS from *E. coli* O55:B5	2x 1.5 mg/kg	Sigma-Aldrich (Munich, Germany)	L2880
DPBS	2x, 4x, 7x 1.5 mg/kg	Gibco (Darmstadt, Germany)	14190-094

Abbreviations: DPBS, Dulbecco's phosphate-buffered saline; LPS, lipopolysaccharide.

2.1.3 Antibodies

The following primary and secondary antibodies were used for immunohistochemistry (**Table 4**) and western blot (**Table 5**).

Table 4. Antibodies used for the histological analysis.

Antibody	Dilution	Manufacture	Cat. no. (RRID)
Mouse monoclonal anti-NeuN	1:500	Chemicon (Munich, Germany)	MAB377 (AB_2298772)
Mouse monoclonal anti-PV	1:500	Millipore (Munich, Germany)	MAB1572 (AB_2174013)
Guinea pig polyclonal anti-VGLUT2	1:500	Synaptic Systems (Göttingen, Germany)	135 404 (AB_887884)
Mouse monoclonal anti-PSD95	1:250	Millipore (Munich, Germany)	MAB1596 (AB_2092365)
Guinea pig polyclonal anti-VGAT	1:1000	Synaptic Systems (Göttingen, Germany)	131 004 (AB_887873)
Mouse monoclonal anti-gephyrin	1:100	Santa Cruz Biotechnology (Heidelberg, Germany)	sc25311 (AB_627670)
Rat monoclonal anti-C3	1:250	Abcam (Cambridge, UK)	ab11862 (AB_2066623)
Mouse monoclonal anti-MOG	1:250	Santa Cruz Biotechnology (Heidelberg, Germany)	sc166172 (AB_2145540)

Rabbit polyclonal anti-Iba1	1:1000	Wako Chemicals (Neuss, Germany)	019-19741 (AB_839504)
Rat monoclonal anti-CD68	1:200	Bio-Rad Laboratories (Feldkirchen, Germany)	MCA1957 (AB_322219)
Rat monoclonal anti-GFAP	1:1000	Invitrogen (Darmstadt, Germany)	13-0300 (AB_2532994)
Mouse monoclonal anti-lamin B1	1:500	Proteintech (Chicago, IL, USA)	66095-1-Ig (AB_11232208)
Rabbit polyclonal anti-amyloid fibrils OC	1:500	Millipore (Munich, Germany)	AB2286 (AB_1977024)
Rabbit polyclonal anti-oligomer A11	1:250	Thermo Fisher Scientific (Darmstadt, Germany)	AHB0052 (AB_2536236)
Goat anti-rabbit Alexa Fluor 488	1:500	Invitrogen (Darmstadt, Germany)	A-11008 (AB_143165)
Goat anti-rabbit Alexa Fluor 594	1:500	Invitrogen (Darmstadt, Germany)	A-11072 (AB_2534116)
Goat anti-rabbit Alexa Fluor 647	1:500	Invitrogen (Darmstadt, Germany)	A-21244 (AB_2535812)
Goat anti-rat Alexa Fluor 488	1:500	Invitrogen (Darmstadt, Germany)	A-11006 (AB_2534074)
Goat anti-rat Alexa Fluor 594	1:500	Invitrogen (Darmstadt, Germany)	A-11007 (AB_10561522)
Goat anti-rat Alexa Fluor 647	1:500	Invitrogen (Darmstadt, Germany)	A-21247 (AB_141778)
Goat anti-mouse Alexa Fluor 488	1:500	Invitrogen (Darmstadt, Germany)	A-11017 (AB_2534084)
Goat anti-mouse Alexa Fluor 594	1:500	Invitrogen (Darmstadt, Germany)	A-11032 (AB_2534091)
Goat anti-mouse Alexa Fluor 647	1:500	Invitrogen (Darmstadt, Germany)	A-21236 (AB_2535805)
Goat anti-guinea pig Alexa Fluor 488	1:500	Invitrogen (Darmstadt, Germany)	A-11073 (AB_2534117)
Goat anti-guinea pig Alexa Fluor 647	1:500	Invitrogen (Darmstadt, Germany)	A-21450 (AB_2735091)

Abbreviations: GFAP, glial fibrillary acidic protein; MOG, myelin oligodendrocyte glycoprotein; PSD95, postsynaptic protein density 95; PV, parvalbumin; VGAT, vesicular GABA transporter; VGLUT2, vesicular glutamate transporter 2.

Table 5. Antibodies used for western blot analysis.

Antibody	Dilution	Manufacture	Cat. no. (RRID)
Mouse monoclonal anti-IL-1β	1:2000	R&D Systems (Wiesbaden-Nordenstadt, Germany)	AB401-NA (AB_354347)
Rabbit polyclonal anti-PSD95	1:1000	Abcam (Cambridge, UK)	ab18258 (AB_444362)
Mouse monoclonal anti-synaptophysin	1:10,000	Millipore (Munich, Germany)	MAB5258 (AB_2313839)
Rabbit polyclonal anti-VGAT	1:1000	Millipore (Munich, Germany)	AB5062P (AB_2301998)
Mouse monoclonal anti-gephyrin	1:1000	Santa Cruz Biotechnology (Heidelberg, Germany)	sc25311 (AB_627670)
Mouse monoclonal anti-β actin	1:1000	Cell Signaling Technology (Frankfurt am Main, Germany)	4967L (AB_330288)
Rabbit polyclonal anti-α tubulin	1:1000	Millipore (Munich, Germany)	CP06 (AB_2617116)
Mouse monoclonal anti-caspase-1 (p20)	1:1000	AdipoGen (Adipogen, Liestal, Switzerland)	AG-20B-0042 (AB_2490248)
Rabbit polyclonal anti-ASC	1:1000	AdipoGen (Adipogen, Liestal, Switzerland)	AG-25B-0006 (AB_2490440)
IRDye 800CW donkey anti-mouse	1:20,000	LI-COR Biosciences (Lincoln, NE, USA)	926-32212 (AB_621847)
IRDye 680RD donkey anti-mouse	1:20,000	LI-COR Biosciences (Lincoln, NE, USA)	926-68072 (AB_10953628)
IRDye 800CW donkey anti-rabbit	1:20,000	LI-COR Biosciences (Lincoln, NE, USA)	926-32213 (AB_621848)
IRDye 800CW goat anti-rat	1:20,000	LI-COR Biosciences (Lincoln, NE, USA)	926-32219 (AB_1850025)

Abbreviations: ASC, apoptosis-associated speck-like protein containing a C-terminal caspase recruitment domain; IL, interleukin; PSD95, postsynaptic protein density 95; VGAT, vesicular GABA transporter.

2.1.4 Buffers

Name of buffers and their constitutes used in the present study were summarised below in table 6.

Table 6. List of buffers.

Buffers	Concentration	Reagent	Manufacture	Cat. no.
Immunohistochemistry				
Citrate buffer (pH 6.0)	100 mM	Trisodium citrate	Carl Roth (Karlsruhe, Germany)	3580.3
PBST (pH 7.4)	0.1% (v/v)	Triton X-100	Carl Roth (Karlsruhe, Germany)	3051.3
	0.01 M	PBS	Millipore (Munich, Germany)	L182-10
0.1 M phosphate buffer (pH 7.2)	0.019 M	Monobasic NaP	Carl Roth (Karlsruhe, Germany)	T879.1
	0.081 M	Dibasic NaP	Carl Roth (Karlsruhe, Germany)	X987.2
Western blot				
TBST (pH 7.5)	15 mM	NaCl	PanReac AppliChem (Darmstadt, Germany)	131659
	5 mM	Tris	Carl Roth (Karlsruhe, Germany)	5429.3
	0.01% (v/v)	Tween 20	Carl Roth (Karlsruhe, Germany)	9127.1
RIPA (pH 7.2)	75 mM	NaCl	PanReac AppliChem (Darmstadt, Germany)	131659
	3.5 mM	SDS	MP Biomedicals (Eschwege, Germany)	811030
	16 mM	NP-40	USBiological (Swampscott, MA, USA)	N3500
	12 mM	Na-DOC	Sigma-Aldrich (Munich, Germany)	D6570
	25 mM	Tris	Carl Roth (Karlsruhe, Germany)	5429.3
Synaptosome isolation				
0.32 M sucrose buffer (pH 7.4)	0.32 M	Sucrose	Carl Roth (Karlsruhe, Germany)	4621.11
	2 mM	EDTA	Carl Roth	8043.1

			(Karlsruhe, Germany)	
	2 mM	EGTA	Carl Roth (Karlsruhe, Germany)	6054.2
	2 mM	Na_3VO_4	PanReac AppliChem (Darmstadt, Germany)	A2196
	5 mM	NaF	Carl Roth (Karlsruhe, Germany)	P756.1
	5 mM	$Na_2H_2P_2O_7$	Sigma-Aldrich (Munich, Germany)	P8135
	10 mM	HEPES	Carl Roth (Karlsruhe, Germany)	9105.2

Abbreviations: PBS, phosphate buffered saline; PBST, phosphate buffered saline with Triton X-100; RIPA, radioimmunoprecipitation assay; TBST, Tris-buffered saline with Tween 20.

2.1.5 Other materials

The following table 7 described all the other materials used in this study.

Table 7. List of materials.

Materials	Manufacture	Cat. no.
Endotoxin injection and tissue collection		
Insulin syringe	BD Medical (Le Pont-de-Claix, France)	324826
Injekt-F (1 ml)	B. Braun (Hessen, Germany)	9166017V
BD Microlance 25 G syringe	BD Biosciences (Drogheda, Ireland)	300600
Ketamine	Ratiopharm (Ulm, Germany)	4089014
Xylazine	Serumwerk Bernburg (Bernburg, Germany)	779-636
Immunohistochemistry		
PFA	Sigma-Aldrich (Munich, Germany)	P6148
Agarose	Carl Roth (Karlsruhe, Germany)	2267.4
Normal goat serum	Abcam (Cambridge, UK)	ab7481
SuperFrost microscope slides	Thermo Scientific	12372098

	(Rockford, IL, USA)	
Immu-Mount mounting medium	Thermo Fisher Scientific (Darmstadt, Germany)	9990402
High precision microscope cover glasses	Paul Marienfeld (Lauda-Königshofen, Germany)	0117580
Coverglass (24 x 60 mm)	Duran Group (Mainz, Germany)	235503704
CoverGrip coverslip sealant	Biotium (Fremont, CA, USA)	23005
In situ Cell Death Detection Kit, TMR red	Roche Applied Science (Mannheim, Germany)	12156792910
Methoxy X04	Tocris Bioscience (Bristol, UK)	4920
Biochemistry		
EDTA-free Pierce protease inhibitor tablet	Thermo Fisher Scientific (Darmstadt, Germany)	A32965
Polypropylene tube with snap-on cap (11 x 39 mm) (1.5 ml)	Beckman Coulter (Krefeld, Germany)	357448
Protease/phosphatase inhibitor cocktail	Cell Signaling Technology (Frankfurt am Main, Germany)	5872S
Pierce BCA protein assay kit	Thermo Scientific (Rockford, IL, USA)	23225
NuPAGE LDS sample buffer	Invitrogen (Darmstadt, Germany)	NP0007
10x Bolt sample reducing agent	Invitrogen (Darmstadt, Germany)	B0009
NuPAGE 4-12% Bis-Tris protein 10-well gels	Invitrogen (Darmstadt, Germany)	NP0321BOX
NuPAGE 4-12% Bis-Tris protein 10-well gels	Invitrogen (Darmstadt, Germany)	WG1402BOX
NuPAGE MOPS running buffer	Invitrogen (Darmstadt, Germany)	NP0001
NuPAGE MES running buffer	Invitrogen (Darmstadt, Germany)	NP0002
PageRuler prestained protein ladder	Thermo Scientific (Rockford, IL, USA)	26617
Trans-Blot Turbo transfer system	Bio-Rad Laboratories (Feldkirchen, Germany)	1704150

Trans-Blot Turbo mini 0.2 µm nitrocellulose transfer packs	Bio-Rad Laboratories (Feldkirchen, Germany)	170-4158
Trans-Blot Turbo midi 0.2 µm nitrocellulose transfer packs	Bio-Rad Laboratories (Feldkirchen, Germany)	170-4159
Bovine serum albumin – fraction V	Rockland Immunochemicals (Limerick, PA, USA)	BSA-50
V-PLEX proinflammatory panel 1 (mouse) kit	Meso Scale Discovery (Rockville, MD, USA)	K15048D

Abbreviations: BCA, bicinchoninic acid; BSA, bovine serum albumin; PFA, paraformaldehyde.

2.1.6 Software

All the software used in the present study was summarised below in table 8.

Table 8. List of software.

Software	Manufacture / original article / URL
Fiji	(Schindelin *et al.* 2012) https://imagej.net/Fiji
Fiji FigureJ 1.35 plugin	(Mutterer and Zinck 2013) https://imagejdocu.tudor.lu/plugin/utilities/figurej/start
Fiji ComDet 0.3.6.1 plugin	https://github.com/ekatrukha/ComDet/wiki
Fiji Skeletonize (2D/3D) plugin	(Doube *et al.* 2010) https://imagej.net/Skeletonize3D
Fiji Analyze Skeleton (2D/3D) plugin	(Arganda-Carreras *et al.* 2010) https://imagej.net/AnalyzeSkeleton
Imaris version 9.1.2	Bitplane (Zurich, Switzerland)
Imaris Viewer version 9.5.1	Bitplane (Zurich, Switzerland)
Image Studio software version 5.2.5	LI-COR Biosciences (Lincoln, NE, USA)
GraphPad Prism software version 9	GraphPad Software (La Jolla, CA, USA)
G*Power software version 3.1.9.6	(Faul *et al.* 2007)

2.2 Endotoxin injection and sample collection

2.2.1 LPS injection into C57BL/6N mice

Endotoxin injection, monitoring of animals following the treatment and sample collection were partly performed by Dr Ildikó Rácz and Ms Stephanie Schwarz. Power analysis (power = 0.80, estimated effect size = 0.40) estimated the sample sizes of each treatment group using the G*Power software version 3.1.9.6 (Faul *et al.* 2007), and this was performed by Dr Ildikó Rácz.

Endotoxin was intraperitoneally injected into female 14- to 16-month-old C57BL/6N mice (25-40 g) at 1.5 mg/kg on two consecutive days (2xLPS) (**Fig. 4A**). The following LPS derived from two bacterial strains was compared: *Escherichia coli* (*E. coli*) O55:B5 (cat. no. L2880; Sigma-Aldrich, St. Lois, USA) or *Salmonella enterica* serotype Typhimurium (cat. no. L6511; Sigma-Aldrich). Of note, since these LPS shared the same endotoxin levels (3,000,000 endotoxin units/mg), extraction method (phenol extraction) and solubility, effects of different preparation methods on the immune reactions *in vivo* should be relatively small. Control groups were given DPBS as a vehicle. The treated mice were monitored by recording the body weights and clinical symptom scores three times per day and observing the behaviours from outside the cage twice per day from the dates of injections to 6 days post-final injection (dpi) (every 2 h from 8:00 to 20:00). In the following week, the monitoring frequency was reduced to twice and once a day from 7 to 10 dpi and from 11 to 13 dpi, respectively. Then, the animals were monitored on a weekly basis until the samples were collected at 63 dpi. During this animal health monitoring, in case that the highest clinical symptom score was rated, or the weight loss exceeded 25% of their baseline body weight for 48 hours, the animals were killed by CO_2.

At 7 or 63 dpi, a lethal dose of anaesthesia solution (100 mg/kg ketamine and 16 mg/kg xylazine) was intraperitoneally injected into mice, and transcardial perfusion was performed using ice-cold phosphate-buffered saline (PBS). A half brain hemisphere was immediately frozen in liquid nitrogen. The other hemisphere without the cerebellum was soaked in 4% (w/v) paraformaldehyde (PFA) in PBS at 4˚C. Following overnight fixation, PFA was washed out in PBS twice, and the brains were stored in 0.01% (w/v) NaN_3 in PBS at 4˚C until use.

Additional cohorts of aged mice (14-16 months old) received prolonged periods of endotoxin injections in order to investigate the effects of the sustained inflammation on the CNS in aged animals. To this end, 1.5 mg/kg *Salmonella* LPS was intraperitoneally administered into 14- to 16-month-old mice on four (4xLPS) and seven consecutive days (7xLPS), and the samples were collected at 7 dpi (**Fig. 4B, C**). The same animal monitoring protocol, euthanasia criteria and killing method were used as the 2xLPS group. All these animal experiments using 14- to 16-month-old

C57BL/6N mice were approved by the local ethical committee (LANUV NRW 81-02.04.2020.A324) and adhered to the Declaration of Helsinki.

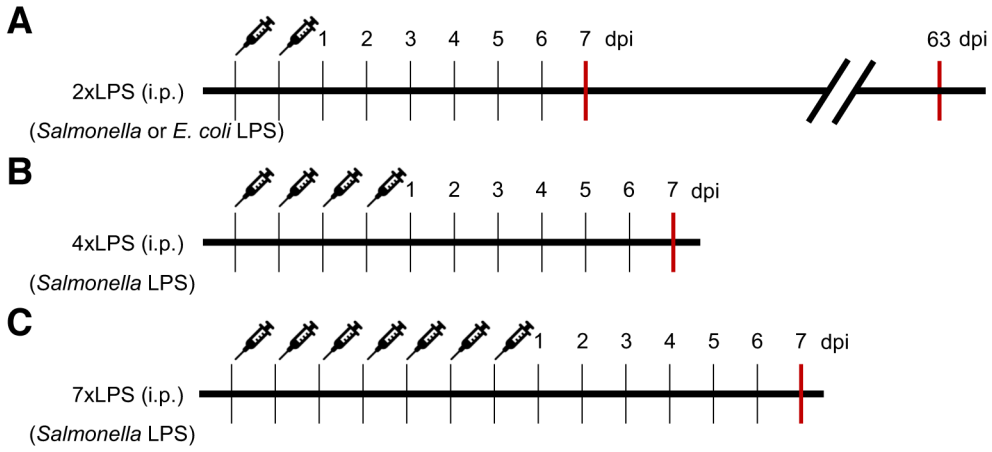

Figure 4. LPS injection paradigms in aged C57BL/6N mice.

(A) 2xLPS group. Either *Salmonella* or *E. coli* LPS was intraperitoneally (i.p.) injected in aged mice (14-16 months old) on two consecutive days. Samples were collected at 7 and 63 dpi (red lines).

(B, C) 4xLPS and 7xLPS groups. Only *Salmonella* LPS was injected (i.p.) into aged mice (14-16 months old) on either four or seven consecutive days. Samples were collected at 7 dpi (red line).

In all the injection paradigms, DPBS was injected as a vehicle at the same time, and each dosage was 1.5 mg/kg.

Abbreviations: DPBS, Dulbecco's phosphate-buffered saline; dpi, days post-final injection; LPS, lipopolysaccharide.

2.2.2 Sample collection of APP/PS1 and APP/PS1; Trem2^{T66M} mice

Sample collection and genotyping of animals were performed by Ms Stephanie Schwarz. Of note, LPS injection into these animals was not performed.

At 12 months of age, animals were killed by an intraperitoneal injection of 10 µl/g body weight of an anaesthesia solution (100 mg/kg ketamine and 20 mg/kg xylazine). A hemibrain was fixed in 4% (w/v) PFA in PBS at 4˚C overnight, washed in PBS for 5 min twice and placed in 30% (w/w) sucrose solution in PBS at 4˚C for 2-3 days. If the brains were not found to be floating in the solution, the brains were frozen by 2-methylbutane immersion and stored at -80˚C until use. The other brain hemisphere

was collected for other experiments performed by Dr Nàdia Villacampa-Pérez, and these data were not described in this thesis. These procedures of animal experimentation were approved by the local ethical committee (LANUV NRW 81-02.04.2017.A451).

2.3 Immunohistochemistry on free floating sections

2.3.1 Vibratome sectioning of the C57BL/6N mouse brains

Coronal 40-µm-thick brain sections were produced by a vibratome (Leica VT1000S, Leica Biosystems, Wetzlar, Germany). These sections were sequentially collected in 0.01% (w/v) NaN_3 in PBS in a way that each microcentrifuge tube contains three or four brain sections equally separated by 400 µm. These sections were stored at 4˚C until use.

2.3.2 Cryostat sectioning of the APP/PS1 transgenic mouse brains

This cryostat sectioning was performed by Dr Nàdia Villacampa-Pérez. Coronal 30-µm-thick brain sections were generated using a cryostat (Leica CM3050S, Leica Biosystems) and stored in cryoprotectant solution (0.58 M sucrose, 0.25 mM PVP-40, 30% (v/v) ethylene glycol in 0.2 M phosphate buffer) at -20˚C. Prior to the histological experiments, the cryoprotectant solution was washed out in PBS for 30 min.

2.3.3 Immunohistochemistry

Three equidistant brain sections per animal were exposed to a permeabilisation buffer (0.1% (v/v) Triton X-100 in PBS (PBST)) for 5 min three times, a blocking buffer (10% (v/v) normal goat serum (Abcam, cat. no. ab7481; RRID: AB_2716553) in PBST) for an hour and an antibody solution diluted in the blocking buffer at 4˚C overnight. On the next day, the sections were washed in PBST for 5 min three times, incubated with the appropriate secondary antibodies (Invitrogen, Darmstadt, Germany) in the blocking buffer for 1.5 hours in dark. Of note, these secondary antibodies were centrifuged at 13,000*g* for 1 min at 4˚C to allow the crystals to sink to the tube bottom in advance (Eppendorf 5424R, Eppendorf AG, Hamburg, Germany). Then, the sections were washed in PBS for 5 min three times in dark and mounted on the SuperFrost microscope slides (Thermo Scientific, Rockford, IL, USA) using Immu-Mount mounting medium (Thermo Fisher Scientific, Darmstadt, Germany). Thickness

of the coverslip was determined by the type of microscopes. A high precision coverglass (#1.5H thickness) (Paul Marienfeld, Lauda-Königshofen, Germany) was used for the super-resolution imaging, while a standard coverslip (#1.5 thickness) (Duran Group, Mainz, Germany) for the confocal imaging.

Depending on the antigens of interest, antigen retrieval was either performed or avoided. Some antigens, such as PSD95 and gephyrin, required heat mediated antigen retrieval by boiling the sections in 10 mM citrate buffer (pH 6) at 95˚C for 15 min and cooling down to room temperature for 20-30 min. In contrast, antigen retrieval can completely eliminate signals of some protein targets (e.g. CD68) (Nakagawa *et al.* 2017). In order to preserve immunoreactivity of these proteins, some experiments were performed sequentially. Namely, once the staining was completed without the antigen retrieval, the antigen retrieval was performed, followed by repeating the same staining protocol.

2.4 Confocal imaging and image analysis

2.4.1 Stereological analysis of neuron and microglia density

Stereology was performed to estimate density of neurons and microglia in a unbiased way (West and Gundersen 1990). Brain tissue sections were stained for NeuN-positive neurons, parvalbumin (PV)-positive interneurons, Iba1-positive microglia and DAPI-positive nuclei. For NeuN and Iba1 staining, confocal images were taken using a Leica TCS SP8 confocal microscope (Leica Microsystem) with a 40x/NA1.1 water objective. In contrast, PV-stained sections were acquired using the same microscope with a 25x/NA0.95 water objective. Eleven serial optical images were obtained at 1 µm intervals. To analyse the density of NeuN-positive neurons, fifteen 50 µm × 50 µm optical fractionators were manually placed on the images in the Fiji software, and NeuN/DAPI-positive nuclei inside the fractionators were counted every three z plane (Schindelin *et al.* 2012). Meanwhile, because microglia and interneurons are less abundant than neurons in the pyramidal cell layers, a larger size of fractionator (300 µm × 300 µm or 500 µm × 240 µm) was placed on the maximum intensity projection images, and Iba1/DAPI- and PV/DAPI-positive nuclei were counted in the Fiji software. During the image analysis, the experimenter was blinded to the treatment groups. The

representative figures were created using a Fiji FigureJ 1.35 plugin (https://imagejdocu.tudor.lu/plugin/utilities/figurej/start) (Mutterer and Zinck 2013).

2.4.2 Histological analysis of microglial senescence

Vibratome sections were stained for nuclear envelop proteins (lamin B1), microglia (Iba1) and nuclei (DAPI). Confocal micrographs were acquired using the Leica TCS SP8 confocal microscope with the 40x objective (step size of 1 µm and 10 optical planes) (Leica Microsystem). At least 25 non-overlapping microglial nuclei were selected and outlined on the maximum intensity projection images in the Fiji software. Subsequently, the integrated density of individual lamin B1 signals was measured. The corrected total cell fluorescence (CTCF) of lamin B1 was then calculated by subtracting the product of mean background signals and the area of microglial nuclei from the integrated density. The circularity of microglial nuclei was measured to study the nuclear architecture using a Fiji circularity built-in function by the following equation: circularity = $4\pi \times (\text{area}/\text{perimeter})^2$. The circularity index equal to one means the perfect roundness of a circle (Barascu *et al.* 2012).

2.4.3 TUNEL staining

Terminal deoxynucleotidyl transferase dUTP nick end labelling (TUNEL) staining followed Deng *et al.*'s (2001) recommendations. In brief, three brain sections per animal were incubated in 0.5% (v/v) PBST at 80˚C for 20 min. These sections were immediately mounted on the SuperFrost microscope slides (Thermo Scientific). After the sections became dry, samples were incubated in 50 µl of reaction mixtures (*in situ* Cell Death Detection Kit, TMR red, cat. no. 12156792910, Roche Applied Science, Mannheim, Germany) at 37˚C for 1 h. This was followed by washing in PBS for 5 min twice and water for 5 min once. Sections were cover-slipped with a standard coverglass (#1.5 thickness) (Duran Group) using 1 mg/ml DAPI-supplemented Immu-Mount (Thermo Fisher Scientific). Ten serial 25x confocal z-stacks were acquired at 1-µm intervals using the Leica TCS SP8 confocal microscope (Leica Microsystem).

2.4.4 Analysis of Aβ fibrillar oligomers and plaques

Cryostat sections were stained for fibrillar Aβ oligomers (OC) and plaques (methoxy X04). Four serial confocal z-stacks were taken at 4 µm intervals using a Zeiss LSM880

microscope (Carl Zeiss, Oberkochen, Germany) with a 20x/NA0.8 air objective. The entire hippocampus and parietal cortex were acquired. Number and area that were positive for the oligomer and plaque staining were measured on the maximum intensity projection images using a Fiji “Analyze Particles” function.

2.5 Super-resolution imaging and image analysis

2.5.1 Super-resolution imaging and deconvolution

Super-resolution microscope was used to perform the analysis involving the synaptic puncta and myelin proteins (myelin oligodendrocyte glycoprotein (MOG)). Following the staining experiments, optical images were serially taken at 0.5 µm intervals over a depth of 8-10 µm using a Zeiss LSM980 microscope with Airyscan 2 (Carl Zeiss). During the image acquisition, a digital zoom of 1.8 and a 63x/NA1.4 oil immersion objective were used.

Synaptic pruning by microglia was also assessed in the super-resolution images. The z-stacks were acquired at 0.5 µm intervals at the digital zoom of 1.8 using the Zeiss LSM980 microscope with Airyscan 2 (Carl Zeiss). A 40x/NA1.4 oil objective was alternatively used in order to ensure that the whole structure of the microglial cell was visible. For this purpose, all the cells, part of which was not observed, were excluded from the analysis. This limited the number of cells to eight or nine per region of interest.

The Wiener filter-based deconvolution was applied on all the super-resolution images using a built-in 3D Airyscan processing algorithm on Zen Blue version 3.1 software (Carl Zeiss).

2.5.2 Analysis of synaptic puncta and C3 puncta in the hippocampus of C57BL6/N mice

Synaptic puncta were quantified according to Sauerbeck *et al.*’s (2020) methods with several modifications. Three vibratome sections of C57BL6/N mice (400 µm apart) were stained for excitatory synaptic proteins (vesicular glutamate transporter 2 (VGLUT2) and postsynaptic protein density 95 (PSD95)), inhibitory synaptic proteins (vesicular GABA transporter (VGAT) and gephyrin) and complement factor (C3). Following the super-resolution imaging, automatic detection of excitatory synaptic

puncta was performed on a Fiji ComDet 0.3.6.1 plugin (https://github.com/ekatrukha/ComDet/wiki). Colocalisation of excitatory synaptic puncta (i.e. excitatory synapses) and colocalisation of C3 puncta with excitatory synaptic puncta (i.e. synaptic C3) were determined if the distance of two punctum centres was shorter than 200 nm. Of note, this distance was previously measured using the similar super-resolution microscope with the Airyscan detector and verified as synapses using an electron microscope (Sauerbeck *et al.* 2020).

However, applying the same methods to quantify the inhibitory synapses were hindered because larger, non-punctum fluorescent signals of VGAT were observed. This fluorescent pattern might reflect that VGAT is densely accumulated at the nerve endings of inhibitory neurons (Chaudhry *et al.* 1998). Instead of quantifying the number of puncta, VGAT-positive area was measured using the Fiji “Analyze Particles” function on binary images. In contrast, gephyrin signals showed clear puncta staining pattern, thus they were quantified on the Fiji ComDet 0.3.6.1 plugin. Following the analysis, the representative figures were created using Imaris version 9.1.2 (Bitplane, Zurich, Switzerland).

2.5.3 Analysis of synaptic puncta in the cortex of APP/PS1 transgenic mice

Three cryostat sections of APP/PS1 transgenic mouse brains were stained for excitatory synaptic proteins (VGLUT2 and PSD95) and Aβ plaques (methoxy X04). Once the super-resolution images were acquired, six circles were manually drawn at 2.5, 5, 10, 20, 40 and 80 µm from the centre of 8-9 plaques in the Fiji. Then, synaptic puncta density in each area was calculated using the Fiji ComDet 0.3.6.1 plugin. The maximum distance of the punctum centres was 200 nm to determine the colocalisation of pre- and postsynaptic puncta.

2.5.4 Analysis of myelin protein coverage in the hippocampus

Three vibratome sections of C57BL6/N mice were stained for myelin proteins (MOG). After the image acquisition, the super-resolution images were thresholded on the Fiji. The MOG-positive area was quantified using the Fiji “Analyze Particles” function.

2.5.5 Analysis of synaptic pruning by microglia in the hippocampus

Quantification of microglial synaptic pruning was based on Schafer *et al*.'s (2014) methods. Three vibratome sections were stained for synaptic puncta (PSD95), microglia (Iba1) and lysosomes (CD68). The super-resolution images were further processed in the Fiji by applying the mean filter (radius of 1.5 pixels) to smoothen the PSD95 and CD68 signals and subtracting the background based on a rolling ball algorithm. Noise in the Iba1 signals was also reduced by applying the median filter (radius of 10 pixels). Isolation of one microglial cell from each z-stack was performed using a Fiji "Find Connected Regions" built-in plugin. This followed the surface rendering of each microglial cell and lysosomes on Imaris version 9.1.2 (Bitplane). The volumes of microglia and microglial lysosomes were calculated. Further, the Imaris spot function detected the PSD95 puncta inside the lysosomes, and the number of synaptic puncta per lysosome volume was calculated to infer the levels of synaptic pruning by microglia.

2.5.6 Skeleton analysis of microglial morphology in the hippocampus

Following the isolation of microglia from the super-resolution z-stacks, morphology of each cell was assessed using skeleton analysis (Young and Morrison 2018). Each microglial cell was skeletonised using "Skeletonize (2D/3D)" and "Analyze Skeleton (2D/3D)" plugins in the Fiji software (Arganda-Carreras *et al.* 2010; Doube *et al.* 2010). The branch lengths shorter than 0.4 µm were considered to be artefacts and thus excluded from the analysis.

2.6 Biochemistry

2.6.1 Synaptosome preparation

Synaptosomes were isolated from the frozen brains using the protocols with several modifications (Wijasa *et al.* 2020). All the steps of this purification were performed at 4˚C. The brains were homogenised in a 0.32 M sucrose buffer (0.32 M sucrose, 2 mM EDTA, 2 mM EGTA, 2 mM Na_3VO_4, 5 mM NaF, 5 mM $Na_2H_2P_2O_7$, 10 mM HEPES and EDTA-free Pierce protease inhibitor tablet (cat. no. A32965, Thermo Fisher Scientific) (pH 7.4)) by applying 15-20 strokes in an ice-cold Teflon-glass homogeniser. Some of the homogenates (150 µl) were reserved to obtain the brain lysates for western blot and enzyme-linked immunosorbent assay (ELISA) and frozen at -80˚C. Samples were

centrifuged at 800*g* for 10 min to collect the post-nuclear supernatant (Eppendorf 5424R, Eppendorf AG), and this was repeated twice to ensure to reduce the contamination of cell debris. This supernatant was centrifuged at 10,000*g* for 15 min in a TLA-55 fixed rotor (Optima MAX-XP ultracentrifuge, Beckman Coulter, Krefeld, Germany). The pellet (i.e. crude synaptosome) was resuspended in 500 µl 0.32 M sucrose buffer (pH 7.4). Samples were slowly applied onto discontinuous sucrose gradients of 1.18 M, 1.0 M and 0.85 M sucrose buffers in buffer A (pH 7.4). After being accurately balanced, they were centrifuged at 82,000*g* for 60 min in an MLS-50 swinging-bucket rotor (Optima MAX-XP ultracentrifuge, Beckman Coulter). Synaptosome fraction at 1.18 M/1.0 M gradient boundary was collected and resuspended in three-fold volume of 0.32 M sucrose buffer. Subsequently, the synaptosomes were centrifuged at 10,000*g* for 15 min in a TLA-55 fixed rotor (Optima MAX-XP ultracentrifuge, Beckman Coulter). The pellet was resuspended in 100 µl 0.32 M sucrose buffer, aliquoted and frozen at -80˚C. The purity of synaptosome was verified by enrichment of synaptic proteins compared with total brain lysates by western blot.

2.6.2 Protein extraction from the frozen brain homogenates

The tissue lysates were purified from the brain homogenates reserved during the synaptosome purification. All the subsequent procedures were performed at 4˚C. The homogenates were slowly thawed and mixed with an equal volume of 2x radioimmunoprecipitation assay (RIPA) buffer (3.5 mM SDS, 12 mM Na-DOC, 16 mM NP-40, 25 mM Tris base, 75 mM NaCl, protease/phosphatase inhibitor cocktail (cat. no. 5872S, Cell Signaling Technology, Frankfurt am Main, Germany), pH 7.2). Samples were sonicated for 10 sec, incubated for 30 min in dark and centrifuged at 100,000*g* for 30 min in a TLA-55 fixed rotor (Optima MAX-XP ultracentrifuge, Beckman Coulter). The supernatants (i.e. lysates) were collected and frozen at -80˚C until use.

2.6.3 Bicinchoninic acid (BCA) assay to determine the total protein levels

Total protein levels in the synaptosome fractions and tissue lysates were determined by a BCA assay (Pierce BCA protein assay kit, cat. no. 23225, Thermo Scientific). In accordance with the manufacture guideline, the BCA protein reagents A and B were mixed at 50:1 ratio, and this mixture was applied on 2.5 µl of samples and 25 µl of

protein standards (water and bovine serum albumin (BSA) solutions at six different concentrations from 0.0625 to 2 mg/ml). Following the incubation at 37˚C for 30 min, the absorbance was measured at 562 nm using an Infinite M200 plate reader (Tecan, Crailsheim, Germany). Protein levels were estimated using the protein standard curve.

2.6.4 Immunoblot and its densitometric analysis

Equal amounts of proteins (20-40 µg) in synaptosome fractions or tissue lysates were added to a NuPAGE LDS sample buffer (cat. no. NP0007, Invitrogen) supplemented with 50 mM dithiothreitol (cat. no. B0009, Invitrogen). Then, samples were heated at 70˚C for 10 min and loaded into NuPAGE 4-12% Bis-Tris protein gels (Invitrogen). Protein separation was performed in either a NuPAGE MES or MOPS SDS running buffer (cat. no. NP0001, NP0002, Invitrogen), and the buffer type was determined by molecular weight of protein of interest. This was followed by transference to a 0.2 µm nitrocellulose membrane using a Trans-Blot Turbo transfer system (cat. no. 1704150, Bio-Rad Laboratories, Feldkirchen, Germany). Membranes were blocked in blocking solution (3% (w/v) BSA in Tris-buffered saline with Tween-20 (TBST) (15 mM NaCl, 5 mM Tris, 0.01% (v/v) Tween-20)) for an hour and exposed to the primary antibodies in the blocking solution at 4˚C overnight. On the next day, the membranes were washed in TBST for 5 min three times, incubated in the secondary antibodies (LI-COR Biosciences, Lincoln, NE, USA) diluted in 1% (w/v) BSA/TBST for an hour and washed in TBST for 5 min three times. The protein bands were imaged using an Odyssey infrared imaging system (LI-COR Biosciences). Signal intensity of each band was calculated in Image Studio software version 5.2.5 (LI-COR Biosciences).

2.6.5 ELISA to quantify proinflammatory cytokine levels in the brain

This experiment was performed by Mr Francesco Santarelli. The following proinflammatory cytokines were measured in the brain lysates using V-PLEX proinflammatory panel 1 (mouse) kit (cat. no. K15048D, Meso Scale Discovery, Rockville, MD, USA): CXCL1, TNF-α, IFN-γ, IL-1β, IL-2, IL-4, IL-5, IL-6, IL-10 and IL-12p70. Briefly, the samples were mixed with an equal volume of diluent 41 using a 96-well plate in this kit and incubated for 2 h with shaking. The samples were washed three times, incubated for the detection antibody for 2 h and washed three times. Following the subsequent reaction with a read buffer, all the cytokine levels were

measured using a SECTOR Imager 2400 reader (Meso Scale Discovery). All the raw data which were lower than the lowest level of quantification described in the manufacture guideline were excluded. Finally, cytokine levels were normalised by the total protein levels.

2.7 Statistical analysis

Each dot in all figures depicted a biological replicate. An error bar in most of the bar charts expressed mean ± standard error of measurement (SEM), while some median ± interquartile range (IQR) or 95% confidence intervals (CIs). All the violin plots and whisker plots showed the median and IQR.

Overall, the normality of the data distribution was assessed using a Shapiro-Wilk test for all the statistical analyses. As detailed below, if the data followed the Gaussian distribution, parametric tests were used. Otherwise, a Grubbs' test (alpha of 0.05) was employed to identify and remove one outlier of the samples in order to reach the normality. In special cases, data that did not pass the Shapiro-Wilk test even after eliminating the outlier were analysed by non-parametric tests (discussed below).

In chapter 3, survival after the LPS injections was assessed by the Kaplan-Meier method (a log-rank test). Weight loss was analysed using a two-way repeated measures analysis of variance (ANOVA) with a Tukey *post-hoc* test. Effects of three drug treatments (namely, vehicle, *Salmonella* LPS and *E. coli* LPS) on most of the parameters, including cytokine levels, microglial morphology and puncta quantification, at two points in time (at 7 dpi and 63 dpi) were analysed by either a two-way ANOVA with a Tukey *post-hoc* test or a non-parametric Kruskal-Wallis test with a Dunn's *post-hoc* test. If the analysis of three treatment groups focused on 7 dpi only, one-way ANOVA with a Tukey *post-hoc* test was performed. Data derived from the parametric tests were expressed as mean ± SEM in the main text, while data derived from the non-parametric tests were summarised in tables as median [IQR] (See **Tables 9, 10**).

In chapter 4, the effects of four injection paradigms of drugs (4xLPS, 4xVeh, 7xLPS and 7xVeh (See **Fig. 4**)) on neuron density were studied using a non-parametric

Kruskal-Wallis test with a Dunn's *post-hoc* test. Additionally, effects of two drug treatments (namely, vehicle and *Salmonella* LPS) on parameters indicating the microglial senescence at 7 dpi and 63 dpi were analysed by a two-way ANOVA with a Sidak *post-hoc* test. Alternatively, effects of ageing (namely, 14 and 16 months old) on the mean circularity of microglial nuclei in the vehicle-treated mice were tested using a two-tailed Student's t-test.

In chapter 5, the effects of two genotypes (that is, APP/PS1 and APP/PS1; *Trem2*^{T66M}) on the amyloid pathology in two regions of interest (that is, the parietal cortex and hippocampus) were assessed using a two-way ANOVA with a Sidak *post-hoc* test. Effects of two genotypes and the distance from plaque centre on synaptic puncta density were assessed using a Kruskal-Wallis test with a Dunn's *post-hoc* test. The effects of two genotypes on synaptic puncta density in the parietal cortex alone were tested using a two-tailed Mann-Whitney test.

The statistical software used was GraphPad Prism software version 9 (GraphPad Software, La Jolla, CA). Differences between groups were considered to be significant if $p < 0.05$.

Chapter 3: Cerebral Effects of Systemic Inflammation in Old Mice

3.1 An introduction to a rationale behind the LPS injection paradigm

This chapter aims to evaluate for acute and chronic effects of endotoxin injections in middle-aged (14-16 months old) mice at 7 dpi and 63 dpi. As described in **Fig. 4A**, either *Salmonella* or *E. coli* LPS was intraperitoneally injected on two consecutive days.

The reason for using aged mice was to simulate the systemic inflammation occurring in patients with sepsis because the majority of patients are over 65 years old (Prescott and Angus 2018). Given that aged brains displayed less ramified morphology of microglia and higher levels of IL-1β than young mice at baseline (Tejera *et al.* 2019; Youm *et al.* 2013), we expected that inflammatory responses to the endotoxin challenge might be exacerbated in old animals. Consistently, LPS injection into middle- and advanced-aged mice (12-24 months old) resulted in higher mortality, weight loss and production of inflammatory mediators in the brain and serum than young mice (3-6 months old) (Mouton *et al.* 2012; Kohman *et al.* 2010; Godbout *et al.* 2005). Notably, LPS-induced impairments of spatial memory and learning were more pronounced in old mice than in young mice (Kohman *et al.* 2010; Chen *et al.* 2008).

Meanwhile, cerebral effects of systemic inflammation were assessed at two points in time (i.e. 7 dpi and 63 dpi) because we were interested in modelling the long-term sequelae of sepsis in the brain as observed in sepsis survivors. Since not all the injected animals did not survive after the injection, as shown later in **Fig. 5A**, it was likely that data collected at the earlier timepoints would include non-surviving animals. The chronic effect was examined at two months post-injection due to the previous findings of synaptic destruction and loss of cortical dendritic spines in young animals (Kondo *et al.* 2011; Weberpals *et al.* 2009).

Regarding the bacterial strains of LPS used in this study, *Salmonella* and *E. coli* LPS were compared because a recent study demonstrated that *Salmonella* LPS tended to show more significant changes in pyramidal cell morphology in the hippocampus,

dendritic spine density and electrophysiological recordings than *E. coli* LPS at three months post-injection (Beyer *et al.* 2020). Since this study injected a lower concentration of endotoxin (0.2 mg/kg on two consecutive days), we hypothesised that higher dosages might aggravate these neuronal effects at 63 dpi.

Lastly, emerging evidence suggests that LPS injection on two consecutive days can enhance the neuroinflammatory responses without generating the immune tolerance in young mice in the wake of epigenetic modifications (Wendeln *et al.* 2018). Further, when young (2-3 months old) mice were challenged by the same dosage of *Salmonella* LPS on two consecutive days, hypothermia and increased mortality rate to approximately 10% within 7 dpi were previously documented (Mei *et al.* 2018). On this basis, we aimed to characterise the acute and chronic cerebral effects of systemic inflammation elicited by LPS prepared from two structurally distinct bacterial strains.

3.2 Increased mortality rate and weight loss after the endotoxin injection

Both *Salmonella* and *E. coli* LPS injections increased a mortality rate to 27.78% and 28.57% at 63 dpi, respectively (*Salmonella* LPS vs. Veh: $p = 0.025$; *E. coli* LPS vs. Veh: $p = 0.023$, log-rank (Mantel-Cox) test) (**Fig. 5A**). Importantly, deaths caused by LPS injections were not found from 7 dpi to 63 dpi, indicating that all the animals studied at 7 dpi and 63 dpi were survivors of the endotoxin challenge. Weight loss was observed in surviving animals from the day of the second injection to 7 dpi (*Salmonella* LPS vs. Veh: $p < 0.0001$ from the day of the second injection to 3 dpi, $p = 0.0002$ at 4 dpi, 0.045 at 5 dpi; *E. coli* LPS vs. Veh: $p < 0.0001$ from the day of the second injection to 5 dpi, $p = 0.0004$ at 6 dpi, $p = 0.038$ at 7 dpi, two-way repeated measures ANOVA) (**Fig. 5B**). Of note, the highest weight loss from the baseline weight was found at 1 dpi (*Salmonella* LPS: 85.79 ± 1.01% (mean ± SEM), *E. coli* LPS: 85.40 ± 0.69%, Veh: 98.11 ± 0.73%). From 7 dpi to 63 dpi, the weight was normalised to the baseline levels in both LPS-treated groups (**Fig. 5C**).

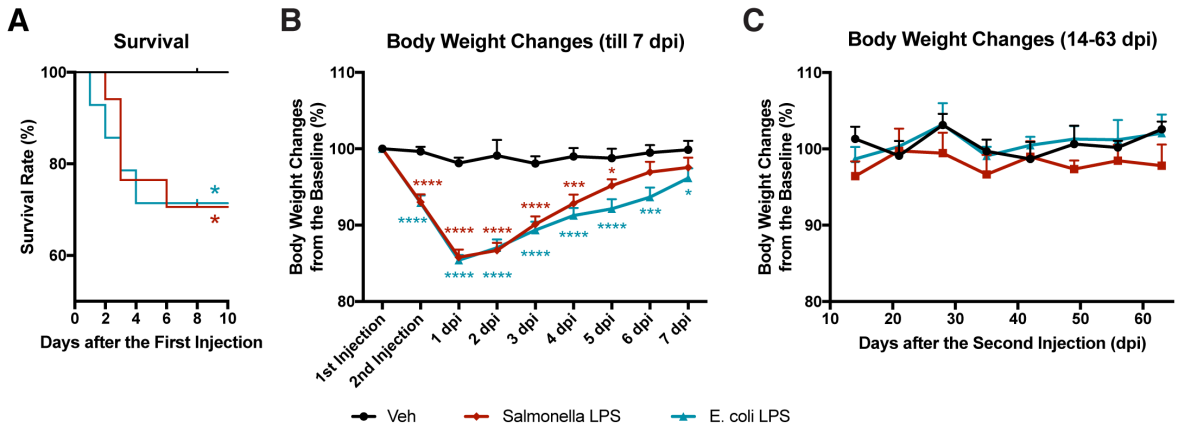

Figure 5. Increased mortality and weight loss until 7 dpi of 2xLPS.

(A) An increase in the mortality after the endotoxin challenge (vehicle (Veh) (black), n=16 mice; *Salmonella* LPS (red), n=18 mice; *E. coli* LPS (blue), n=14 mice, log-rank (Mantel-Cox) test, *Salmonella* (red) or *E. coli* LPS (blue) vs. Veh: **p* < 0.05).

(B) Immediate weight changes after the LPS injections (n=10 mice/treatment, two-way repeated measures ANOVA with a Tukey *post-hoc* test, *Salmonella* (red) or *E. coli* LPS (blue) vs. Veh at the respective timepoints: **p* < 0.05, ****p* < 0.001, *****p* < 0.0001). Data were mean ± SEM.

(C) Absence of the chronic weight changes from 14 dpi to 63 dpi (n=4 mice/ treatment, two-way repeated measures ANOVA with a Tukey *post-hoc* test). Data were mean ± SEM.

Abbreviations: dpi, days post-final injection; LPS, lipopolysaccharide.

3.3 Sustained neuroinflammation until 7 dpi of 2xLPS

3.3.1 Elevated cytokine levels and the NLRP3 inflammasome activation in the brain

Proinflammatory cytokine levels in the brains were assessed using western blot and ELISA to investigate whether some cytokines might be persistently elevated. The immunoblot analysis of IL-1β showed a trend of higher IL-1β levels in the *E. coli* LPS group than the vehicle and *Salmonella* LPS groups at 7 dpi (*Salmonella* LPS: 93.93 ± 7.97%, *E. coli* LPS: 124.70 ± 9.97%, Veh: 100.00 ± 6.74%; *E. coli* LPS vs. Veh: p = 0.054, *E. coli* LPS vs. *Salmonella* LPS: p = 0.012, two-way ANOVA, **Fig. 6A, B**). Because there was no such an increase at 63 dpi, it would be plausible that IL-1β levels were nearly normalised by 7 dpi in the brain. Another proinflammatory cytokine, CXCL1, was found to be elevated at 7 dpi of LPS, irrespective of the serotypes (*Salmonella* LPS: 40.69 ± 4.80 pg/mg, *E. coli* LPS: 59.26 ± 3.76 pg/mg, Veh: 26.91 ±

1.99 pg/mg; *Salmonella* LPS vs. Veh: $p = 0.028$, *E. coli* LPS vs. Veh: $p < 0.0001$, *E. coli* LPS vs. *Salmonella* LPS: $p = 0.004$, two-way ANOVA, **Fig. 6C**). Furthermore, IL-6 levels were detected in all the samples, and high levels were found only in the *E. coli* LPS group at 7 dpi (*Salmonella* LPS: 126.83 ± 4.46 pg/mg, *E. coli* LPS: 148.45 ± 5.30 pg/mg, Veh: 126.34 ± 5.52 pg/mg; *E. coli* LPS vs. Veh: $p = 0.019$, *E. coli* LPS vs. *Salmonella* LPS: $p = 0.023$, two-way ANOVA) and at 63 dpi (*Salmonella* LPS: 135.10 ± 5.52 pg/mg, *E. coli* LPS: 158.84 ± 3.52 pg/mg, Veh: 129.15 ± 8.65 pg/mg; *E. coli* LPS vs. Veh: $p = 0.007$, *E. coli* LPS vs. *Salmonella* LPS: $p = 0.024$, two-way ANOVA, **Fig. 6D**). Meanwhile, IL-5 levels were found to be normal at 7 dpi and 63 dpi (data not shown). Some cytokines, such as IL-1β, IL-4 and IFN-γ, were detected at borderline levels of the quantification using ELISA, thus the reliability of the data was considered to be low. The other cytokines (namely, TNF-α, IL-2, IL-10 and IL-12p70) were not detected.

In order to verify the increase in IL-1β levels at 7 dpi, additional indicators of the NLRP3 inflammasome pathway were examined using western blot. While the cleaved caspase-1 levels were found to be normal, ASC protein levels were elevated after the *E. coli* LPS injection (*Salmonella* LPS: 134.33 ± 11.84%, *E. coli* LPS: 160.20 ± 15.20%, Veh: 100.00 ± 11.83%; *E. coli* LPS vs. Veh: $p = 0.015$, one-way ANOVA, **Fig. 6E-G**), supporting that the *E. coli* LPS injection might have produced greater or longer activation of the NLRP3 inflammasome than the *Salmonella* LPS.

Overall, a few cytokine levels were maintained at relatively higher levels in the brain at 7 dpi, indicating that neuroinflammation persisted by 7 dpi. Of note, the *E. coli* LPS injection seemed to produce the strongest effects on the IL-1β, CXCL1, IL-6 and ASC levels in the brain. Except for IL-6 in the *E. coli* LPS group at 63 dpi, all the cytokine levels were normalised or found below the limits of reliable detection. This suggested that neuroinflammation may not have lasted for two months after the injection.

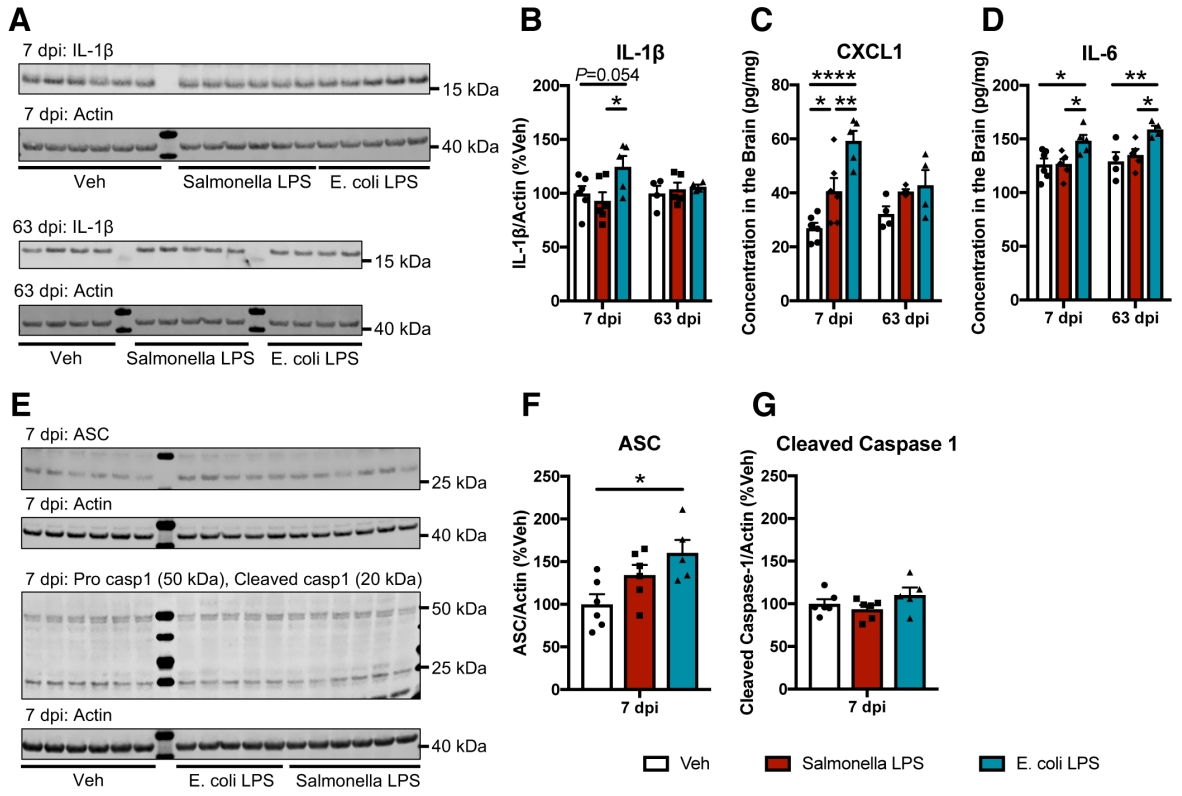

Figure 6. Cytokine increase and NLRP3 inflammasome activation.

(A, B) Western blot analysis of mature IL-1β levels in the brain. There was an increasing trend at 7 dpi of *E. coli* LPS. No such findings were observed at 63 dpi (n=5-6 mice, two-way ANOVA with a Tukey *post-hoc* test, **p* < 0.05).

(C, D) Quantification of proinflammatory cytokine levels in the brain using ELISA. A temporal increase in CXCL1 levels was observed at 7 dpi of both LPS serotypes. A persistent serotype-related increase in IL-6 levels was also found at 7 dpi and 63 dpi of *E. coli* LPS (n=4-6 mice, two-way ANOVA with a Tukey *post-hoc* test, **p* < 0.05, ***p* < 0.01, *****p* < 0.0001). Data were expressed as mean ± SEM.

(E-G) Western blot analysis of NLRP3 inflammasome activation in the brain at 7 dpi. Whilst cleaved caspase-1 levels were normal, ASC levels were found to be elevated after *E. coli* LPS injections (n=5-6 mice, one-way ANOVA with a Tukey *post-hoc* test, **p* < 0.05). Data were expressed as mean ± SEM.

Abbreviations: ASC, apoptosis-associated speck-like protein containing a C-terminal caspase recruitment domain; CXCL1, C-X-C motif chemokine ligand 1; dpi, days post-final injection; ELISA, enzyme-linked immunosorbent assay; IL, interleukin; LPS, lipopolysaccharide; NLRP3, nucleotide-binding domain, the leucine-rich repeat, and the pyrin domain containing protein 3.

3.3.2 Observations of less ramified microglia at 7 dpi

To complement the persisting neuroinflammation at 7 dpi, microglial morphology was studied at the single-cell level in the hippocampus using skeleton analysis. During image acquisition using a super-resolution microscope, the Iba1-positive microglial cells, of which complete structure was visible in z-stacks, were individually located to the centre of the field of view. The resulting 8-9 cells per animal in the CA1 or CA3 hippocampal subfields were manually isolated from the image stacks.

At 7 dpi, microglia in CA1 showed shorter branch length and fewer junctions, branches and process end-points after both *Salmonella* and *E. coli* LPS injections, indicating the morphological alterations persisting by 7 dpi (Total branch length — *Salmonella* LPS vs. Veh: $p = 0.012$, *E. coli* LPS vs. Veh: $p = 0.008$; Total branch number — *Salmonella* LPS vs. Veh: $p = 0.015$, *E. coli* LPS vs. Veh: $p = 0.003$; Total junction number — *Salmonella* LPS vs. Veh: $p = 0.044$, *E. coli* LPS vs. Veh: $p = 0.002$; Total process endpoints — *Salmonella* LPS vs. Veh: $p < 0.0001$, *E. coli* LPS vs. Veh: $p = 0.001$, Kruskal-Wallis test, **Fig. 7A-E, I, Table 9**).

Microglia in CA3 region also demonstrated similar, but less significant, differences of morphology after LPS injections, indicating that there might be regional differences of microglial morphology between CA1 and CA3 subfields (Total branch length — *E. coli* LPS vs. Veh: $p = 0.027$; Total branch number — *E. coli* LPS vs. Veh: $p = 0.004$; Total junction number — *E. coli* LPS vs. Veh: $p = 0.005$, Total process endpoints — *E. coli* LPS vs. Veh: $p = 0.029$, Kruskal-Wallis test, **Fig. 7A, B, F-H, J, Table 9**).

Meanwhile, none of the morphological parameters of CA1 and CA3 microglia significantly differed from the control group at 63 dpi (**Fig. 7C-J, Table 9**). Given that many of the comparisons between 7 dpi and 63 dpi among LPS-treated mice showed a normalising tendency, these results confirmed that the morphological changes did not persist in old mice and were normalised by 63 dpi in CA1 (Total branch length — *Salmonella* LPS at 7 dpi vs. *Salmonella* LPS at 63 dpi: $p < 0.0001$, *E. coli* LPS at 7 dpi vs. *E. coli* LPS at 63 dpi: $p = 0.004$; Total branch number — *Salmonella* LPS at 7 dpi vs. *Salmonella* LPS at 63 dpi: $p = 0.0003$, *E. coli* LPS at 7 dpi vs. *E. coli* LPS at 63 dpi: $p = 0.0003$; Total junction number — *Salmonella* LPS at 7 dpi vs. *Salmonella* LPS at 63 dpi: $p = 0.0009$, *E. coli* LPS at 7 dpi vs. *E. coli* LPS at 63 dpi: $p < 0.0001$; Total

process endpoints — *Salmonella* LPS at 7 dpi vs. *Salmonella* LPS at 63 dpi: $p < 0.0001$, *E. coli* LPS at 7 dpi vs. *E. coli* LPS at 63 dpi: $p = 0.051$, Kruskal-Wallis test, **Fig. 7C-E, I, Table 9**) and in CA3 (Total branch number — *E. coli* LPS at 7 dpi vs. *E. coli* LPS at 63 dpi: $p = 0.024$; Total junction number — *E. coli* LPS at 7 dpi vs. *E. coli* LPS at 63 dpi: $p = 0.019$, Kruskal-Wallis test, **Fig. 7F-H, J, Table 9**).

Microglial density was quantified in CA1 and CA3 subregions because the presence of a higher number of microglia can cumulatively contribute to increasing cytokine levels and removing synaptic structures, even if the phagocytic activity may not be heightened at the single-cell levels. Nevertheless, this analysis did not uncover clear differences from the control groups in CA1 and CA3 at 7 dpi and 63 dpi (**Fig. 7K**), suggesting that the number of microglia was not chronically altered in the hippocampus and did not produce additive neurotoxic effects due to the higher density of microglia.

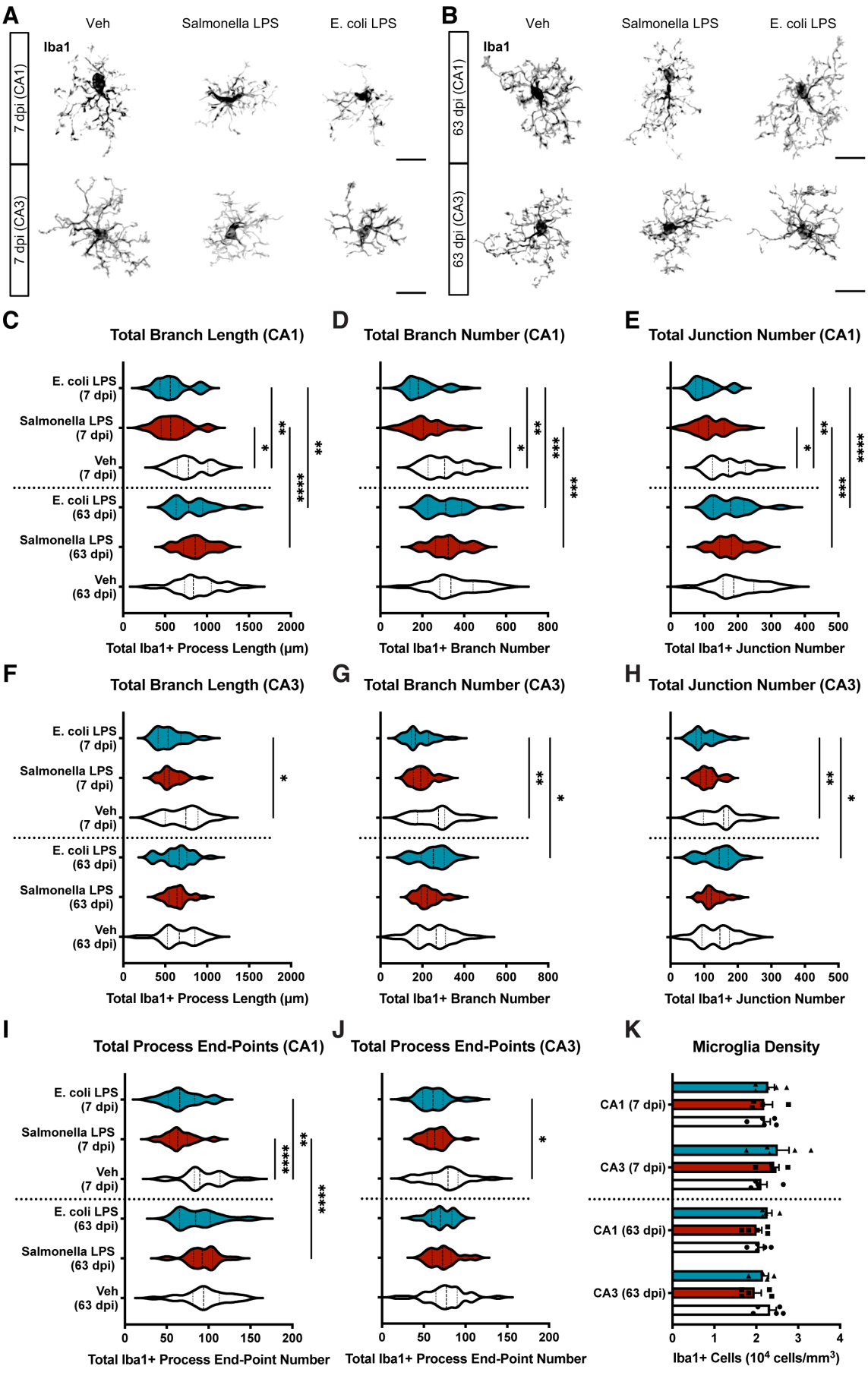
A
Veh
Salmonella LPS
E. coli LPS
Iba1
7 dpi (CA1)
7 dpi (CA3)
B
Veh
Salmonella LPS
E. coli LPS
Iba1
63 dpi (CA1)
63 dpi (CA3)
C
Total Branch Length (CA1)
E. coli LPS (7 dpi)
Salmonella LPS (7 dpi)
Veh (7 dpi)
E. coli LPS (63 dpi)
Salmonella LPS (63 dpi)
Veh (63 dpi)
0 500 1000 1500 2000
Total Iba1+ Process Length (µm)
D
Total Branch Number (CA1)
0 200 400 600 800
Total Iba1+ Branch Number
E
Total Junction Number (CA1)
0 100 200 300 400 500
Total Iba1+ Junction Number
F
Total Branch Length (CA3)
G
Total Branch Number (CA3)
H
Total Junction Number (CA3)
I
Total Process End-Points (CA1)
0 50 100 150 200
Total Iba1+ Process End-Point Number
J
Total Process End-Points (CA3)
K
Microglia Density
CA1 (7 dpi)
CA3 (7 dpi)
CA1 (63 dpi)
CA3 (63 dpi)
0 1 2 3 4
Iba1+ Cells (10^4 cells/mm^3)
Veh
Salmonella LPS
E. coli LPS

(See figure on previous page.)

Figure 7. Transient morphological changes of microglia in CA1 and CA3 at 7 dpi.

(A, B) Representative images of the isolated microglia in CA1 and CA3 at 7 dpi and 63 dpi. Less ramified morphology of microglia was seen at 7 dpi of LPS. Scale bar = 20 μm.

(C-J) Violin plots with median and interquartile range obtained from the skeleton analysis of microglia in (C-E, I) CA1 and (F-H, J) CA3 at 7 dpi and 63 dpi. The total length of branches (C, F) and the total number of (D, G) branches, (E, H) junctions and (I, J) process end-points indicated that the less ramified morphology of microglia was observed in CA1 and CA3 at 7 dpi but later returned to the normal by 63 dpi (n=24-36 cells from 3-4 mice, Kruskal-Wallis test with a Dunn's *post-hoc* test, *p < 0.05, **p < 0.01, ***p < 0.001, ****p < 0.0001).

(K) The normal density of microglia in CA1 and CA3 subfields at 7 dpi and 63 dpi (n=4-5 mice, two-way ANOVA with a Tukey *post-hoc* test). Data were expressed as mean ± SEM.

Abbreviations: dpi, days post-final injection; LPS, lipopolysaccharide.

Table 9. Summary of the skeleton analysis of microglia.

	7 dpi			63 dpi		
	Veh	***Salm.* LPS**	***E. coli* LPS**	**Veh**	***Salm.* LPS**	***E. coli* LPS**
CA1 microglia						
Total branch length (μm)	778.80 [644.79, 1012.08]	566.59 [453.03, 722.79]	562.13 [439.63, 666.59]	837.56 [731.73, 1051.22]	861.25 [721.12, 980.81]	780.68 [631.75, 950.32]
Total branch number	306.50 [277.75, 393.00]	205.00 [154.50, 273.00]	181.50 [141.00, 241.50]	337.00 [283.25, 442.50]	323.50 [263.00, 378.00]	312.00 [227.00, 387.50]
Total junction number	173.00 [125.00, 223.00]	113.00 [83.00, 159.00]	96.00 [74.00, 128.00]	188.50 [156.50, 248.50]	182.00 [146.00, 215.25]	179.00 [127.00, 218.75]
Total process end-points	89.50 [83.00, 113.75]	63.00 [53.50, 74.50]	65.50 [51.75, 83.25]	94.00 [81.25, 112.75]	92.50 [82.00, 104.75]	84.50 [65.25, 102.00]
CA3 microglia						

Total branch length (μm)	745.29 [499.47, 891.82]	546.22 [487.59, 663.85]	535.24 [414.89, 686.70]	666.85 [526.54, 853.61]	640.76 [544.62, 701.19]	665.45 [541.01, 756.65]
Total branch number	277.00 [176.00, 306.00]	192.00 [157.00, 227.00]	166.50 [147.25, 229.50]	266.00 [178.50, 310.00]	223.00 [194.00, 265.75]	252.00 [194.00, 304.50]
Total junction number	158.00 [98.00, 173.00]	106.00 [89.00, 124.00]	91.50 [76.00, 127.75]	147.00 [93.50, 175.50]	121.00 [107.25, 146.50]	145.00 [105.75, 172.25]
Total process end-points	79.00 [60.00, 91.00]	63.00 [54.00, 73.00]	61.00 [48.75, 73.00]	77.00 [64.50, 90.00]	72.50 [60.00, 82.50]	70.00 [59.50, 83.75]

Data were expressed as median [interquartile range].

Abbreviations: dpi, days post-final injection; LPS, lipopolysaccharide.

3.4 No LPS effects on neuron and myelin density in the hippocampus

The stereological analysis of pyramidal cell density in CA1 and CA3 was performed. This revealed that both of the LPS serotypes did not decrease the neuron density in CA1 and CA3 at 7 dpi and 63 dpi (**Fig. 8A, E)**. We also sought for LPS-induced selective interneuron death or myelin loss, but the PV-positive interneuron density and MOG-positive area remained unchanged in CA1 and CA3 at 7 dpi and 63 dpi (**Fig. 8B, C, F, G**). Finally, apoptosis of every cell type was examined by TUNEL staining of the hippocampus. We found that less than two apoptotic nuclei per 40x confocal micrographs were only observable in CA1 at 7 dpi (**Fig. 8D**). This provided evidence against the increased apoptosis rate in CA1 at 7 dpi, which supported the earlier data concerning the neuron and myelin density in the same regions.

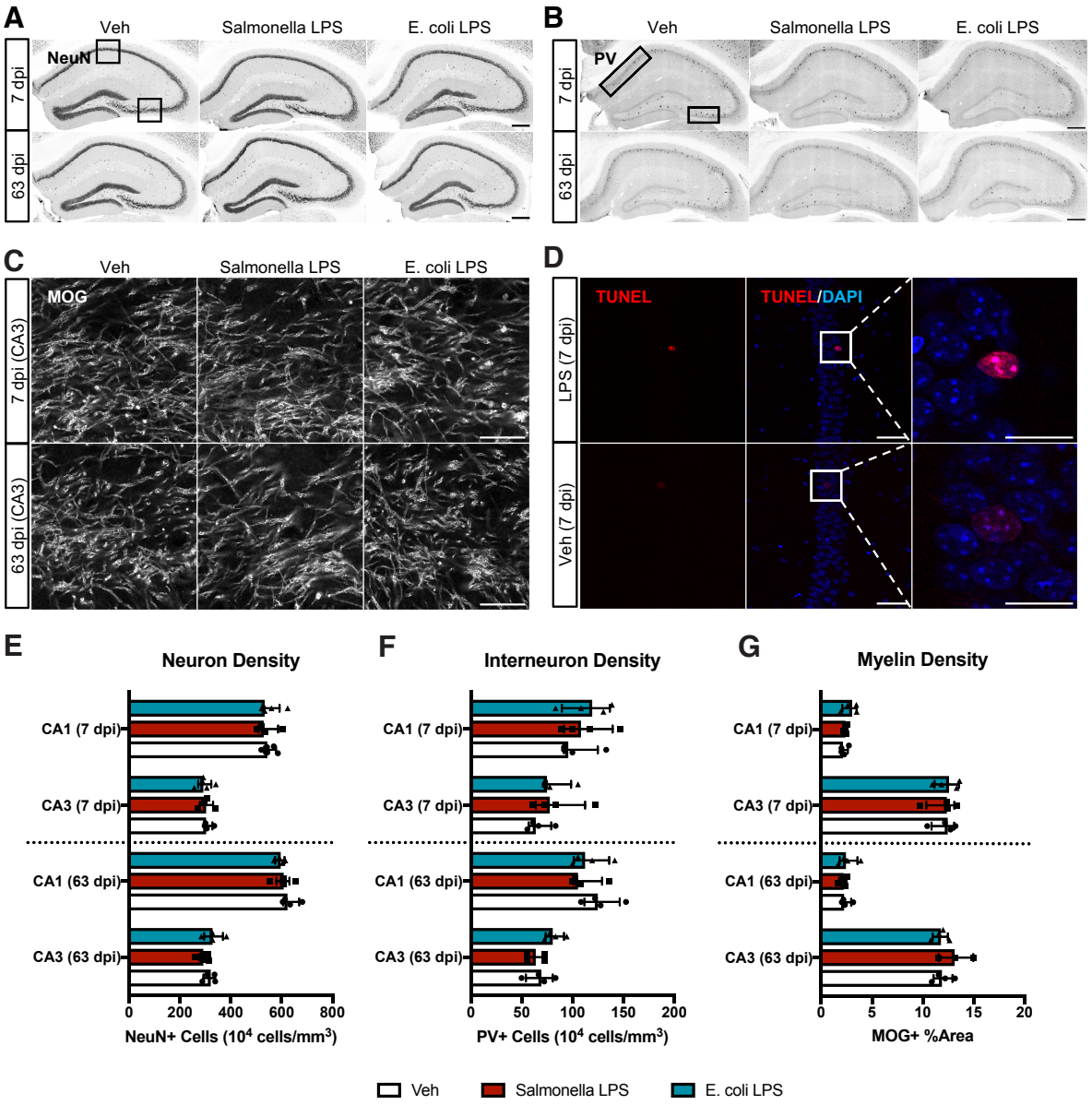

Figure 8. Normal neuron and myelin density in CA1 and CA3 at 7 dpi and 63 dpi.

(A, B) Representative images of the (A) NeuN-positive neurons and (B) PV-positive interneurons in the hippocampus at 7 dpi and 63 dpi. Cell nuclei were counted in the rectangles. Scale bar = 100 μm.

(C) Representative images of MOG-positive signals in CA3 at 7 dpi and 63 dpi. Scale bar = 20 μm.

(D) A rare observation of TUNEL-positive apoptotic nuclei in CA1 at 7 dpi. Scale bar = 50 μm (middle) and 10 μm (right).

(E, F) Normal (E) neuron and (F) interneuron density in CA1 and CA3 at 7 dpi and 63 dpi (n=4-5 mice).

(G) Normal MOG-positive area in CA1 and CA3 at 7 dpi and 63 dpi (n=4 mice).
All the statistical analysis presented here used a Kruskal-Wallis test with a Dunn's *post-hoc* test. Data were expressed as median ± interquartile range.
Abbreviations: dpi, days post-final injection; LPS, lipopolysaccharide; MOG, myelin oligodendrocyte glycoprotein; PV, parvalbumin; TUNEL, terminal deoxynucleotidyl transferase dUTP nick end labelling.

3.5 Local, rather than global, synapse loss after systemic inflammation

3.5.1 Little evidence for global synapse loss at 7 dpi and 63 dpi

We isolated synaptosomes from the hemibrains and performed immunoblot analysis to study the synaptic protein changes after the systemic inflammation. Our findings indicated that there were no dramatic changes in excitatory and inhibitory synaptic proteins at 7 dpi and 63 dpi. The only difference we observed was PSD95 protein levels between *Salmonella* LPS and *E. coli* LPS at 7 dpi (PSD95: *Salmonella* LPS: 111.14 ± 6.88%, *E. coli* LPS: 90.29 ± 3.67%, Veh: 100 ± 2.99%; *Salmonella* LPS vs. *E. coli* LPS: p = 0.012, two-way ANOVA, **Fig. 9**).

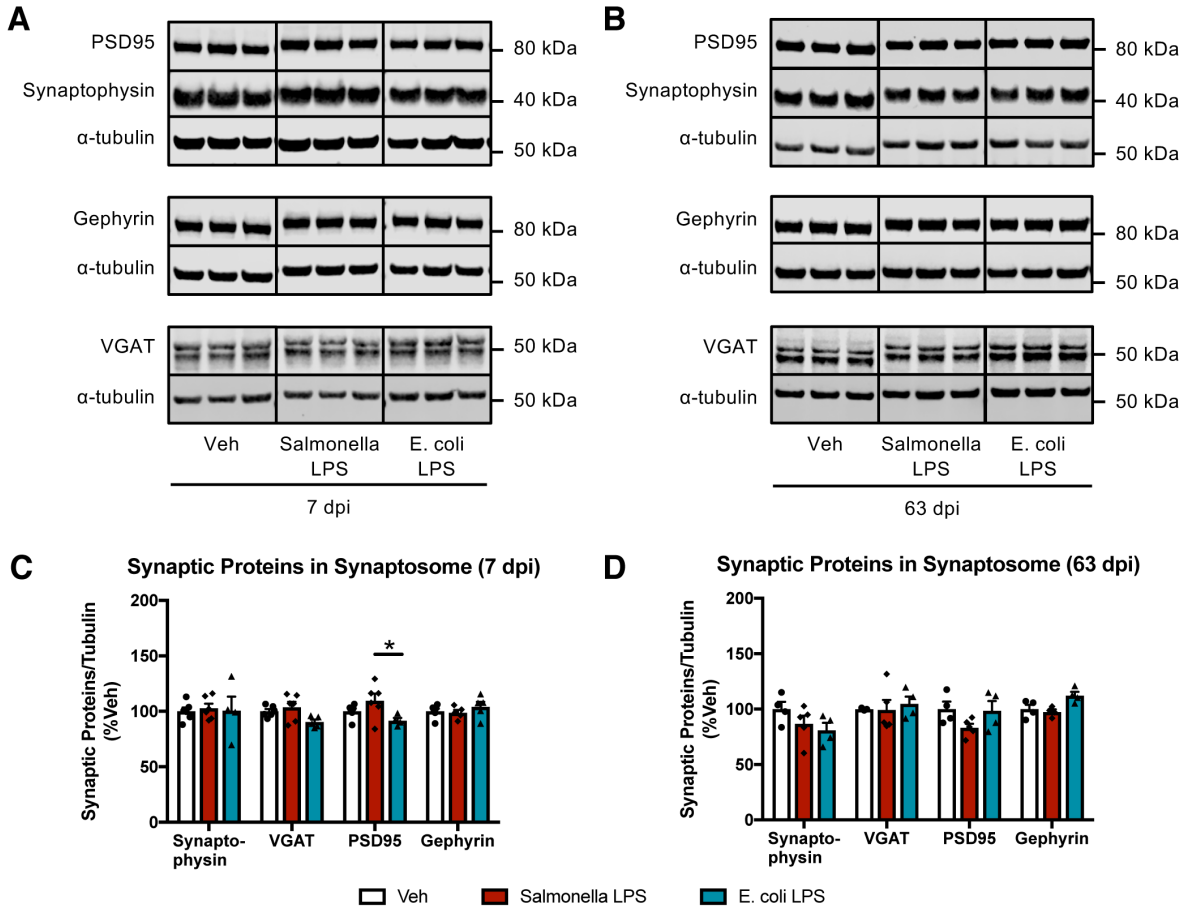

(See figure on previous page.)

Figure 9. No overt changes in global synaptic proteins at 7 dpi and 63 dpi.

(A, B) Immunoblot images for excitatory (PSD95), inhibitory (VGAT and gephyrin) and non-specific synaptic proteins (synaptophysin) in synaptosomes isolated from the hemibrains at 7 dpi and 63 dpi.

(C, D) No overt reduction of synaptic proteins at 7 dpi and 63 dpi (n=4-6 mice, two-way ANOVA with a Tukey *post-hoc* test, *$p < 0.05$). Data were expressed as mean ± SEM.

Abbreviations: dpi, days post-final injection; LPS, lipopolysaccharide; PSD95, postsynaptic protein density 95; VGAT, vesicular GABA transporter.

3.5.2 Delayed reduction of excitatory synaptic puncta in CA3 at 63 dpi

Because the analysis of synaptosomes, prepared from the hemibrains, was only able to assess global changes of synaptic proteins, we then moved on to histological analysis of synaptic puncta, proteins accumulated at synaptic structures, in the hippocampus. Due to the point spread function elongation, the immunofluorescent signals of the synaptic puncta became an ellipsoid shape at the diameter of 300-600 nm on microscopic z-stacks (Broadhead *et al.* 2016). A recently developed super-resolution microscope with an Airyscan detector has sufficient axial and lateral spatial resolutions (r_{xy} = 140 nm and r_z = 400 nm) for imaging these fluorescent signals (Huff 2015), and hence this microscope was chosen for the synaptic puncta analysis.

We observed normal density of the excitatory synaptic puncta (VGLUT2 and PSD95) in CA1, dentate gyrus (DG) and CA3 regions of the hippocampus at 7 dpi (**Fig. 10A, C-E**). Likewise, the synaptic puncta density in CA1 and DG were normal at 63 dpi (**Fig. 10C-E**). In contrast, the CA3 subfield demonstrated a clear reduction of both presynaptic and postsynaptic puncta and their colocalisation at 63 dpi (VGLUT2 — *Salmonella* LPS: 48.53 ± 2.67 puncta/100 µm^2, *E. coli* LPS: 41.81 ± 1.35 puncta/100 µm^2, Veh: 75.14 ± 0.75 puncta/100 µm^2; *Salmonella* LPS vs. Veh: $p < 0.0001$, *E. coli* LPS vs. Veh: $p < 0.0001$; PSD95 — *Salmonella* LPS: 25.13 ± 0.27 puncta/100 µm^2, *E. coli* LPS: 21.40 ± 0.68 puncta/100 µm^2, Veh: 35.91 ± 1.40 puncta/100 µm^2; *Salmonella* LPS vs. Veh: $p < 0.0001$, *E. coli* LPS vs. Veh: $p < 0.0001$, *Salmonella* LPS vs. *E. coli* LPS: $p = 0.044$; Colocalisation — *Salmonella* LPS: 2.44 ±

0.17 puncta/100 µm^2, *E. coli* LPS: 1.96 ± 0.11 puncta/100 µm^2, Veh: 4.82 ± 0.35 puncta/100 µm^2; *Salmonella* LPS vs. Veh: $p < 0.0001$, *E. coli* LPS vs. Veh: $p < 0.0001$, two-way ANOVA, **Fig. 10B-E**).

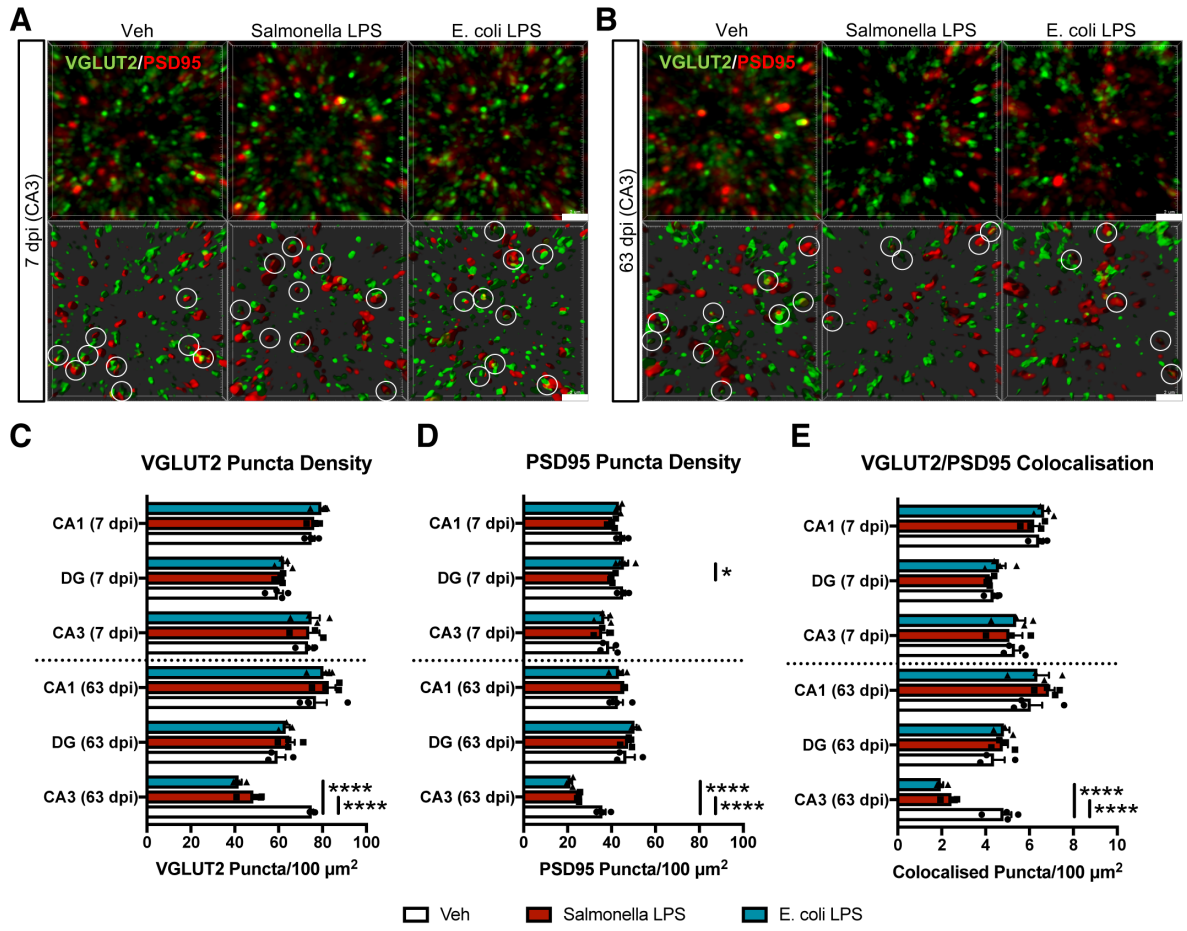

Figure 10. Reduced CA3 excitatory synaptic puncta density at 63 dpi.

(A, B) Representative super-resolution images of VGLUT2 (green) and PSD95 (red) puncta in CA3 at (A) 7 dpi and (B) 63 dpi. The three-dimensional reconstructions of two adjacent z-planes indicated colocalisation of pre- and post-synaptic puncta (white circles). It should be noted that some of the synaptic puncta were counted multiple times if being detected in adjacent z-planes. Scale bar = 2 µm.

(C-E) Delayed reduction of excitatory synaptic puncta density in CA3, but not CA1 and DG, at 63 dpi (n=3-4 mice, two-way ANOVA with a Tukey *post-hoc* test, *$p < 0.05$, ****$p < 0.0001$).

Data were expressed as mean ± SEM.

Abbreviations: dpi, days post-final injection; DG, dentate gyrus; LPS, lipopolysaccharide; PSD95, postsynaptic protein density 95; VGLUT2, vesicular glutamate transporter 2.

In the meantime, inhibitory synapses (VGAT and gephyrin) were similarly studied in the hippocampus. Results showed that there were little changes in the VGAT area and gephyrin puncta denisty in CA1, CA3 and DG at 7 dpi and 63 dpi (**Fig. 11**). This implied that the synapse loss in CA3 at 63 dpi might be specific to excitatory synapses.

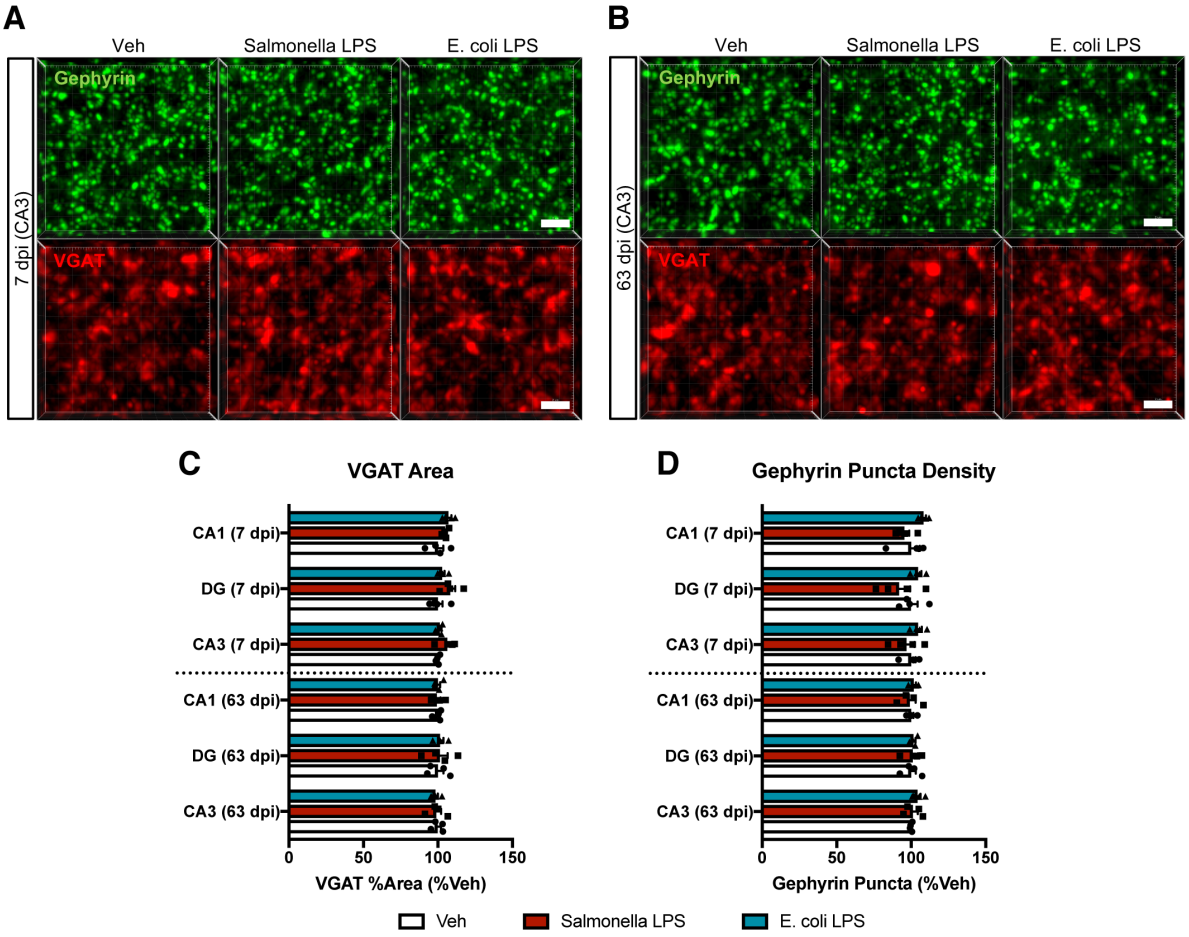

Figure 11. Normal inhibitory synaptic puncta density at 7 dpi and 63 dpi.

(A, B) Representative super-resolution images of gephyrin puncta (green) and VGAT signals (red) in CA3 at (A) 7 dpi and (B) 63 dpi. Scale bar = 2 μm.

(C, D) Normal gephyrin puncta density and VGAT-positive area in CA1, CA3 and DG at 7 dpi and 63 dpi (n=4 mice, two-way ANOVA with a Tukey *post-hoc* test). Data were expressed as mean ± SEM.

Abbreviations: dpi, days post-final injection; DG, dentate gyrus; LPS, lipopolysaccharide; VGAT, vesicular GABA transporter.

3.5.3 No enhancement of synaptic pruning by microglia in CA3 at 7 dpi and 63 dpi

Synaptic pruning by microglia was studied so as to elucidate how excitatory synapses were reduced in CA3. To this end, we reconstructed microglial cells and CD68-positive microglial lysosomes in the three-dimension from the super-resolution image stacks and finally isolated the PSD95-positive synaptic puncta inside the lysosomes (**Fig. 12A**). We found that the mean volume of the lysosomes elevated in CA1 and CA3 microglia only at 7 dpi, compared with the control microglia (CA1 — *Salmonella* LPS vs. Veh: $p = 0.003$, *E. coli* LPS vs. Veh: $p < 0.0001$; CA3 — *E. coli* LPS vs. Veh: $p = 0.032$, Kruskal-Wallis test, **Fig. 12B, E; Table 10**). However, the total volume of lysosomes remained normal at 7 dpi and 63 dpi of LPS (**Fig. 12C, F; Table 10**), indicating that the higher mean lysosome volumes at 7 dpi might have resulted from the clustering of lysosomes.

In order to investigate the synaptic pruning by microglia, the engulfed PSD95 puncta density per lysosome volume was assessed. This analysis showed that fewer synaptic puncta were detected at 7 dpi and 63 dpi of LPS, indicating that the synaptic pruning by CA1 microglia might have been attenuated by the LPS injection (7 dpi: *Salmonella* LPS vs. Veh: $p = 0.0005$; 63 dpi: *Salmonella* LPS vs. Veh: $p = 0.010$, *E. coli* LPS vs. Veh: $p = 0.017$, Kruskal-Wallis test, **Fig. 12A, D, G; Table 10**). On the other hand, little changes of synaptic pruning were observed in CA3 at 7 dpi and 63 dpi (**Fig. 12A, D, G; Table 10**), highlighting that the CA3 excitatory synapse loss might not be attributed to the changes in synaptic pruning by microglia in the same region.

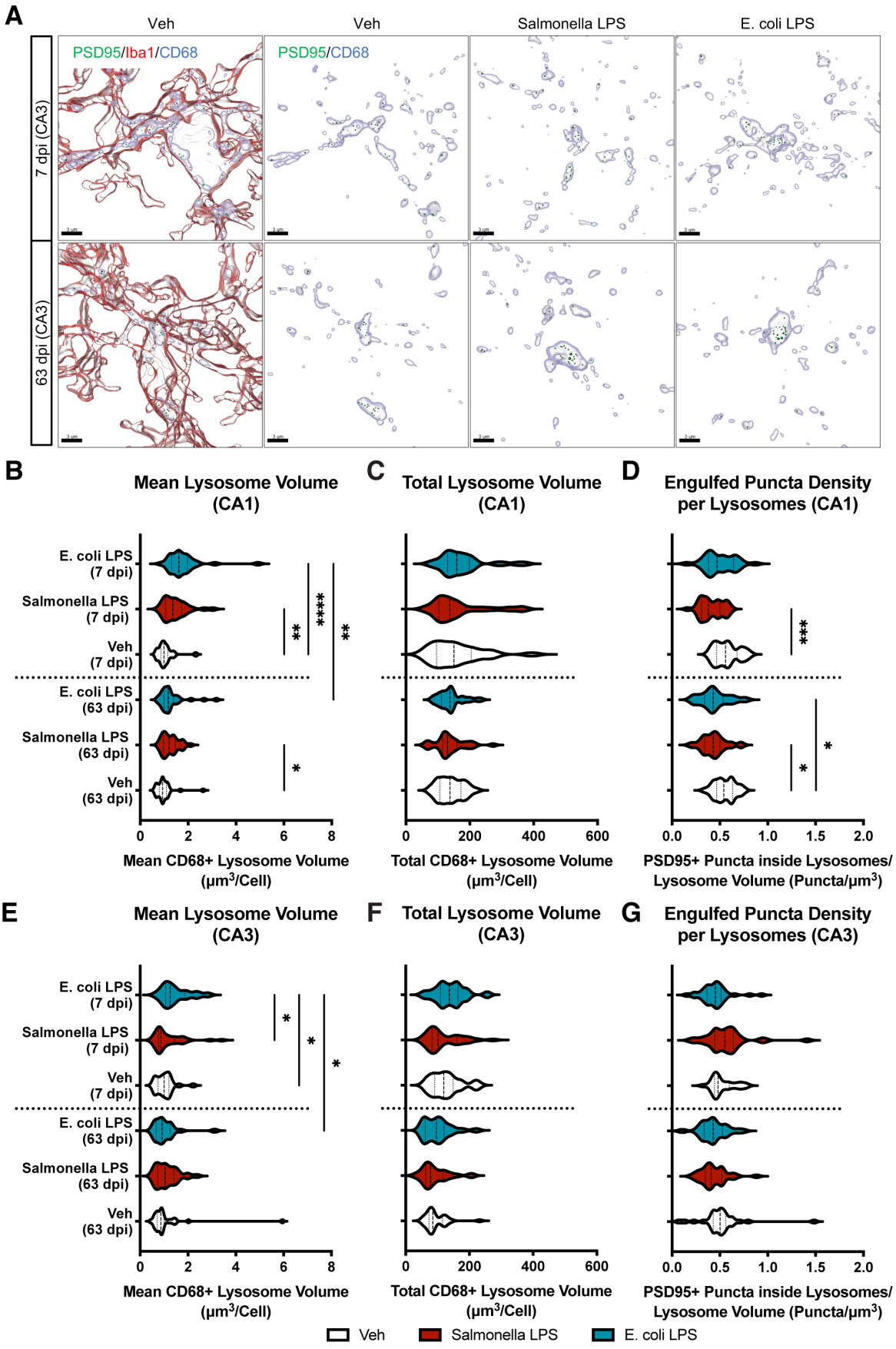
A
Veh
Veh
Salmonella LPS
E. coli LPS
7 dpi (CA3)
63 dpi (CA3)
PSD95/Iba1/CD68
PSD95/CD68
B
Mean Lysosome Volume (CA1)
C
Total Lysosome Volume (CA1)
D
Engulfed Puncta Density per Lysosomes (CA1)
E. coli LPS (7 dpi)
Salmonella LPS (7 dpi)
Veh (7 dpi)
E. coli LPS (63 dpi)
Salmonella LPS (63 dpi)
Veh (63 dpi)
Mean CD68+ Lysosome Volume (µm³/Cell)
Total CD68+ Lysosome Volume (µm³/Cell)
PSD95+ Puncta inside Lysosomes/ Lysosome Volume (Puncta/µm³)
E
Mean Lysosome Volume (CA3)
F
Total Lysosome Volume (CA3)
G
Engulfed Puncta Density per Lysosomes (CA3)
Veh
Salmonella LPS
E. coli LPS

(See figure on previous page.)

Figure 12. Normal or reduced synaptic pruning by microglia at 7 dpi and 63 dpi.

(A) Representative three-dimensional reconstruction of the single microglia in CA3 (red), microglial lysosomes (blue) and engulfed PSD95 puncta inside lysosomes (green). Scale bar = 3 μm.

(B, E) Higher volumes of mean CD68-positive lysosomes in (B) CA1 and (E) CA3 microglia at 7 dpi, but not at 63 dpi (except for *Salmonella* LPS in CA1) (n=24-36 cells from 3-4 mice).

(C, F) Normal volume of total CD68-positive lysosomes in (C) CA1 and (F) CA3 microglia at 7 dpi and 63 dpi (n=24-36 cells from 3-4 mice).

(D, G) Normal or reduced levels of synaptic pruning by (D) CA1 and (G) CA3 microglia at 7 dpi and 63 dpi (n=24-36 cells from 3-4 mice).

All the statistical analyses shown in panels **B-G** used a Kruskal-Wallis test with a Dunn's *post-hoc* test (*$p < 0.05$, **$p < 0.01$, ***$p < 0.001$, ****$p < 0.0001$). Violin plots indicated the median and interquartile range.

Abbreviations: dpi, days post-final injection; LPS, lipopolysaccharide; PSD95, postsynaptic protein density 95.

Table 10. Summary of microglial lysosomes and synaptic pruning.

	7 dpi			**63 dpi**		
	Veh	***Salm.* LPS**	***E. coli* LPS**	**Veh**	***Salm.* LPS**	***E. coli* LPS**
CA1 microglia						
Mean lysosome volume (μm^3)	0.99 [0.86, 1.15]	1.36 [1.06, 1.73]	1.61 [1.31, 1.97]	0.93 [0.80, 1.09]	1.20 [0.97, 1.46]	1.17 [0.99, 1.39]
Total lysosome volume (μm^3)	150.56 [96.04, 204.79]	137.24 [103.50, 186.01]	159.49 [130.46, 198.31]	137.94 [106.39, 172.68]	130.30 [114.84, 159.64]	137.83 [111.41, 150.72]
Engulfed puncta (puncta/μm^3)	0.56 [0.47, 0.68]	0.38 [0.31, 0.50]	0.47 [0.38, 0.64]	0.54 [0.47, 0.63]	0.43 [0.34, 0.50]	0.43 [0.34, 0.53]
CA3 microglia						
Mean lysosome volume (μm^3)	1.00 [0.75, 1.20]	0.87 [0.77, 1.45]	1.26 [1.07, 1.87]	0.87 [0.71, 1.00]	1.04 [0.74, 1.42]	0.92 [0.67, 1.26]

Total lysosome volume (μm^3)	119.52 [90.85, 149.10]	101.62 [82.73, 160.70]	137.01 [109.34, 164.23]	85.57 [73.41, 115.76]	78.05 [62.83, 117.62]	96.32 [61.53, 120.60]
Engulfed puncta (puncta/μm^3)	0.48 [0.44, 0.60]	0.55 [0.45, 0.64]	0.45 [0.37, 0.51]	0.50 [0.43, 0.56]	0.41 [0.35, 0.52]	0.43 [0.33, 0.53]

Data were expressed as median [interquartile range].

Abbreviations: dpi, days post-final injection; LPS, lipopolysaccharide.

3.5.4 Reduction of synaptic complement factor C3 in CA3 at 63 dpi

To investigate whether the complement pathway may be involved in synapse loss and synaptic pruning, the density of complement factor C3, was analysed in the hippocampus. Similar to the data on excitatory synaptic puncta, the total C3 puncta density was normal in CA1, CA3 and DG subfields at 7 dpi; and CA1 and DG at 63 dpi (**Fig. 13A-C**). However, the density significantly reduced in CA3 at 63 dpi (*Salmonella* LPS: 17.63 ± 1.15 puncta/100 μm^2, *E. coli* LPS: 15.81 ± 0.46 puncta/100 μm^2, Veh: 29.29 ± 2.60 puncta/100 μm^2; *Salmonella* LPS vs. Veh: $p < 0.0001$, *E. coli* LPS vs. Veh: $p < 0.0001$, two-way ANOVA, **Fig. 13A-C**). Similarly, fewer synaptic C3 puncta colocalised with one of excitatory synaptic puncta (VGLUT2 or PSD95) were found in CA3 at 63 dpi (C3 colocalised with VGLUT2: *Salmonella* LPS: 3.54 ± 0.02 puncta/100 μm^2, *E. coli* LPS: 3.20 ± 0.14 puncta/100 μm^2, Veh: 6.67 ± 0.57 puncta/100 μm^2; *Salmonella* LPS vs. Veh: $p < 0.0001$, *E. coli* LPS vs. Veh: $p < 0.0001$; C3 colocalised with PSD95 — *Salmonella* LPS: 0.89 ± 0.05 puncta/100 μm^2, *E. coli* LPS: 0.76 ± 0.04 puncta/100 μm^2, Veh: 1.91 ± 0.20 puncta/100 μm^2; *Salmonella* LPS vs. Veh: $p < 0.0001$, *E. coli* LPS vs. Veh: $p < 0.0001$, two-way ANOVA, **Fig. 13D, E**). In contrast, the synaptic C3 puncta density was found to be normal in CA1, CA3 and DG at 7 dpi, and CA1 and DG at 63 dpi (**Fig. 13D, E**).

Furthermore, the proportions of C3-coated excitatory synaptic puncta were quantified at 7 dpi and 63 dpi (**Fig. 13F, G**). Results indicated that the proportion of C3-coated VGLUT2 and PSD95 decreased in CA3 at 63 dpi (Ratio of C3-tagged VGLUT2 over total VGLUT2 — *Salmonella* LPS: 7.91 ± 0.53%, *E. coli* LPS: 7.47 ± 0.07%, Veh: 9.16 ± 0.32%; *E. coli* LPS vs. Veh: $p = 0.010$; Ratio of C3-tagged PSD95 over total PSD95 — *Salmonella* LPS: 3.51 ± 0.18%, *E. coli* LPS: 3.44 ± 0.15%, Veh: 5.13 ± 0.38%; *Salmonella* LPS vs. Veh: $p = 0.0007$, *E. coli* LPS vs. Veh: $p = 0.0004$, two-way ANOVA, **Fig. 13F, G**).

Altogether, these data suggested that the number of C3-tagged synapses declined over time in CA3 between 7 dpi and 63 dpi, and assuming that microglia recognised and eliminated these C3-tagged synapses, these data supported the hypothesis for the role of microglia in CA3-specific synapse loss following endotoxin injection.

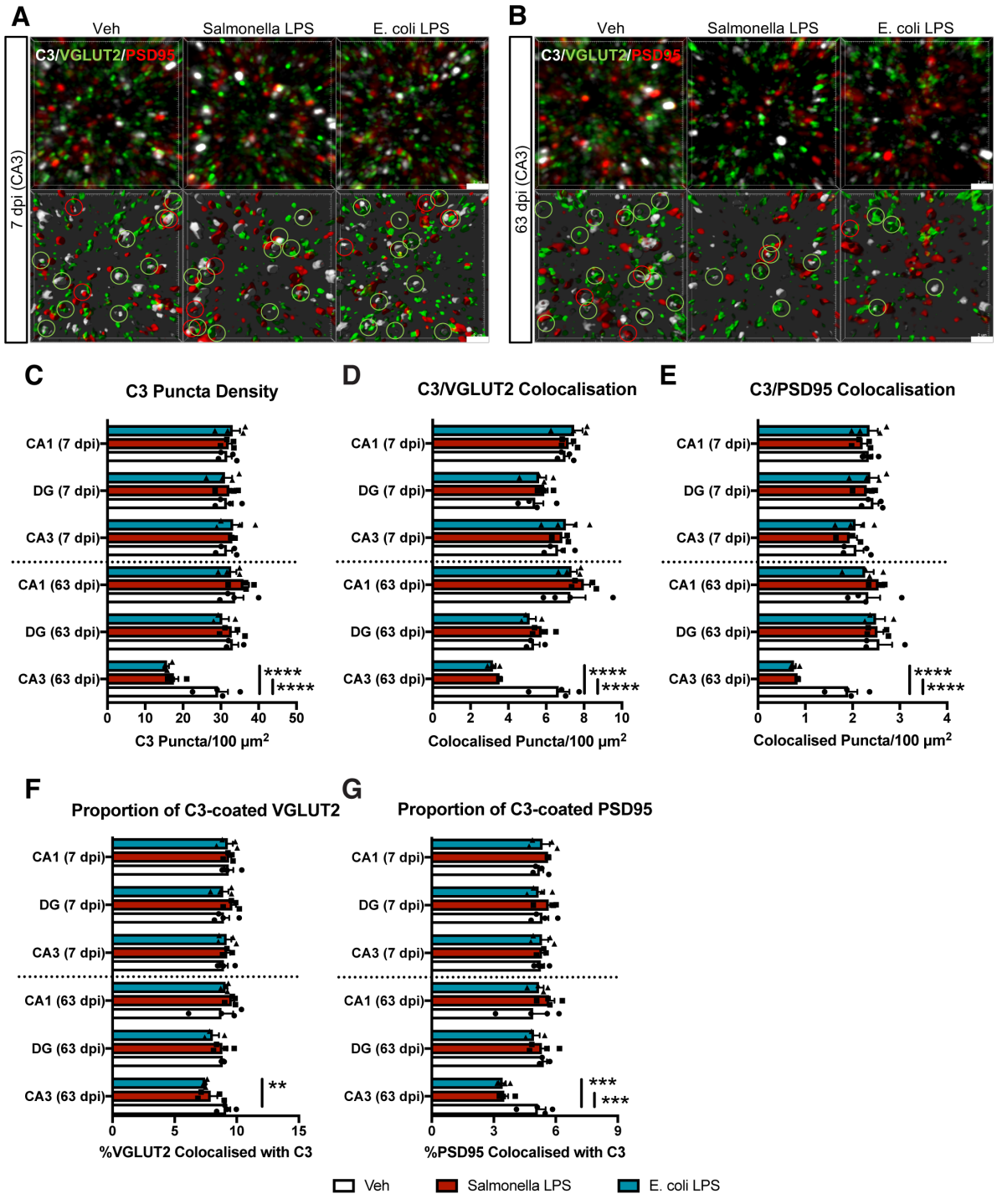

Figure 13. Reduced synaptic C3 puncta density in CA3 at 63 dpi.

(See figure legend on next page.)

(A, B) Representative super-resolution images of complement factor C3 (white), together with VGLUT2 (green) and PSD95 (red) in CA3 at (A) 7 dpi and (B) 63 dpi. The three-dimensional reconstruction of two adjacent z-planes demonstrated colocalisation of C3 puncta with either VGLUT2 (green circles) or PSD95 (red circles). Scale bar = 2 μm.

(C-E) Decrease of (C) total C3 puncta and (D, E) synaptic C3 puncta colocalised with VGLUT2 or PSD95 in CA3 at 63 dpi (n=3-4 mice).

(F, G) Reduction of the C3-coated excitatory synaptic puncta out of the total synaptic puncta in CA3 at 63 dpi (n=3-4 mice).

All the statistical analyses presented in panels **C-G** were based on a two-way ANOVA with a Tukey *post-hoc* test (***p* < 0.01, ****p* < 0.001, *****p* < 0.0001). Data were expressed as mean ± SEM.

Abbreviations: dpi, days post-final injection; DG, dentate gyrus; LPS, lipopolysaccharide; PSD95, postsynaptic protein density 95; VGLUT2, vesicular glutamate transporter 2.

Chapter 4: Neuron Density and Senescence after Prolonged Inflammation

4.1 Effects of 4xLPS and 7xLPS injections on neurons in the hippocampus

Previous reports about neuronal loss following LPS injection used either higher concentrations of LPS (e.g. 5 or 10 mg/kg) (Semmler *et al.* 2007; Qin *et al.* 2007) or prolonged exposures to lower doses of LPS (e.g. injections on four or seven consecutive days) (Lee *et al.* 2008; Bodea *et al.* 2014). Thus, we postulated that the negative results observed at 7 dpi of 2xLPS might be due to insufficient dosing of LPS. To test this hypothesis, we injected *Salmonella* LPS on four and seven consecutive days and quantified the neuronal cell density in the CA1 region of the hippocampus at 7 dpi. Nevertheless, this analysis demonstrated the neuron density remained normal after 4xLPS and 7xLPS injections (**Fig. 14**). This indicated that the neuronal cell death might not be acutely induced in CA1 by these injection paradigms at 7 dpi.

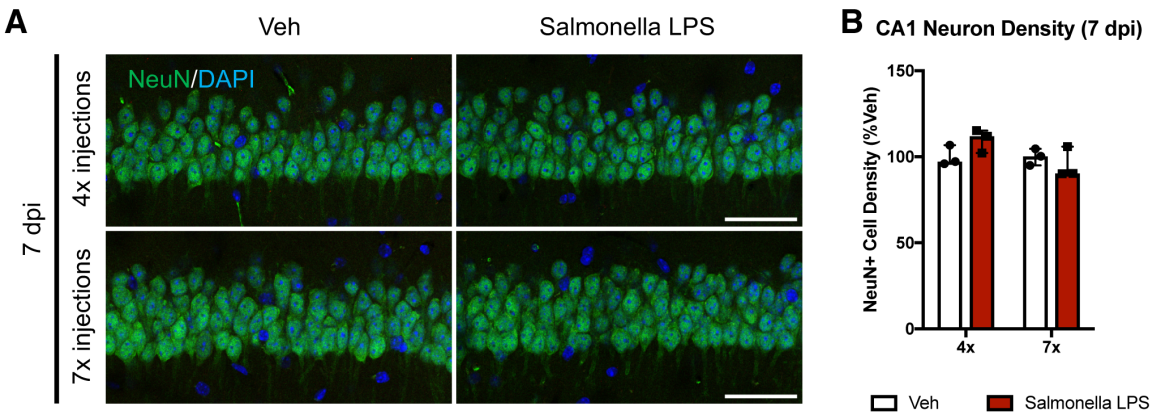

Figure 14. Normal neuron density in CA1 at 7 dpi of 4xLPS and 7xLPS.

(A) Representative figure of NeuN staining (green) in CA1 subfield of the hippocampus at 7 dpi of 4xLPS and 7xLPS. Scale bar = 50 μm.

(B) Normal neuron density in CA1 at 7 dpi of 4xLPS and 7xLPS (n=3 mice, Kruskal-Wallis test with a *post-hoc* Dunn's test). Data were expressed as median ± 95% confidence intervals.

Abbreviations: dpi, days post-final injection; LPS, lipopolysaccharide.

4.2 Microglial and astrocytic senescence

4.2.1 Age-dependent, but treatment-independent, microglial senescence at 63 dpi

Previous studies reported that the NLRP3 inflammasome is required for low-grade inflammation in the hippocampus during ageing (Youm *et al.* 2013) and implicated in glial senescence (Heneka *et al.* 2018). Because its activation in the brain is peaked at 3 dpi of LPS injection (Tejera *et al.* 2019), and our immunoblot analysis provided some evidence that the NLRP3 inflammasome might have been activated before 7 dpi (**Fig. 6B, E-G**), we sought to address whether the LPS injection might induce the glial senescence. To this end, a decline of nuclear lamin B1 immunoreactivity, a hallmark of cellular senescence (Freund *et al.* 2012), was tested in microglia at 7 dpi and 63 dpi (**Fig. 15A, B**). Quantification of CTCF showed that there was no effect of the LPS injection on the lamin B1 signal intensity at 7 dpi and 63 dpi (**Fig. 15A, B**). However, this analysis indicated an overall age-dependent reduction of lamin B1 signals from 7 dpi to 63 dpi (7 dpi — *Salmonella* LPS: 1968.47 ± 147.44 arbitrary unit (AU), Veh: 1798.28 ± 75.59 AU; 63 dpi: *Salmonella* LPS: 1296.14 ± 95.02 AU, Veh: 1422.65 ± 231.82 AU; pooled analysis of 7 dpi vs. 63 dpi: $p = 0.005$, two-way ANOVA, **Fig. 15B**), indicating the progressive induction of the microglial senescence from 14 to 16 months of age. Given that lamin B1 is a nuclear envelop protein regulating the nuclear architecture of cells (Freund *et al.* 2012), the size of microglial nuclei and circularity were measured. Consistent with the age-dependent, treatment-independent, changes in the lamin B1 immunoreactivity, the microglial nuclei were enlarged in an age-dependent manner (7 dpi — *Salmonella* LPS: 39.20 ± 1.45 μm^2, Veh: 38.06 ± 1.48 μm^2; 63 dpi — *Salmonella* LPS: 45.99 ± 2.99 μm^2, Veh: 47.78 ± 2.74 μm^2; pooled analysis of 7 dpi vs. 63 dpi: $p = 0.005$, two-way ANOVA, **Fig. 15C**). Likewise, the mean circularity was declined in the vehicle group from 7 dpi to 63 dpi (7 dpi: 0.75 ± 0.003 AU, 63 dpi: 0.70 ± 0.01 AU; $p = 0.041$, two-way ANOVA, **Fig. 15D**). Furthermore, there was a treatment effect of LPS on mean circularity at 7 dpi (*Salmonella* LPS: 0.69 ± 0.02 AU, Veh: 0.75 ± 0.003 AU; $p = 0.002$, two-way ANOVA, **Fig. 15E**). Because there found no changes in lamin B1 immunoreactivity and nuclear size due to the LPS injection, this reduction of mean circularity may not be attributed to the induction of senescence. An alternative explanation might be the prior induction of proliferation and migration to the blood vessels following LPS injections.

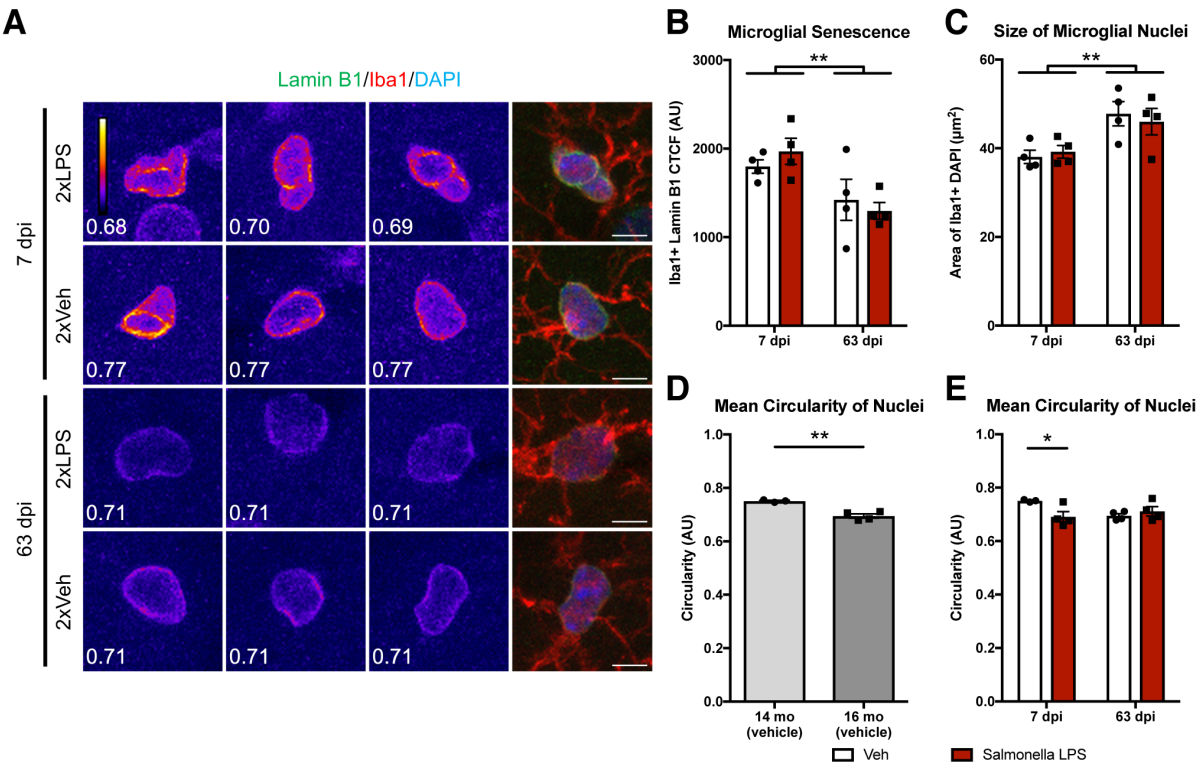

Figure 15. Little 2xLPS effects on microglial senescence at 7 dpi and 63 dpi.

(A) Representative maximum intensity projection images of lamin B1 signals colocalised with Iba1-positive microglia in CA1 at 7 dpi and 63 dpi of *Salmonella* LPS on two consecutive days (2xLPS). Signals in red indicated the higher fluorescent intensity of lamin B1, while those in blue lower intensity. A value in the bottom left corner of each image was the circularity of the microglial nucleus. Scale bar = 5 µm.

(B) CTCF of microglial lamin B1 in CA1 at 7 dpi and 63 dpi. Age-dependent reduction of lamin B1 immunoreactivity was observed, but these changes were not dependent on LPS injection (n=4 mice/treatment).

(C) Area of microglial nuclei in CA1 at 7 dpi and 63 dpi. Age-dependent increase in nuclear size in microglia was found from 7 dpi to 63 dpi (n=4 mice).

(D) Mean circularity of microglial nuclei in CA1 in vehicle-injected mice at 7 dpi (mean age of 14.8 mo) and 63 dpi (mean age of 16.6 mo). Age-related reduction was observed at 16 months of age (n=3-4 mice, Student's *t*-test, $^{**}p < 0.01$).

(E) Mean circularity of microglial nuclei in CA1 at 7 dpi and 63 dpi. A reduction was observed at 7 dpi of LPS (n=3-4 mice).

Statistical analysis presented in panels **B, C** and **E** used a two-way ANOVA with a Sidak *post-hoc* test ($^{*}p < 0.05$, $^{**}p < 0.01$). Data were mean ± SEM.

Abbreviations: AU, arbitrary unit; CTCF, corrected total cell fluorescence; dpi, days post-final injection; LPS, lipopolysaccharide.

4.2.2 No effects on glial senescence at 7 dpi of 4xLPS and 7xLPS

In order to investigate whether the glial senescence might occur in astrocytes and whether the endotoxin challenges for longer periods than two consecutive days may be required for inducing glial senescence, an observational study was performed at 7 dpi of 4xLPS and 7xLPS. As a result, lamin B1 immunoreactivity appeared to be unchanged both in microglia (**Fig. 16A**) and astrocytes (**Fig. 16B**) after the 4xLPS and 7xLPS injections. This indicated that microglial and astrocytic senescence was not induced by LPS injections at 7 dpi in old mice.

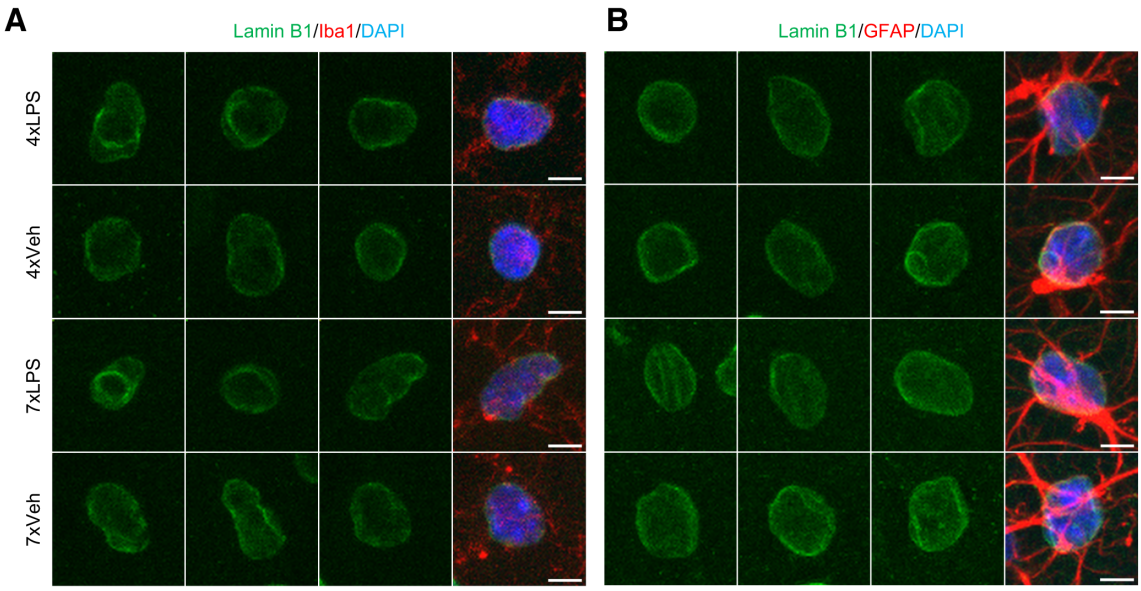

Figure 16. Little effects of 4xLPS and 7xLPS on glial senescence at 7 dpi.
(A, B) No apparent changes in lamin B1 (green) immunoreactivity in microglia (A) and astrocytes (B) at 7 dpi of 4xLPS and 7xLPS. Scale bar = 5 μm.
Abbreviations: dpi, days post-final injection; GFAP, glial fibrillary acidic protein; LPS, lipopolysaccharide.

Chapter 5: Roles of TREM2 in Synapse Loss of Aged APP/PS1 Mice

5.1 A brief introduction of this chapter

In animal models of amyloid pathology, including the one used in the present study (that is, APP/PS1 mice), synapse loss is detected as early as at 4 months of age (Hong *et al.* 2016). Some studies showed that synapse loss is spatially correlated with the distance from the plaque centre, suggesting the synaptotoxic nature of the oligomeric Aβ (Sauerbeck *et al.* 2020; Koffie *et al.* 2009). Other studies demonstrated this synapse loss may be mediated by microglia because pharmacological depletion of microglia or normalisation of microglial density (using colony stimulating factor 1 receptor (CSF1R) inhibitors) prevented synapse loss in *APP* transgenic mice (Olmos-Alonso *et al.* 2016; Spangenberg *et al.* 2016). Microglial synaptic pruning was also implicated via the complement activation (Hong *et al.* 2016).

Previously, several loss-of-function mutations of *TREM2* have been linked to patients with neurodegenerative diseases, such as the R47H mutation for sporadic AD (Guerreiro *et al.* 2013b; Jonsson *et al.* 2013) and the T66M mutation for FTD-like syndromes (Guerreiro *et al.* 2013a). TREM2 seems to modify the amyloid pathology because compartmentalisation of Aβ plaques was impaired by TREM2-deficient microglia in animal models of AD (Yuan *et al.* 2016). Recently, TREM2 has also been required for microglial synaptic pruning *in vitro* and in the presence of amyloid pathology (Scott-Hewitt *et al.* 2020; Filipello *et al.* 2018) (**Fig. 3A**).

On this basis, we hypothesised that microglia in APP/PS1 mice with the loss-of-function T66M mutation of the *Trem2* gene might impair their capacity of synaptic pruning. To this end, we analysed the plaque and oligomer density in the hippocampus and cortex, followed by the synaptic puncta density in the same regions.

5.2 Altered Aβ plaque and oligomer loads with the *Trem2* mutation

Analysis of methoxy X04-positive Aβ plaque load revealed that the plaque density was reduced in the cortex of 12-month-old APP/PS1 mice with the *Trem2* mutation, compared with the age-matched APP/PS1 mice (APP/PS1; *Trem2*^{T66M}: 931.90 ±

196.32 plaques/mm^2, APP/PS1: 4446.13 ± 1074.03 plaques/mm^2; p = 0.004, two-way ANOVA, **Fig. 17A, C**). Similarly, the coverage was also found to be reduced in the cortex in the *Trem2* mutant mice (APP/PS1; *Trem2*^{T66M}: 0.83 ± 0.06%, APP/PS1: 2.70 ± 0.51%; p = 0.007, two-way ANOVA, **Fig. 17A, D**).

An abundance of fibrillar oligomeric Aβ species was quantified on brain sections stained for a conformation-specific antibody OC. Results indicated that the cortex of *Trem2* mutant possessed higher density of Aβ oligomers (APP/PS1; *Trem2*^{T66M}: 723.18 ± 37.60 plaques/mm^2, APP/PS1: 583.92 ± 64.08 plaques/mm^2; p = 0.044, two-way ANOVA, **Fig. 17B, E**). Consistently, the coverage also increased in the cortex of *Trem2* mutant (APP/PS1; *Trem2*^{T66M}: 8.54 ± 0.62%, APP/PS1: 5.73 ± 0.78%; p = 0.005, two-way ANOVA, **Fig. 17B, F**). We also tried to quantify prefibrillar Aβ oligomers in the brain using an A11 antibody. However, numerous A11-positive puncta were observed in both an APP/PS1 and its wild-type littermate (data not shown), and thus this analysis was not performed. This positive staining in the wild-type brain is likely due to the staining of homooligomers that many proteins can form (Hashimoto and Panchenko 2010). Together with the previous study showing fewer microglia around the plaques, these results indicated that loss of functional TREM2 proteins in microglia failed to compartmentalise Aβ into plaques, resulting in the spreading of the Aβ oligomers in the cortex.

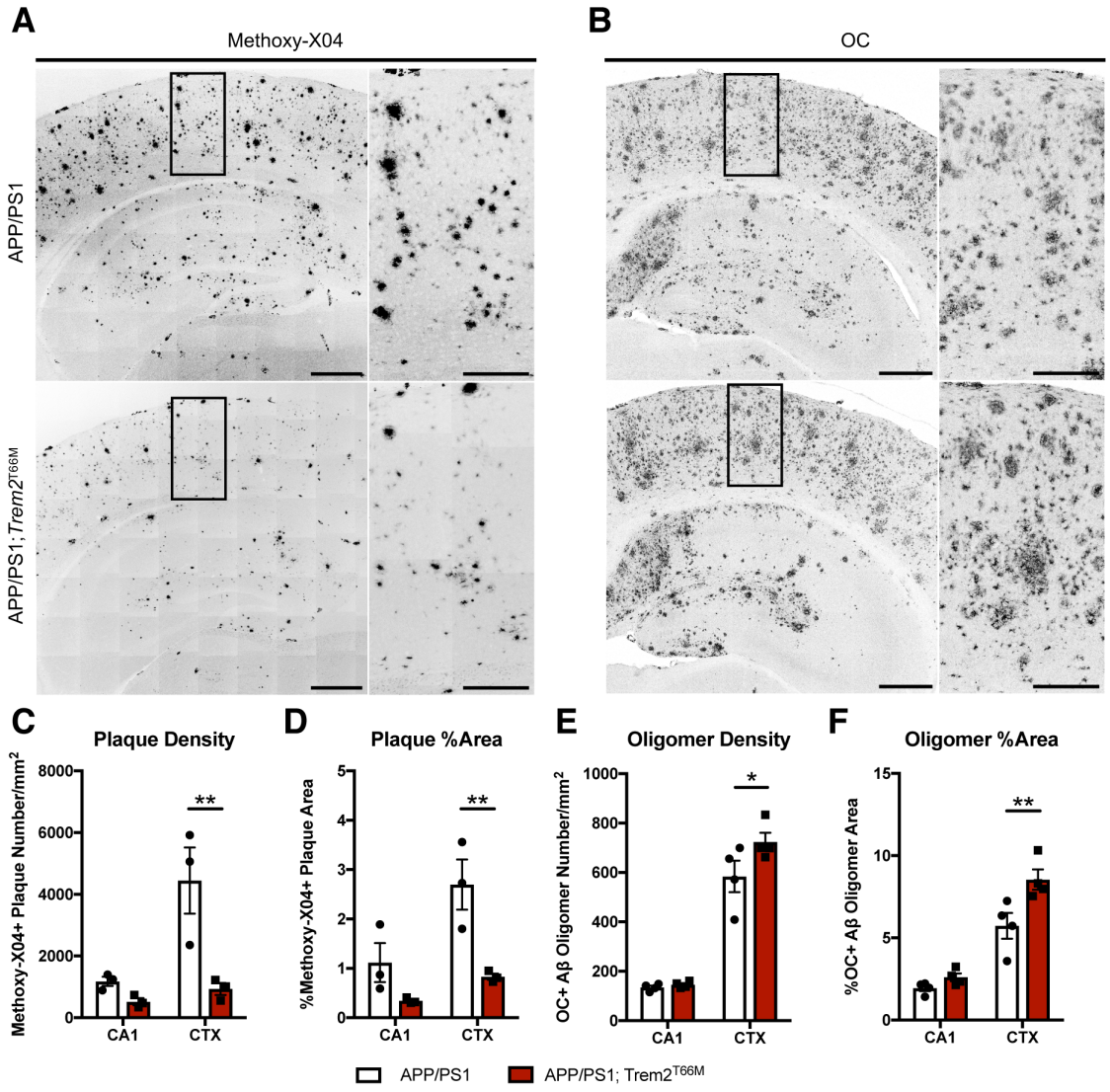

Figure 17. Altered amyloid pathology in the presence of *Trem2* mutation.

(A, B) Representative figures showing the distinct abundance of (A) methoxy-X04-positive Aβ plaque and (B) OC-positive Aβ oligomers in 12-month-old APP/PS1 and APP/PS1; *Trem2*^{T66M} mice. Scale bar = 500 μm. Images on the right half in panels (A) and (B) were the magnified part of the cortex (rectangles). Scale bar = 200 μm.

(C, D) Aβ plaque density and area in the CA1 hippocampal region and the parietal cortex (CTX). The plaque density and area were reduced in the cortex of APP/PS1; *Trem2*^{T66M} mice compared with APP/PS1 mice (n=3 mice).

(E, F) Oligomer density and area in CA1 and CTX. A higher oligomer density and area were found in the cortex of APP/PS1; *Trem2*^{T66M} mice than APP/PS1 mice (n=4 mice).

All the statistical analysis presented in panels **C-F** used a two-way ANOVA with a Sidak *post-hoc* test (*p < 0.05, **p < 0.01). Data were mean ± SEM.

5.3 Quantification of synaptic puncta in relation to the Aβ plaques

In order to test whether the diffused area of Aβ oligomers may worsen the synapse loss in APP/PS1 mice, or whether a lack of functional TREM2 proteins may mitigate the synapse loss due to the impaired synaptic pruning, synaptic puncta density was compared in the proximal region from the Aβ plaques with that in the distal region. Because the difference of oligomer density and coverage between *Trem2* wild-type and mutant mice were more evident in the cortex, quantification of synaptic puncta focused on the parietal cortex. Circles were drawn at the increasing radius from 2.5 μm to 80 μm around 8-9 plaques in the cortex (**Fig. 18A**). Overall, both genotypes demonstrated that synapse loss was the highest in the plaque proximal regions (0-2.5 μm from the plaque centre). Using the synaptic puncta density in the plaque distal regions (40-80 μm from the plaque centre) of the same plaque as internal controls, colocalised synaptic puncta density in each plaque decreased by 82.27 ± 1.42% (VGLUT2: 56.27 ± 6.82%, PSD95: 67.03 ± 4.39%) in APP/PS1 mice and 60.08 ± 10.58% (VGLUT2: 49.45 ± 10.58%, PSD95: 49.58 ± 9.89%) in APP/PS1; *Trem2*^{T66M} mice (**Fig. 18B-E**). Both genotypes showed a clear normalising tendency away from the plaque centre, reaching the normal levels at 20-40 μm from the plaque centre (**Fig. 18B-E**). When the synaptic puncta density was compared with the internal controls (that is, puncta density in the most distal area of interest at 40-80 μm from the same plaque centre), there found no difference between the genotypes (**Fig. 18B-E**). However, when the absolute synaptic puncta density was compared between the genotypes, both proximal (0-5 μm area) and distal regions (20-40 μm area) detected a higher synaptic puncta density in APP/PS1; *Trem2*^{T66M} mice than APP/PS1 mice in the proximal regions (median [IQR]: VGLUT2 — APP/PS1: 10.00 [6.43, 21.45] puncta/100 μm^2, APP/PS1; *Trem2*^{T66M}: 23.45 [12.10, 40.83] puncta/100 μm^2, p = 0.003; PSD95 — APP/PS1: 6.90 [2.10, 9.90] puncta/100 μm^2, APP/PS1; *Trem2*^{T66M}: 12.90 [6.08, 19.63] puncta/100 μm^2, p = 0.005; VGLUT2/PSD95 colocalisation — APP/PS1: 0.00 [0.00, 0.40] puncta/100 μm^2, APP/PS1; *Trem2*^{T66M}: 0.70 [0.00, 2.03] puncta/100 μm^2, p = 0.011, Mann-Whitney test, **Fig. 18F-H**) and the distal regions (median [IQR]: VGLUT2 — APP/PS1: 20.00 [15.18, 45.60] puncta/100 μm^2, APP/PS1; *Trem2*^{T66M}: 37.25 [25.95, 58.93] puncta/100 μm^2, p = 0.0005; PSD95 — APP/PS1: 12.75 [9.55, 19.75] puncta/100 μm^2, APP/PS1; *Trem2*^{T66M}: 18.00 [12.88, 26.10] puncta/100 μm^2, p = 0.034; VGLUT2/PSD95 colocalisation — APP/PS1: 0.55 [0.30, 1.53] puncta/100 μm^2, APP/PS1; *Trem2*^{T66M}: 1.50 [0.63, 2.50] puncta/100 μm^2, p =

0.011, Mann-Whitney test, **Fig. 18F-H**). Taken together, these results suggested that *Trem2* mutation ameliorated the synapse loss in APP/PS1 mice even in the presence of more abundant Aβ oligomers in the cortex. Given that the *Trem2* mutation did not have an effect on the relative abundance of synaptic puncta to the internal controls, these data implied that other mechanisms were involved in the synapse loss in the proximal to the Aβ plaques.

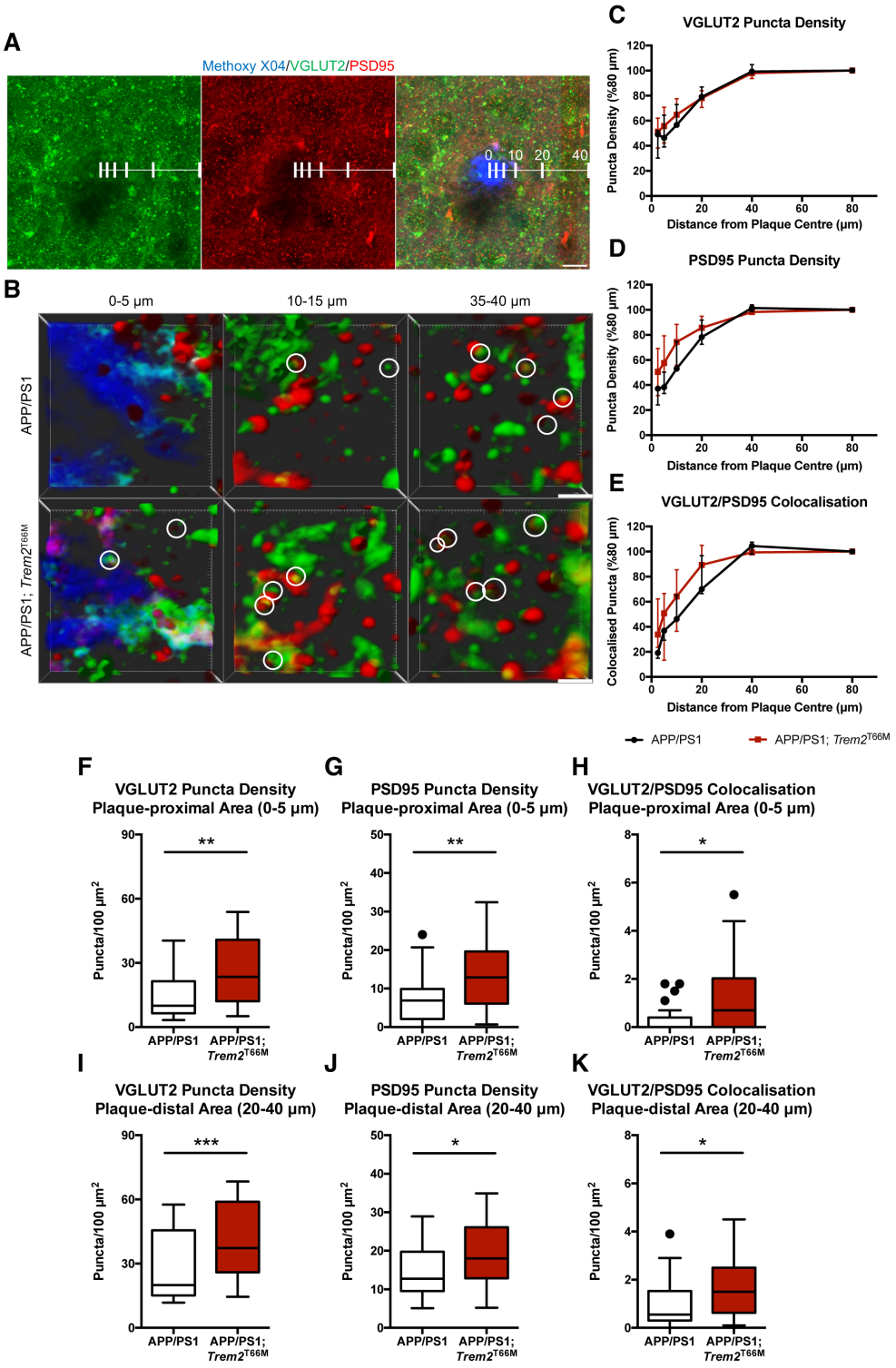

(See figure on previous page.)

Figure 18. Effects of the *Trem2* mutation on synapse loss in APP/PS1 mice.

(A) Maximum intensity projection of super-resolution images of VGLUT2 (green), PSD95 (red) and methoxy-X04 (blue) staining. A clear loss of synaptic puncta staining was observed in the vicinity of Aβ plaques in the cortex of a 12-month-old APP/PS1 mouse. White lines indicate the distance from the plaque centre in μm, and the synaptic puncta density was quantified by drawing circles at the radius of 2.5, 5, 10, 20, 40 and 80 μm around the 8-9 plaques per animal. Scale bar = 10 μm.

(B) Three-dimensional reconstructions of VGLUT2 (green), PSD95 puncta (red) and their colocalisation (white circles) in 0-5 μm, 10-15 μm and 35-40 μm from the plaque centre. Methoxy-X04-positive plaques were confirmed in the 0-5 μm areas. A robust synapse loss was found nearby the plaques, but the normalisation of synapses was conceivable away from the plaque centre both in APP/PS1 and APP/PS1; *Trem2*^{T66M} mice. Scale bar = 1 μm.

(C-E) Quantification of (C) VGLUT2, (D) PSD95 and (E) colocalised VGLUT2/PSD95 puncta in the cortex of APP/PS1 and APP/PS1; *Trem2*^{T66M} mice. Raw data were normalised by the synaptic puncta density at the distance of 40-80 μm area (n=3-4 mice, Kruskal-Wallis test with a Dunn's *post-hoc* test).

(F-K) Synaptic puncta density in the (F-H) plaque-proximal (0-5 μm from the plaque centre) and (I-K) plaque-distal regions (20-40 μm) in APP/PS1 and APP/PS1; *Trem2*^{T66M} mice. Density of (F, I) VGLUT2, (G, J) PSD95 and (H, K) colocalised VGLUT2/PSD95 puncta indicated the higher synaptic puncta density in the presence of the *Trem2* mutation (n=26-28 plaques from 3-4 mice/genotype, two-tailed Mann-Whitney test, $*p < 0.05$, $**p < 0.01$, $***p < 0.001$).

In panels **C-K**, data were presented as median ± interquartile range.

Abbreviations: PSD95, postsynaptic protein density 95; VGLUT2, vesicular glutamate transporter 2.

Chapter 6: Discussion

6.1 Findings from the endotoxin project

6.1.1 Induction and persistence of neuroinflammation for more than a week

The present study confirmed that peripheral injections of *Salmonella* LPS and *E. coli* LPS into aged mice resulted in neuroinflammation lasting for at least seven days, but almost fully resolved by two months post-injection. It is intriguing to note that CXCL1 and IL-6 levels seemed to maintain at the higher levels after *E. coli* LPS injections, indicating that this LPS serotype may be able to produce longer neuroinflammatory responses than *Salmonella* LPS. This trend was also seen in several other data (for example, ASC protein levels, microglial morphology and mean lysosome volume in microglia). Many of our data about neuroinflammatory responses are consistent with the Tejera *et al*.'s (2019) study which examined the acute effects of *Salmonella* LPS injection (at 1 mg/kg via i.p. route) into 15-month-old mice. For instance, the authors found that changes in microglial morphology and cytokine levels were normalised by 10 dpi (Tejera *et al.* 2019). Microglial proliferation and CD68 immunoreactivity increased at 2 dpi, but returned to the normal levels at 10 dpi (Tejera *et al.* 2019), supporting our data of microglial density and total lysosome volume at 7 dpi. Similarly, the investigators found the increased ASC speck formation using histology at 2 dpi and 10 dpi (Tejera *et al.* 2019), which was again confirmed by our immunoblot analysis at 7 dpi.

6.1.2 Local and delayed loss of the CA3 excitatory synapses and complements

Our histological data suggested that systemic inflammation can lead to a local, delayed synapse loss in CA3 at 63 dpi with preserving the global synaptic protein levels in the brain at 7 dpi and 63 dpi. We presented that this synapse loss was specific to the excitatory synapses in CA3 because the inhibitory synaptic proteins remained unchanged. This indicated that systemic inflammation may produce a chronic imbalance between excitatory and inhibitory synaptic transmissions at CA3 and then affect the neuronal activity in CA1 via Schaffer collaterals. In order to test whether the CA3 excitatory synapse loss is associated with long-term disturbances of cognitive functions, behavioural experiments will be needed at two or more months after the endotoxin injection. Plus, biochemical analysis of synaptic proteins in the

hippocampus and electrophysiological recordings of LTP will provide further evidence for the synapse loss and impaired synaptic transmission within the hippocampus.

It is worth noting that the *E. coli* LPS group showed elevated levels of IL-6 at 7 dpi and 63 dpi. Since we did not observe a similar increase in the *Salmonella* LPS group, this may highlight another serotype-related difference in neuroinflammatory responses. As mentioned earlier, many groups reported a correlation between higher IL-6 levels in the plasma and delirium (van Munster *et al.* 2008; Wu *et al.* 2020; de Rooij *et al.* 2007; Singh-Manoux *et al.* 2014). Admittedly, our analysis of synaptic puncta density did not uncover serotype-related differences, but persistently high IL-6 levels in the brain may imply that the *E. coli* LPS-treated group display poorer performance of behavioural experiments than *Salmonella* LPS. If a similar rise is also detected in the serum at 63 dpi, the *E. coli* LPS injection into old mice may serve as a better model for the inflammatory responses elicited by the bacterial infection than *Salmonella* LPS.

Recently, Beyer *et al.* (2020) injected either *Salmonella* or *E. coli* LPS into 16-month-old mice and found a distinct microglial morphology and a reduced dendritic spine density in CA1 at three months post-injection of LPS. Importantly, both of the bacterial serotypes of LPS equally affected the pyramidal cell morphology and the spine density in the apical dendrites of CA1, but not in the basal dendrites (Beyer *et al.* 2020). These results in the apical dendrites of CA1 were not consistent with our data demonstrating the normal microglial morphology and synaptic puncta density in CA1 stratum radiatum at two months post-injection. However, this discrepancy can be explained by the timing of analysis after the endotoxin challenge, meaning that one more month may have been required for detecting the synapse loss in CA1 in this study. Because our data suggested the increased inhibitory tone of the Schaffer collaterals, the neuronal activity should be declined over time, and this likely affects the microglia-synapse interactions. Notably, abrogation of neuronal activity via light deprivation induced the morphological alterations of microglia (consistent with Beyer *et al*.'s study (2020)) and decreased the contact frequency with dendritic spines in the visual cortex as a result of a lowered motility of microglial processes (consistent with the reduced synaptic pruning by CA1 microglia in this study) (Tremblay *et al.* 2010). Further, this light deprivation reduced the size of dendritic spines, with which microglia did not contact during the *in vivo* imaging periods (Tremblay *et al.* 2010). It is reasonable to

speculate that this change in the spine size affects the manual counting of dendritic spines in the fixed tissues as performed in Beyer *et al*.'s study (2020). Since microglia can also contribute to synaptogenesis (Miyamoto *et al.* 2016; Weinhard *et al.* 2018), systemic inflammation may reduce the microglia-synapse interactions with a consequence of declining the synaptogenesis in CA1 apical dendrites.

Other as yet answered questions from our study are why the CA3 excitatory synapses were only targeted by the systemic inflammation and what molecular mechanisms resulted in the delayed synapse loss between 7 dpi and 63 dpi. We initially hypothesised that because the complement system can be acutely activated by the endotoxin challenge (Jacob *et al.* 2007; Bodea *et al.* 2014), synaptic pruning by microglia may be enhanced as observed during development and in the presence of amyloid pathology (Hong *et al.* 2016; Schafer *et al.* 2012). However, we found neither the accumulation of C3 proteins nor an expected increase in the synaptic pruning by microglia in CA3 at 7 dpi and 63 dpi. Our histological data about the normal C3 puncta density can be explained by the rapid normalisation of C3 levels by 7 dpi. In support, previous studies reported elevated C3 levels at earlier timepoints (Jacob *et al.* 2007; Bodea *et al.* 2014). Given that the number of both synaptic C3 and C3-coated excitatory synapses were simultaneously lowered in CA3 at 63 dpi, one can argue that synaptic pruning by CA3 microglia may be increased between the two points in time that we analysed.

From the data presented in this thesis, our results ruled out two possible explanations for this CA3-specific synapse loss. First, our analysis of microglial density did not reveal clear regional differences in CA1 and CA3 at 7 dpi and 63 dpi, indicating that the net synaptic pruning did not account for the CA3-specific synapse loss. With higher sample sizes than the present study, previous studies found that microglial density was even higher in CA1 than in CA3 (Filipello *et al.* 2018; Jinno *et al.* 2007). Thus, it seems unlikely that increasing the sample sizes and number of fields to count microglia in our study can help to provide explanations based on the total synaptic puncta inside the entire microglial populations in CA1 and CA3. Second, although the LPS-induced morphological differences were more significant in CA1 than in CA3, the morphology in LPS-injected animals were found to be indistinguishable. This means that whereas the baseline microglial morphology may be more ramified in CA1 than in

CA3, the levels of LPS-induced microglial activation may be similar in these hippocampal subfields.

An alternative hypothesis to account for the CA3 synapse loss may be related to the effects of LPS injections on the peripheral organs such as the kidney (**Table 2**). As detailed later, the renal dysfunctions are closely associated with the cognitive disturbances (as observed in patients with chronic kidney disease (CKD)) (Viggiano *et al.* 2020) and the persistence of peripheral inflammation in patients who survived sepsis (Hawkins *et al.* 2018). Thus, uraemic toxins that the damaged kidneys fail to eliminate may accumulate over time and eventually induce the PS exposure at synapses, promoting synaptic pruning by microglia after a delay of more than a week after the endotoxin challenge. This raises a need for further studies to investigate whether the renal functions may be chronically impaired in the old animals and whether synaptic pruning may be enhanced at an intermediate timepoint such as 30 dpi. Moreover, C5a anaphylatoxin receptor (C5aR) has been previously found at synapses in the mossy fibres of rats (Crane *et al.* 2009) and is activated downstream of the C3-dependent complement pathway (Veerhuis *et al.* 2011). Although little is known about whether C5aR is more abundant in excitatory synapses than in inhibitory synapses, such potential differences in accumulations at different types of synapses may help to explain the propensity for excitatory synapse loss. It should be noted that previous studies highlighting the roles of C3 in synaptic pruning did not examine its downstream pathway, including the C5a-C5aR axis (Schafer *et al.* 2012; Hong *et al.* 2016). Hence, it remains possible that activation of this downstream signalling can promote synaptic pruning by microglia selectively in the area CA3.

6.1.3 No effects of 2x, 4x, 7xLPS on glial senescence

On the contrary to the NLRP3 inflammasome activation in the brain, our histological analysis of microglial senescence produced negative results. Endotoxin injections on four and seven consecutive days did not induce the microglial and astrocytic senescence in CA1 at 7 dpi. Nevertheless, independent of the LPS injections, we observed a reduction of lamin B1 signals in microglia at 16 months of age compared with that at 14 months of age, indicating the gradual onset of microglial senescence between these ages. Although the difference of lamin B1 immunoreactivity is clear in

this study, it is noteworthy that downregulation of lamin B1 is not sufficient to conclude that microglia in 16-month-old mice are senescent because there exists no single specific marker for cellular senescence (Gorgoulis *et al.* 2019). Thus, it is important to examine other markers of senescence to confirm this result in the future (for example, p16, p21 and senescence-associated β-galactosidase activity (Baker and Petersen 2018)).

Given that NLRP3-dependent senescence in the CNS was suggested in mice at an advanced age (23 months old) (Youm *et al.* 2013), the endotoxin challenge may be too early to induce the microglial senescence. Alternatively, both amyloid and tau pathologies can chronically activate the NLRP3 inflammasome pathway (Heneka *et al.* 2013; Ising *et al.* 2019), and cellular senescence has been recently reported in microglia around Aβ plaques in 12-month-old APP/PS1 mice (Hu *et al.* 2021) and neurons bearing neurofibrillary tangles (NFTs) in >16-month-old human *APP* and *MAPT* (microtubule-associated protein tau) transgenic mice (Musi *et al.* 2018). On this ground, the NLRP3 inflammasome activation by the LPS injection might be too short.

6.1.4 Limitations of the present study as animal models of sepsis

The LPS injection paradigm (2xLPS) in this study was intended to maximise the inflammatory responses to prevent immune tolerance in the brain (Wendeln *et al.* 2018). However, in patients who survived sepsis, sustained immunosuppression is a common observation especially after the hospital discharge (Stortz *et al.* 2018; Gentile *et al.* 2012) (**Fig. 1A**). Similar immunosuppression in the CNS remains to be determined, but our injection paradigm in this sense may be less relevant for the observation in patients with sepsis. Furthermore, LPS injections on four or more consecutive days, rather than a single injection, produced more pronounced cerebral damages (for example, neuron density in the substantia nigra (Bodea *et al.* 2014) and the BBB permeability changes (Haruwaka *et al.* 2019)), thereby requiring further considerations of the choice of injection paradigm in the future. To regard our endotoxin challenge as animal models of sepsis, analysis of peripheral organ damages should have been investigated. The present study could also be improved by using other animal models of sepsis (such as caecal ligation and puncture (CLP) and gram-positive bacterial infection) to confirm the reproducibility of our findings.

6.2 Findings from the TREM2 project

6.2.1 Reduced plaque load and elevated oligomer load in Trem2 mutants

Our data demonstrated that a loss-of-function mutation of the *Trem2* gene lowers the Aβ plaque load but increases the fibrillar oligomer load in the cortex of 12-month-old APP/PS1 mice. Although these results need to be re-evaluated using APP/PS1 mice with a more relevant *Trem2* mutation for AD (namely, the R47H and R62H mutations) (Guerreiro *et al.* 2013b; Jonsson *et al.* 2013; Jin *et al.* 2014; Sims *et al.* 2017), our data confirm recent studies of TREM2-deficient *APP* transgenic mice showing that the plaque load was reduced as the animals got older (Parhizkar et al. 2019; Meilandt et al. 2020), but the soluble OC-positive Aβ oligomers increased in the hippocampus (Meilandt et al. 2020). However, these investigators also found that the amyloid pathology was increased in female mice at a younger age (6-7 months old), and the reduced plaque load in male mice was only detectable at an advanced age (19-22 months old) (Meilandt et al. 2020). This indicated that the genotype effect of *Trem2* knockout on the plaque load may be dependent on sex and show a fluctuating course of changes during ageing. Indeed, using different *APP* transgenic mouse models, some investigators showed that the plaque density remained normal at 4 months of age but increased at 8 months (Wang et al. 2015; Wang et al. 2016), while others claimed normal or lower levels at 4 months, followed by the higher plaque density at 8 months (Jay et al. 2017; Jay et al. 2015). Importantly, on a *post-mortem* investigation of the R47H mutation heterozygous careers who developed AD, the amyloid pathology remained unchanged (Yuan *et al.* 2016). One possible explanation of these inconsistent results is the artefacts caused by the overexpression of different transgenes in these *APP* transgenic mouse lines. Thus, the use of *App* knock-in mouse models, which overcome this problem by expressing humanised *App* mutations under the mouse endogenous promoter (Saito et al. 2014; Xia et al. 2021), may yield more consistent data about the plaque load. In addition, the *Trem2* knockout mice or mice homozygous for the *Trem2* loss-of-function mutations may contribute to adding less relevant pathologies to animal models of AD. Homozygous loss-of-function mutations in genes to encode TREM2 or its adaptor protein, DNAX-activating protein of 12 kDa (DAP12), cause Nasu-Hakola disease in humans, characterised by dementia and frontal lobe syndrome at a very early age (<30 years old), basal ganglia calcification, bone cysts and fractures (Paloneva *et al.* 2002; Paloneva *et al.* 2001).

Individuals homozygous for the T66M mutation in the *TREM2* gene develop FTD-like syndromes (with atypical seizure) (Guerreiro *et al.* 2013a). Hence, whether the observed effects of TREM2 on amyloid pathology in mouse models truly recapitulates the pathology in patients with AD requires further investigations.

6.2.2 Increased synaptic puncta density in the cortex of Trem2 mutants

From the analysis of synaptic puncta density in this study, the most severe synapse loss was found in the immediate vicinity of Aβ plaques (0-5 μm from the plaque centre) and showed a progressive normalisation away from the plaque centre. This confirms previous studies showing the spatial correlation between synapse loss and distance from the plaques in *APP* transgenic mice (Sauerbeck *et al.* 2020; Koffie *et al.* 2009). Compared with synaptic puncta in the plaque distal regions (40-80 μm from the plaque centre), the synaptic puncta density in both genotypes returned to similar levels at 20-40 μm from the same plaque. However, our data suggested that the *Trem2* mutation partly rescued synapse loss in the cortex both in plaque distal and proximal regions. This suggested that despite the elevated levels of Aβ oligomers in the brain, lack of functional TREM2 proteins in microglia can lessen the synapse loss in APP/PS1 mice at 12 months of age. Given the importance of TREM2 in synaptic pruning (Filipello *et al.* 2018) and the contribution of microglia to the synapse loss in the presence of amyloid pathology even from the early disease stage (Hong *et al.* 2016), it seems likely that microglial synaptic pruning was impeded, thereby increasing the synaptic puncta density in the cortex of *Trem2* mutants. This is consistent with the rescue of synapse loss when microglia were almost completely depleted in *APP* transgenic mice using a potent CSF1R inhibitor (Spangenberg *et al.* 2016). Quantification of the synaptic pruning by microglia will be needed to elucidate the mechanism behind the increased synaptic puncta density in the future.

6.3 Other mechanisms behind the cerebral dysfunctions of sepsis

Our analysis focused on synaptic pruning by microglia in order to elucidate the synapse loss caused by systemic inflammation. However, other mechanisms (including the BBB breakdown, premorbid pathology associated with neurodegenerative diseases, renal failures and latent viral reactivation) should exist and are addressed here.

6.3.1 Cerebrovascular changes

As humans get older, cognitive functions deteriorate without the apparent hippocampal atrophy, and recent findings repeatedly suggested the roles of the increased BBB permeability in the hippocampus (Montagne *et al.* 2015; Nation *et al.* 2019; Montagne *et al.* 2020). Similarly, previous neuroimaging findings in patients with SAE suggested the presence of the BBB breakdown, such as white matter hyperintensity and vasogenic oedema (Stubbs *et al.* 2013; Ehler *et al.* 2017; Wardlaw *et al.* 2017). This is in line with the frequent observations of the increased BBB permeability in mouse models of sepsis and related systemic inflammation (such as endotoxin challenges (Varatharaj and Galea 2017), CLP (Flierl *et al.* 2009) and gram-positive bacterial infection (Andonegui *et al.* 2018)). One likely cellular mechanism that drives this change in the BBB permeability is the microglial uptake of tight junctions in the endothelium (**Fig. 19A**). The endothelial glycocalyx is a layer of glycoproteins and proteoglycans, lining the luminal side of the endothelium (van der Poll *et al.* 2017), and maintains the tight junction integrity (Hotchkiss *et al.* 2016). In patients with sepsis, the endothelial glycocalyx is ubiquitously degraded in various peripheral organs (such as kidney, lung and liver), coinciding with the increased endothelial permeability (Chelazzi *et al.* 2015). This shedding of glycocalyx is mediated by inflammatory mediators secreted by leukocytes which migrated and adhered to the endothelium (Chelazzi *et al.* 2015). Likewise, glycocalyx degradation products were also found in the hippocampus of young mice after endotoxin challenge at high doses and contributed to the LTP deficits and impaired fear memory (Hippensteel *et al.* 2019). The investigators claimed that heparan sulfate fragments (derived from the endothelial glycocalyx) bind to brain-derived neurotrophic factor (BDNF) at high affinity and inhibit the BDNF-TrkB receptor signalling in the hippocampus (Hippensteel *et al.* 2019). Consistently, a recent *in vivo* imaging study demonstrated that during the repeated LPS injections into young mice, activated microglia migrated to the blood vessels, removed the endothelial tight junctions and allowed the extravasation of the peripherally injected dextrans into the brain (Haruwaka *et al.* 2019). Therefore, it is plausible to speculate that sepsis can exacerbate the BBB breakdown, which has been already induced by ageing, and permit the entry of potentially neurotoxic or synaptotoxic peripheral proteins into the brains (such as heparan sulfate fragments (Hippensteel *et al.* 2019), albumin (Hooper *et al.* 2009) and fibrinogen (Merlini *et al.* 2019)).

Congruent with the changes in BBB permeability, monocytes are frequently observed in the mouse brains after systemic inflammation and may have pathological roles in patients with SAE (Singer *et al.* 2016a; Andonegui *et al.* 2018) (**Fig. 19A**). Once entering the brain, monocytes should differentiate into the macrophages or dendritic cells. These monocyte-derived cells may exaggerate the neuroinflammatory responses (as observed in mouse models of experimental autoimmune encephalomyelitis (EAE) and traumatic brain injury) (Garré and Yang 2018) and affect the synaptic plasticity by eliminating synapses (as recently found in mouse models of a focal EAE (Jafari *et al.* 2021)). Furthermore, several studies reported that memory and learning deficits in mouse models of the gram-positive bacterial infection and viral infection were rescued by monocyte depletion (Andonegui *et al.* 2018; Garré *et al.* 2017), which further supports the potential roles of monocytes in cerebral damages after the sepsis onset.

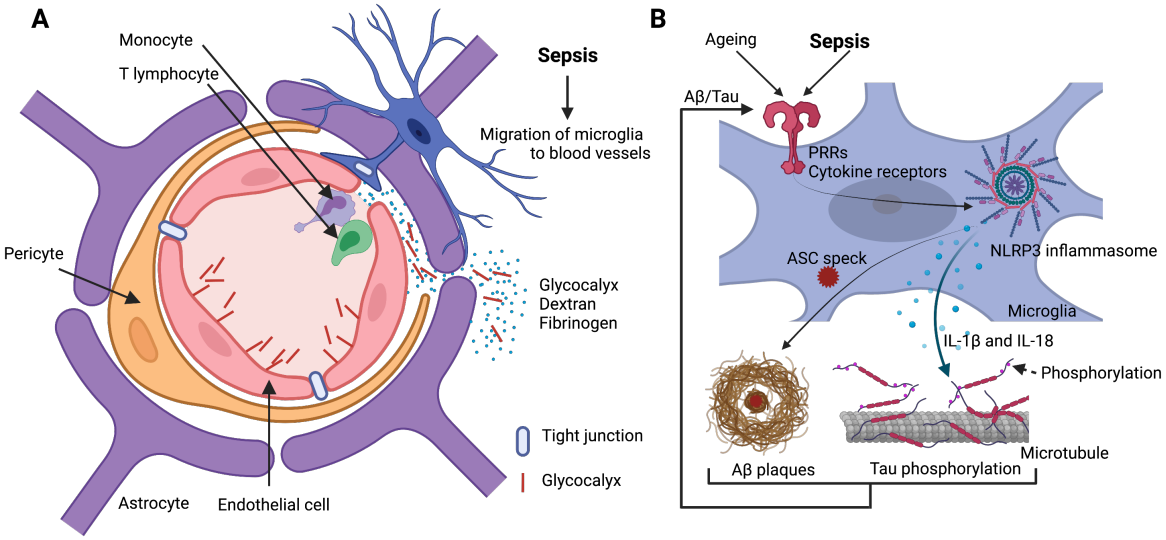

Figure 19. Possible roles of cerebrovascular changes and other pathology.
(A) Increased blood-brain barrier (BBB) permeability after sepsis. The integrity of endothelial tight junction, which determines the BBB permeability, can be compromised by the uptake of tight junctions by microglia migrated to the neurovascular unit (Haruwaka *et al.* 2019). This seems to contribute to the infiltration of monocytes extravasation of small peripheral proteins in the brain (such as dextran (Haruwaka *et al.* 2019) and heparan sulfate fragments as a result of glycocalyx degradation (Hippensteel *et al.* 2019)). If the BBB integrity has been affected by other age-related pathology such as amyloid pathology, systemic inflammation may permit the entry of larger peripheral proteins (including fibrinogen (Tejera *et al.*

2019)) and infiltration of monocytes and T lymphocytes (Tejera *et al.* 2019; McManus *et al.* 2014).

(B) The NLRP3 inflammasome activation connecting sepsis with amyloid and tau pathology. Because the NLRP3 inflammasome activation plays a role in the pathogenesis of the amyloid pathology (by cross-seeding Aβ via ASC specks (Venegas *et al.* 2017)) and the tau pathology (by regulating kinase and phosphatase activity in neurons (Ising *et al.* 2019)), it is likely that sepsis can worsen the progression of these pathologies (as observed in the aged mouse model of familial Alzheimer's disease which was challenged by endotoxin (Tejera *et al.* 2019)).

This figure was created using BioRender (https://biorender.com/).

Abbreviations: ASC, apoptosis associated speck-like protein containing a caspase recruitment domain; NLRP3, NOD-, LRR- and pyrin domain-containing protein 3; PRRs, pattern recognition receptors.

6.3.2 Premorbid pathology

It is important to underscore that ageing alone is not sufficient for developing and maintaining cognitive disturbances in patients with sepsis, hinting at the possible actions of predisposing factors in the SAE pathogenesis (Sonneville *et al.* 2017; Fritze *et al.* 2021). One possible factor may be a premorbid pathology related to neurodegenerative diseases. Notably, Aβ deposition starts in the brain two decades before patients are diagnosed with AD (Bateman *et al.* 2012). Individuals retaining the normal cognitive functions (cognitive reserve) can also present abundant neuropathological hallmarks of AD (that is, Aβ plaques and NFTs) on *post-mortem* investigations at the equal levels to those observed in patients with AD (Savva *et al.* 2009). Thus, considering that sepsis is an age-related disease, the presence of these neuropathologies is probable in some of the cognitively unimpaired individuals at the time of sepsis onset, and these premorbid pathologies may help to differentiate the effects of sepsis on cognitive functions. In support, LPS injections into aged APP/PS1 mice led to exaggerated reductions of dendritic spine density in CA1 and DG at three months post-injection, compared with LPS-injected wild-type controls (Beyer *et al.* 2020). Both endotoxin challenge and respiratory infection also resulted in a robust BBB breakdown (for instance, extravasation of fibrinogen and infiltration of monocytes

and T lymphocytes into the brain) in the aged APP/PS1 mice, but not in the age-matched wild-type littermates (Tejera *et al.* 2019; McManus *et al.* 2014) (**Fig. 19A**).

In addition, previous findings indicated that systemic inflammation can worsen the amyloid and tau pathology in mouse models, and again the NLRP3 inflammasome may be involved in this process (**Fig. 19B**). For example, CLP and endotoxin challenge in APP/PS1 mice increased the Aβ deposition without affecting the APP processing (Tejera *et al.* 2019; Basak *et al.* 2021). Since sepsis can activate the NLRP3 inflammasome and generate the ASC specks, which can cross-seed Aβ and help to generate Aβ plaques in APP/PS1 mice (Venegas *et al.* 2017), extracellular ASC speck release may likely contribute to enhancing the amyloid pathology (Tejera *et al.* 2019). Consistent with our data showing the reduced synaptic pruning following endotoxin challenge in C57BL6/N mice, activated microglia diminish the phagocytosis of Aβ, aiding the accumulation of Aβ in the brain (Tejera *et al.* 2019). Thus, it seems possible that systemic inflammation promotes depositions of synaptotoxic Aβ oligomers at synapses, which is required for microglia to recognise and eliminate the synapses in the animal models of AD (Hong *et al.* 2016). Additionally, tau phosphorylation in the hippocampus can be increased after endotoxin injection into young mice overexpressing the human *MAPT*, *APP* and *PS1* mutations (Kitazawa *et al.* 2005). Considering that NLRP3 deficiency significantly delays or hinders the onset of tau pathology in *MAPT* transgenic mice during ageing (Ising *et al.* 2019), it is likely that the effects of systemic inflammation on tau pathology may be mediated by the NLRP3 inflammasome activation. In another model of FTD (that is, P301S *MAPT* transgenic mice), synapse loss in CA3 is documented after the increased tau phosphorylation in the same region (Yoshiyama *et al.* 2007). Hence, it seems plausible that systemic inflammation can also exacerbate or accelerate the onset of synapse destructions via tau pathology.

6.3.3 Renal dysfunctions

Previous epidemiological studies highlighted that renal dysfunction is common in patients with sepsis and SAE and may underly the chronic pathology among those who survived sepsis. A recent large-scale analysis of patients with sepsis (n=1,636) demonstrated that the majority (61%) presented acute kidney injury (AKI) at the time

of diagnosis and approximately one-fifth (19%) of these survivors in the AKI group developed CKD within a year after the onset (Arshad *et al.* 2020). Renal pathology is also suggested as a candidate mechanism for the sustained inflammation in PICS because renal damages can upregulate TLRs in the renal tubule epithelial cells of animal models of AKI, leading to the exaggerated cytokine production following endotoxin challenge (namely, immune training) (Hawkins *et al.* 2018). Since patients who survive sepsis display recurrence of sepsis after the hospital discharge (Prescott *et al.* 2015), peripheral inflammation may be maintained in the survivors with AKI. On the other hand, renal dysfunction seems to be relevant for SAE pathology because plasma biomarkers indicating the renal dysfunctions (such as bilirubin and blood urea nitrogen) were found to be higher in patients with SAE (Eidelman *et al.* 1996), and AKI increased the risk of encephalopathy in patients with sepsis in ICU (Sonneville *et al.* 2017).

Regarding the molecular mechanisms that connect renal failures with SAE, it is reasonable to speculate that uraemic toxins, which the kidney fails to filter out due to its dysfunction, may play a role in cerebral damages. It is known that some of these uraemic toxins (for example, IL-1β and IL-6) are neurotoxic and pass through the BBB (Viggiano *et al.* 2020). Animal models of CKD suggested that kidney failures (caused by an adenine-rich diet and nephrectomy) resulted in memory deficits via BBB breakdown (Bobot *et al.* 2020), and such cerebrovascular changes were further augmented after LPS injections (Lau *et al.* 2020). For this reason, we speculated that the delayed CA3 synapse loss shown in this study might be related to the secondary effect of systemic inflammation.

6.3.4 Latent viral reactivation

Lastly, given the fact that clinical trials of sepsis have repeatedly failed in the last three decades (Cavaillon *et al.* 2020), the differences between patients with sepsis and animal models need to be taken into account, and an important aspect to be considered is the prior infection by latent viruses. It is known that pathogenic viruses (for instance, HSV-1, EBV and CMV) can infect the majority of humans until adulthood and stop replicating in the periphery and CNS (including but not restricted to the hippocampus and frontal cortex) (Looker *et al.* 2015; Marcocci *et al.* 2020; Cannon *et*

al. 2010; Balfour *et al.* 2013). However, in patients with sepsis, these latent viruses are found to be reactivated in the periphery (Walton *et al.* 2014). Animal models also confirmed that the latent viruses can be reactivated following the endotoxin challenge and proinflammatory cytokine injection (Cook *et al.* 2006).

Consequences of the latent virus reactivation in the brains of patients with sepsis remain largely unknown. However, a recent study of HSV-1 reactivation in the mouse trigeminal ganglion showed that the viral reactivation leads to apoptotic fragmentations of the infected neurons surrounded by a cluster of microglial cells (known as microglial nodule) (Doll *et al.* 2020). This microglial nodule has been found in the brains of deceased patients with COVID-19 which frequently develops viral sepsis in severe cases (Matschke *et al.* 2020; Zhou *et al.* 2020). Although this may reflect the neuroinvasion of the causative virus as suggested by several groups of investigators (Matschke *et al.* 2020; Meinhardt *et al.* 2021; Song *et al.* 2021), the observation of microglial nodule provides some evidence that latent virus reactivation may be induced in the brain of patients with viral sepsis. Together, it is plausible that if the latent viruses exist in a patient's brain, sepsis may reactivate these viruses via proinflammatory cytokines and induce rapid apoptosis of the infected neurons. Future research will be needed to investigate the links of latent viral reactivation to the long-lasting cerebral damages using animal models and patients with sepsis.

Chapter 7: Conclusion

Systemic inflammation elicited by endotoxin injections in old mice increased the proinflammatory cytokine levels, activated the NLRP3 inflammasome and consequently changed the microglial morphology. Because most of these changes that we detected were rather mild, the neuroinflammatory responses should be returning to homeostasis at 7 dpi. Many of our data showed more pronounced effects on these parameters associated with neuroinflammation in *E. coli* LPS treated group than in *Salmonella* LPS treated group. This suggested that the *E. coli* LPS may produce stronger or sustained inflammatory responses in the brain.

Both of the bacterial serotypes of LPS similarly led to the local reduction of excitatory synaptic puncta in the CA3 subfield of the hippocampus at 63 dpi. Our biochemical analysis of synaptosomes demonstrated that global loss of synaptic proteins was not induced following systemic inflammation. Due to the resulting increase in the inhibitory tone of the Schaffer collaterals, it seems likely that other region of the hippocampal subfield such as CA1 may be affected if the analysis is performed at a later point in time via reduced microglial contacts with dendritic spines. Further investigations are needed to test whether these synaptic changes can chronically alter the behaviours associated with memory and learning.

Mechanisms that cause the CA3-specific synapse loss remain elusive. Considering the reduced proportion of C3-coated synapses and the density of synaptic C3 puncta in CA3, we cannot rule out the possibility that microglial synaptic pruning was increased between 7 dpi and 63 dpi. This might occur in response to a second hit of the CNS (for example, via infiltration of peripheral proteins as a consequence of peripheral organ failures). Instead, it is also likely that the C5a-C5aR axis might be activated at CA3 excitatory synapses, thereby promoting the elimination of these synapses by microglia.

Intriguingly, microglial and astrocytic senescence was not observed by endotoxin challenges on up to seven consecutive days. This indicated that the duration of the NLRP3 inflammasome activation were not sufficient in the mice that we used. If not, a more advanced age or additional age-related neurodegenerative pathologies which

increase the baseline levels of NLRP3 inflammasome activation might have been required.

Meanwhile, we also sought to seek the disease-modifying roles of TREM2 in 12-month-old APP/PS1 mice. We showed fewer Aβ plaques but more abundant oligomeric Aβ in the cortex of *Trem2* mutant mice. Despite this, we found the elevated density of excitatory synaptic puncta in the same region of *Trem2* mutant mice, suggesting that even though more synaptotoxic Aβ oligomers are present, microglial synaptic pruning may require the TREM2 pathway.

List of Publications

1. **Manabe, T.**, Rácz, I., Schwartz, S., Oberle, L., Santarelli, F., Emmrich, J.V., Neher, J.J., Heneka, M.T. (2021) Systemic inflammation induced the delayed reduction of excitatory synapses in the CA3 during ageing. *J. Neurochem. https://doi.org/10.1111/jnc.15491*

Manuscript submitted

1. **Manabe, T.** & Heneka, M.T. Cerebral dysfunctions caused by sepsis during ageing. Submitted to the Nature Reviews Immunology. Under the revision.

Manuscript in preparation

1. Villacampa, N.*, Tejera, D.*, Kumar, S., Joshi, P., **Manabe, T.**, Saecker, A.V., Schwartz, S., Walter, J., Heneka, M.T. Loss of TREM2 function increases ASC-specks formation and impairs microglia function.

Conferences

1. **Manabe, T.**, Rácz, I., Schwartz, S., Santarelli, F., Emmrich, J.V., Neher, J.J., Heneka, M.T. (2021) CA3 Excitatory Synapse Loss as a Chronic Effect of Septic Shock in Middle-aged Mice. Alzheimer's Association International Conference (AAIC) 2021, virtual. Poster presentation.
2. **Manabe, T.**, Rácz, I., Schwartz, S., Emmrich, J.V., Neher, J.J., Heneka, M.T. (2019) Investigation of Microglia-neuron Interactions in Response to Septic Shock. Venusberg Meeting on Neuroinflammation, Bonn, Germany. Poster presentation.
3. **Manabe, T.**, Rácz, I., Schwartz, S., Emmrich, J.V., Neher, J.J., Heneka, M.T. (2019) Investigation of Microglia-neuron Interactions in Response to Septic Shock. Clusters Science Day, Bonn, Germany. Poster presentation.

List of Figures

List of Tables

References

Andonegui G., Zelinski E. L., Schubert C. L., Knight D., Craig L. A., Winston B. W., Spanswick S. C., et al. (2018) Targeting inflammatory monocytes in sepsis-associated encephalopathy and long-term cognitive impairment. *JCI Insight* **3**, e99364.

Arganda-Carreras I., Fernández-González R., Muñoz-Barrutia A., Ortiz-De-Solorzano C. (2010) 3D reconstruction of histological sections: Application to mammary gland tissue. *Microsc. Res. Tech.* **73**, 1019–1029.

Arshad A., Ayaz A., Rehman S., Ukrani R. D., Akbar I., Jamil B. (2020) Progression of Acute Kidney Injury to Chronic Kidney Disease in Sepsis Survivors: 1-Year Follow-Up Study. *J. Intensive Care Med.*, 885066620956621.

Baker D. J., Petersen R. C. (2018) Cellular senescence in brain aging and neurodegenerative diseases: evidence and perspectives. *J. Clin. Invest.* **128**, 1208–1216.

Balfour H. H. Jr, Sifakis F., Sliman J. A., Knight J. A., Schmeling D. O., Thomas W. (2013) Age-Specific Prevalence of Epstein–Barr Virus Infection Among Individuals Aged 6–19 Years in the United States and Factors Affecting Its Acquisition. *J. Infect. Dis.* **208**, 1286–1293.

Barascu A., Le Chalony C., Pennarun G., Genet D., Imam N., Lopez B., Bertrand P. (2012) Oxidative stress induces an ATM-independent senescence pathway through p38 MAPK-mediated lamin B1 accumulation. *EMBO J.* **31**, 1080–1094.

Basak J. M., Ferreiro A., Cohen L. S., Sheehan P. W., Nadarajah C. J., Kanan M. F., Sukhum K. V., Dantas G., Musiek E. S. (2021) Bacterial sepsis increases hippocampal fibrillar amyloid plaque load and neuroinflammation in a mouse model of Alzheimer's disease. *Neurobiol. Dis.* **152**, 105292.

Bateman R. J., Xiong C., Benzinger T. L. S., Fagan A. M., Goate A., Fox N. C., Marcus D. S., et al. (2012) Clinical and biomarker changes in dominantly inherited Alzheimer's disease. *N. Engl. J. Med.* **367**, 795–804.

Beyer M. M. S., Lonnemann N., Remus A., Latz E., Heneka M. T., Korte M. (2020) Enduring Changes in Neuronal Function upon Systemic Inflammation Are NLRP3 Inflammasome Dependent. *J. Neurosci.* **40**, 5480–5494.

Bobot M., Thomas L., Moyon A., Fernandez S., McKay N., Balasse L., Garrigue P., et al. (2020) Uremic Toxic Blood-Brain Barrier Disruption Mediated by AhR Activation Leads to Cognitive Impairment during Experimental Renal Dysfunction. *J. Am. Soc. Nephrol.* **31**, 1509–1521.

Bodea L.-G., Wang Y., Linnartz-Gerlach B., Kopatz J., Sinkkonen L., Musgrove R., Kaoma T., et al. (2014) Neurodegeneration by activation of the microglial complement-phagosome pathway. *J. Neurosci.* **34**, 8546–8556.

Bone R. C., Balk R. A., Cerra F. B., Dellinger R. P., Fein A. M., Knaus W. A., Schein R. M., Sibbald W. J. (1992) Definitions for sepsis and organ failure and guidelines for the use of innovative therapies in sepsis. The ACCP/SCCM Consensus Conference Committee. American College of Chest Physicians/Society of Critical Care Medicine. *Chest* **101**, 1644–1655.

Broadhead M. J., Horrocks M. H., Zhu F., Muresan L., Benavides-Piccione R., DeFelipe J., Fricker D., et al. (2016) PSD95 nanoclusters are postsynaptic building blocks in hippocampus circuits. *Sci. Rep.* **6**, 24626.

Cannon M. J., Schmid D. S., Hyde T. B. (2010) Review of cytomegalovirus seroprevalence and demographic characteristics associated with infection. *Rev. Med. Virol.* **20**, 202–213.

Cavaillon J., Singer M., Skirecki T. (2020) Sepsis therapies: learning from 30 years of failure of translational research to propose new leads. *EMBO Mol. Med.* **12**, e10128.

Chang C.-W., Chiu C.-H., Lin M.-H., Wu H.-M., Yu T.-H., Wang P.-Y., Kuo Y.-Y., et al. (2021) GMP-compliant fully automated radiosynthesis of [18F]FEPPA for PET/MRI imaging of regional brain TSPO expression. *EJNMMI Res.* **11**, 26.

Chaudhry F. A., Reimer R. J., Bellocchio E. E., Danbolt N. C., Osen K. K., Edwards R. H., Storm-Mathisen J. (1998) The Vesicular GABA Transporter, VGAT, Localizes to Synaptic Vesicles in Sets of Glycinergic as Well as GABAergic Neurons. *J. Neurosci.* **18**, 9733–9750.

Chavan S. S., Huerta P. T., Robbiati S., Valdes-Ferrer S. I., Ochani M., Dancho M., Frankfurt M., Volpe B. T., Tracey K. J., Diamond B. (2012) HMGB1 Mediates Cognitive Impairment in Sepsis Survivors. *Mol. Med.* **18**, 930–937.

Chelazzi C., Villa G., Mancinelli P., De Gaudio A. R., Adembri C. (2015) Glycocalyx and sepsis-induced alterations in vascular permeability. *Crit. Care* **19**.

Chen J., Buchanan J. B., Sparkman N. L., Godbout J. P., Freund G. G., Johnson R. W. (2008) Neuroinflammation and disruption in working memory in aged mice after acute stimulation of the peripheral innate immune system. *Brain Behav. Immun.* **22**, 301–311.

Chen Z., Jalabi W., Hu W., Park H.-J., Gale J. T., Kidd G. J., Bernatowicz R., et al. (2014) Microglial displacement of inhibitory synapses provides neuroprotection in the adult brain. *Nat. Commun.* **5**, 4486.

Chen Z., Jalabi W., Shpargel K. B., Farabaugh K. T., Dutta R., Yin X., Kidd G. J., Bergmann C. C., Stohlman S. A., Trapp B. D. (2012) Lipopolysaccharide-Induced Microglial Activation and Neuroprotection against Experimental Brain Injury Is Independent of Hematogenous TLR4. *J. Neurosci.* **32**, 11706–11715.

Choi H. B., Ryu J. K., Kim S. U., McLarnon J. G. (2007) Modulation of the Purinergic P2X7 Receptor Attenuates Lipopolysaccharide-Mediated Microglial Activation and Neuronal Damage in Inflamed Brain. *J. Neurosci.* **27**, 4957–4968.

Cook C. H., Trgovcich J., Zimmerman P. D., Zhang Y., Sedmak D. D. (2006) Lipopolysaccharide, tumor necrosis factor alpha, or interleukin-1beta triggers reactivation of latent cytomegalovirus in immunocompetent mice. *J. Virol.* **80**, 9151–9158.

Crane J. W., Baiquni G. P., Sullivan R. K., Lee J. D., Sah P., Taylor S. M., Noakes P. G., Woodruff T. M. (2009) The C5a anaphylatoxin receptor CD88 is expressed in presynaptic terminals of hippocampal mossy fibres. *J. Neuroinflammation* **6**, 34.

Dantzer R., Kelley K. W. (2007) Twenty Years of Research on Cytokine-Induced Sickness Behavior. *Brain Behav. Immun.* **21**, 153–160.

Davenport E. E., Burnham K. L., Radhakrishnan J., Humburg P., Hutton P., Mills T. C., Rautanen A., et al. (2016) Genomic landscape of the individual host response and outcomes in sepsis: a prospective cohort study. *Lancet Respir. Med.* **4**, 259–271.

Deng X., Wang Y., Chou J., Cadet J. L. (2001) Methamphetamine causes widespread apoptosis in the mouse brain: evidence from using an improved TUNEL histochemical method. *Mol. Brain Res.* **93**, 64–69.

Doll J. R., Hoebe K., Thompson R. L., Sawtell N. M. (2020) Resolution of herpes simplex virus reactivation in vivo results in neuronal destruction. *PLoS Pathog.* **16**, e1008296.

Doube M., Kłosowski M. M., Arganda-Carreras I., Cordelières F. P., Dougherty R. P., Jackson J. S., Schmid B., Hutchinson J. R., Shefelbine S. J. (2010) BoneJ: Free and extensible bone image analysis in ImageJ. *Bone* **47**, 1076–1079.

Dumitriu D., Hao J., Hara Y., Kaufmann J., Janssen W. G. M., Lou W., Rapp P. R., Morrison J. H. (2010) Selective Changes in Thin Spine Density and Morphology in Monkey Prefrontal Cortex Correlate with Aging-Related Cognitive Impairment. *J. Neurosci.* **30**, 7507–7515.

Ehler J., Barrett L. K., Taylor V., Groves M., Scaravilli F., Wittstock M., Kolbaske S., et al. (2017) Translational evidence for two distinct patterns of neuroaxonal injury in sepsis: a longitudinal, prospective translational study. *Crit. Care* **21**, 262.

Eidelman L. A., Putterman D., Putterman C., Sprung C. L. (1996) The Spectrum of Septic Encephalopathy: Definitions, Etiologies, and Mortalities. *JAMA* **275**, 470–473.

Fajgenbaum D. C., June C. H. (2020) Cytokine Storm. *N. Engl. J. Med.* **383**, 2255–2273.

Faul F., Erdfelder E., Lang A.-G., Buchner A. (2007) G*Power 3: a flexible statistical power analysis program for the social, behavioral, and biomedical sciences. *Behav. Res. Methods* **39**, 175–191.

Filipello F., Morini R., Corradini I., Zerbi V., Canzi A., Michalski B., Erreni M., et al. (2018) The Microglial Innate Immune Receptor TREM2 Is Required for Synapse Elimination and Normal Brain Connectivity. *Immunity* **48**, 979-991.e8.

Finnema S. J., Nabulsi N. B., Eid T., Detyniecki K., Lin S., Chen M.-K., Dhaher R., et al. (2016) Imaging synaptic density in the living human brain. *Sci. Transl. Med.* **8**, 348ra96-348ra96.

Flierl M. A., Stahel P. F., Rittirsch D., Huber-Lang M., Niederbichler A. D., Hoesel L. M., Touban B. M., et al. (2009) Inhibition of complement C5a prevents breakdown of the blood-brain barrier and pituitary dysfunction in experimental sepsis. *Crit. Care* **13**, R12.

Franceschi C., Capri M., Monti D., Giunta S., Olivieri F., Sevini F., Panourgia M. P., et al. (2007) Inflammaging and anti-inflammaging: A systemic perspective on aging and longevity emerged from studies in humans. *Mech. Ageing Dev.* **128**, 92–105.

Franceschi C., Garagnani P., Vitale G., Capri M., Salvioli S. (2017) Inflammaging and 'Garb-aging.' *Trends Endocrinol. Metab.* **28**, 199–212.

Freund A., Laberge R.-M., Demaria M., Campisi J. (2012) Lamin B1 loss is a senescence-associated biomarker. *MBoC* **23**, 2066–2075.

Fricker M., Neher J. J., Zhao J.-W., Théry C., Tolkovsky A. M., Brown G. C. (2012) MFG-E8 mediates primary phagocytosis of viable neurons during neuroinflammation. *J. Neurosci.* **32**, 2657–2666.

Fritze T., Doblhammer G., Widmann C. N., Heneka M. T. (2021) Time course of dementia following sepsis in German health claims data. *Neurol. Neuroimmunol. Neuroinflamm.* **8**, e911.

Garré J. M., Silva H. M., Lafaille J. J., Yang G. (2017) CX3CR1+ monocytes modulate learning and learning-dependent dendritic spine remodeling via TNF-α. *Nat. Med.* **23**, 714–722.

Garré J. M., Yang G. (2018) Contributions of monocytes to nervous system disorders. *J. Mol. Med.* **96**, 873–883.

Gentile L. F., Cuenca A. G., Efron P. A., Ang D., Bihorac A., McKinley B. A., Moldawer L. L., Moore F. A. (2012) Persistent inflammation and immunosuppression: A common syndrome and new horizon for surgical intensive care. *J. Trauma Acute Care Surg.* **72**, 1491–1501.

Ghaly T., Rabadi M. M., Weber M., Rabadi S. M., Bank M., Grom J. M., Fallon J. T., Goligorsky M. S., Ratliff B. B. (2011) Hydrogel-embedded endothelial progenitor cells evade LPS and mitigate endotoxemia. *Am. J. Physiol. Renal Physiol.* **301**, F802–F812.

Godbout J. P., Chen J., Abraham J., Richwine A. F., Berg B. M., Kelley K. W., Johnson R. W. (2005) Exaggerated neuroinflammation and sickness behavior in aged mice following activation of the peripheral innate immune system. *FASEB J.* **19**, 1329–1331.

Goldberg E. L., Dixit V. D. (2015) Drivers of age-related inflammation and strategies for healthspan extension. *Immunol. Rev.* **265**, 63–74.

Gorgoulis V., Adams P. D., Alimonti A., Bennett D. C., Bischof O., Bishop C., Campisi J., et al. (2019) Cellular Senescence: Defining a Path Forward. *Cell* **179**, 813–827.

Guerreiro R. J., Lohmann E., Brás J. M., Gibbs J. R., Rohrer J. D., Gurunlian N., Dursun B., et al. (2013a) Using exome sequencing to reveal mutations in TREM2 presenting as a frontotemporal dementia-like syndrome without bone involvement. *JAMA Neurol.* **70**, 78–84.

Guerreiro R., Wojtas A., Bras J., Carrasquillo M., Rogaeva E., Majounie E., Cruchaga C., et al. (2013b) TREM2 variants in Alzheimer's disease. *N. Engl. J. Med.* **368**, 117–127.

Gunther M. L., Morandi A., Krauskopf E., Pandharipande P., Girard T. D., Jackson J. C., Thompson J., et al. (2012) The association between brain volumes, delirium duration, and cognitive outcomes in intensive care unit survivors: The VISIONS cohort magnetic resonance imaging study. *Crit. Care Med.* **40**, 2022–2032.

Harland M., Torres S., Liu J., Wang X. (2020) Neuronal Mitochondria Modulation of LPS-Induced Neuroinflammation. *J. Neurosci.* **40**, 1756–1765.

Haruwaka K., Ikegami A., Tachibana Y., Ohno N., Konishi H., Hashimoto A., Matsumoto M., et al. (2019) Dual microglia effects on blood brain barrier permeability induced by systemic inflammation. *Nat. Commun.* **10**, 5816.

Hashimoto K., Panchenko A. R. (2010) Mechanisms of protein oligomerization, the critical role of insertions and deletions in maintaining different oligomeric states. *Proc. Natl. Acad. Sci. U.S.A.* **107**, 20352–20357.

Hawkins R. B., Raymond S. L., Stortz J. A., Horiguchi H., Brakenridge S. C., Gardner A., Efron P. A., et al. (2018) Chronic Critical Illness and the Persistent Inflammation, Immunosuppression, and Catabolism Syndrome. *Front. Immunol.* **9**, 1511.

He M., Chiang H.-H., Luo H., Zheng Z., Qiao Q., Wang L., Tan M., et al. (2020) An Acetylation Switch of the NLRP3 Inflammasome Regulates Aging-Associated Chronic Inflammation and Insulin Resistance. *Cell Metab.* **31**, 580-591.e5.

He Y., Hara H., Núñez G. (2016) Mechanism and Regulation of NLRP3 Inflammasome Activation. *Trends Biochem. Sci.* **41**, 1012–1021.

Heneka M. T., Golenbock D. T., Latz E. (2015) Innate immunity in Alzheimer's disease. *Nat. Immunol.* **16**, 229–236.

Heneka M. T., Kummer M. P., Stutz A., Delekate A., Schwartz S., Vieira-Saecker A., Griep A., et al. (2013) NLRP3 is activated in Alzheimer's disease and contributes to pathology in APP/PS1 mice. *Nature* **493**, 674–678.

Heneka M. T., McManus R. M., Latz E. (2018) Inflammasome signalling in brain function and neurodegenerative disease. *Nat. Rev. Neurosci.* **19**, 610–621.

Hippensteel J. A., Anderson B. J., Orfila J. E., McMurtry S. A., Dietz R. M., Su G., Ford J. A., et al. (2019) Circulating heparan sulfate fragments mediate septic cognitive dysfunction. *J. Clin. Invest.* **129**, 1779–1784.

Hong S., Beja-Glasser V. F., Nfonoyim B. M., Frouin A., Li S., Ramakrishnan S., Merry K. M., et al. (2016) Complement and microglia mediate early synapse loss in Alzheimer mouse models. *Science* **352**, 712–716.

Hooper C., Pinteaux-Jones F., Fry V. A. H., Sevastou I. G., Baker D., Heales S. J., Pocock J. M. (2009) Differential effects of albumin on microglia and macrophages; implications for neurodegeneration following blood–brain barrier damage. *J. Neurochem.* **109**, 694–705.

Hosokawa K., Gaspard N., Su F., Oddo M., Vincent J.-L., Taccone F. S. (2014) Clinical neurophysiological assessment of sepsis-associated brain dysfunction: a systematic review. *Crit. Care* **18**, 674.

Hosseini S., Wilk E., Michaelsen-Preusse K., Gerhauser I., Baumgärtner W., Geffers R., Schughart K., Korte M. (2018) Long-Term Neuroinflammation Induced by Influenza A Virus Infection and the Impact on Hippocampal Neuron Morphology and Function. *J. Neurosci.* **38**, 3060–3080.

Hotchkiss R. S., Coopersmith C. M., McDunn J. E., Ferguson T. A. (2009) Tilting toward immunosuppression. *Nat. Med.* **15**, 496–497.

Hotchkiss R. S., Moldawer L. L., Opal S. M., Reinhart K., Turnbull I. R., Vincent J.-L. (2016) Sepsis and septic shock. *Nat. Rev. Dis. Primers* **2**, 16045.

Hu Y., Fryatt G. L., Ghorbani M., Obst J., Menassa D. A., Martin-Estebane M., Muntslag T. A. O., et al. (2021) Replicative senescence dictates the emergence of disease-associated microglia and contributes to Aβ pathology. *Cell Rep.* **35**, 109228.

Huerta P. T., Robbiati S., Huerta T. S., Sabharwal A., Berlin R., Frankfurt M., Volpe B. T. (2016) Preclinical Models of Overwhelming Sepsis Implicate the Neural System that Encodes Contextual Fear Memory. *Mol. Med.* **22**, 789–799.

Huff J. (2015) The Airyscan detector from ZEISS: confocal imaging with improved signal-to-noise ratio and super-resolution. *Nat. Methods* **12**, i–ii.

Inouye S. K., Robinson T., Blaum C., Busby-Whitehead J., Boustani M., Chalian A., Deiner S., et al. (2015) Postoperative Delirium in Older Adults: Best Practice Statement from the American Geriatrics Society. *J. Am. Coll. Surg.* **220**, 136-148.e1.

Ising C., Venegas C., Zhang S., Scheiblich H., Schmidt S. V., Vieira-Saecker A., Schwartz S., et al. (2019) NLRP3 inflammasome activation drives tau pathology. *Nature* **575**, 669–673.

Iwashyna T. J., Ely E. W., Smith D. M., Langa K. M. (2010) Long-term cognitive impairment and functional disability among survivors of severe sepsis. *JAMA* **304**, 1787–1794.

Jacob A., Hensley L. K., Safratowich B. D., Quigg R. J., Alexander J. J. (2007) The role of the complement cascade in endotoxin-induced septic encephalopathy. *Lab. Invest.* **87**, 1186–1194.

Jafari M., Schumacher A.-M., Snaidero N., Ullrich Gavilanes E. M., Neziraj T., Kocsis-Jutka V., Engels D., et al. (2021) Phagocyte-mediated synapse

removal in cortical neuroinflammation is promoted by local calcium accumulation. *Nat. Neurosci.* **24**, 355–367.

Jankowsky J. L., Slunt H. H., Ratovitski T., Jenkins N. A., Copeland N. G., Borchelt D. R. (2001) Co-expression of multiple transgenes in mouse CNS: a comparison of strategies. *Biomol. Eng.* **17**, 157–165.

Jay T. R., Hirsch A. M., Broihier M. L., Miller C. M., Neilson L. E., Ransohoff R. M., Lamb B. T., Landreth G. E. (2017) Disease Progression-Dependent Effects of TREM2 Deficiency in a Mouse Model of Alzheimer's Disease. *J. Neurosci.* **37**, 637–647.

Jay T. R., Miller C. M., Cheng P. J., Graham L. C., Bemiller S., Broihier M. L., Xu G., et al. (2015) TREM2 deficiency eliminates TREM2+ inflammatory macrophages and ameliorates pathology in Alzheimer's disease mouse models. *J. Exp. Med.* **212**, 287–295.

Jin S. C., Benitez B. A., Karch C. M., Cooper B., Skorupa T., Carrell D., Norton J. B., et al. (2014) Coding variants in TREM2 increase risk for Alzheimer's disease. *Hum. Mol. Genet.* **23**, 5838–5846.

Jinno S., Fleischer F., Eckel S., Schmidt V., Kosaka T. (2007) Spatial arrangement of microglia in the mouse hippocampus: a stereological study in comparison with astrocytes. *Glia* **55**, 1334–1347.

Jonsson T., Stefansson H., Steinberg S., Jonsdottir I., Jonsson P. V., Snaedal J., Bjornsson S., et al. (2013) Variant of TREM2 associated with the risk of Alzheimer's disease. *N. Engl. J. Med.* **368**, 107–116.

Kayagaki N., Wong M. T., Stowe I. B., Ramani S. R., Gonzalez L. C., Akashi-Takamura S., Miyake K., et al. (2013) Noncanonical Inflammasome Activation by Intracellular LPS Independent of TLR4. *Science* **341**, 1246–1249.

Kitazawa M., Oddo S., Yamasaki T. R., Green K. N., LaFerla F. M. (2005) Lipopolysaccharide-induced inflammation exacerbates tau pathology by a cyclin-dependent kinase 5-mediated pathway in a transgenic model of Alzheimer's disease. *J. Neurosci.* **25**, 8843–8853.

Kleinberger G., Brendel M., Mracsko E., Wefers B., Groeneweg L., Xiang X., Focke C., et al. (2017) The FTD-like syndrome causing TREM2 T66M mutation impairs microglia function, brain perfusion, and glucose metabolism. *EMBO J.* **36**, 1837–1853.

Knuefermann P., Nemoto S., Misra A., Nozaki N., Defreitas G., Goyert S. M., Carabello B. A., Mann D. L., Vallejo J. G. (2002) CD14-deficient mice are protected against lipopolysaccharide-induced cardiac inflammation and left ventricular dysfunction. *Circulation* **106**, 2608–2615.

Koffie R. M., Meyer-Luehmann M., Hashimoto T., Adams K. W., Mielke M. L., Garcia-Alloza M., Micheva K. D., et al. (2009) Oligomeric amyloid β associates with postsynaptic densities and correlates with excitatory synapse loss near senile plaques. *Proc. Natl. Acad. Sci. U.S.A.* **106**, 4012–4017.

Kohman R. A., Crowell B., Kusnecov A. W. (2010) Differential sensitivity to endotoxin exposure in young and middle-age mice. *Brain Behav. Immun.* **24**, 486–492.

Kondo S., Kohsaka S., Okabe S. (2011) Long-term changes of spine dynamics and microglia after transient peripheral immune response triggered by LPS in vivo. *Mol. Brain* **4**, 27.

Lamkanfi M., Sarkar A., Walle L. V., Vitari A. C., Amer A. O., Wewers M. D., Tracey K. J., Kanneganti T.-D., Dixit V. M. (2010) Inflammasome-Dependent Release of the Alarmin HMGB1 in Endotoxemia. *J. Immunol.* **185**, 4385–4392.

Lau W. L., Nunes A. C. F., Vasilevko V., Floriolli D., Lertpanit L., Savoj J., Bangash M., et al. (2020) Chronic Kidney Disease Increases Cerebral Microbleeds in Mouse and Man. *Transl. Stroke Res.* **11**, 122–134.

Lee J. W., Lee Y. K., Yuk D. Y., Choi D. Y., Ban S. B., Oh K. W., Hong J. T. (2008) Neuro-inflammation induced by lipopolysaccharide causes cognitive impairment through enhancement of beta-amyloid generation. *J. Neuroinflammation* **5**, 37.

Lemstra A. W., Groen in't Woud J. C. M., Hoozemans J. J. M., Haastert E. S. van, Rozemuller A. J. M., Eikelenboom P., Gool W. A. van (2007) Microglia activation in sepsis: a case-control study. *J. Neuroinflammation* **4**, 4.

Lerouge I., Vanderleyden J. (2002) O-antigen structural variation: mechanisms and possible roles in animal/plant–microbe interactions. *FEMS Microbiol. Rev.* **26**, 17–47.

Levy M. M., Fink M. P., Marshall J. C., Abraham E., Angus D., Cook D., Cohen J., et al. (2003) 2001 SCCM/ESICM/ACCP/ATS/SIS International Sepsis Definitions Conference. *Crit. Care Med.* **31**, 1250–1256.

Li S., Li B., Zhang L., Zhang G., Sun J., Ji M., Yang J. (2020a) A complement-microglial axis driving inhibitory synapse related protein loss might contribute to systemic inflammation-induced cognitive impairment. *Int. Immunopharmacol.* **87**, 106814.

Li T., Chiou B., Gilman C. K., Luo R., Koshi T., Yu D., Oak H. C., et al. (2020b) A splicing isoform of GPR56 mediates microglial synaptic refinement via phosphatidylserine binding. *EMBO J.* **39**, e104136.

Lin G.-L., McGinley J. P., Drysdale S. B., Pollard A. J. (2018) Epidemiology and Immune Pathogenesis of Viral Sepsis. *Front. Immunol.* **9**.

Linnartz-Gerlach B., Bodea L., Klaus C., Ginolhac A., Halder R., Sinkkonen L., Walter J., Colonna M., Neumann H. (2019) TREM2 triggers microglial density and age-related neuronal loss. *Glia* **67**, 539–550.

Litvinchuk A., Wan Y.-W., Swartzlander D. B., Chen F., Cole A., Propson N. E., Wang Q., Zhang B., Liu Z., Zheng H. (2018) Complement C3aR Inactivation Attenuates Tau Pathology and Reverses an Immune Network Deregulated in Tauopathy Models and Alzheimer's Disease. *Neuron* **100**, 1337-1353.e5.

Looker K. J., Magaret A. S., May M. T., Turner K. M. E., Vickerman P., Gottlieb S. L., Newman L. M. (2015) Global and Regional Estimates of Prevalent and Incident Herpes Simplex Virus Type 1 Infections in 2012. *PLoS One* **10**, e0140765.

Louveau A., Harris T. H., Kipnis J. (2015) Revisiting the Mechanisms of CNS Immune Privilege. *Trends Immunol.* **36**, 569–577.

Lu T., Pan Y., Kao S.-Y., Li C., Kohane I., Chan J., Yankner B. A. (2004) Gene regulation and DNA damage in the ageing human brain. *Nature* **429**, 883–891.

Marcocci M. E., Napoletani G., Protto V., Kolesova O., Piacentini R., Li Puma D. D., Lomonte P., Grassi C., Palamara A. T., De Chiara G. (2020) Herpes Simplex Virus-1 in the Brain: The Dark Side of a Sneaky Infection. *Trends Microbiol.* **28**, 808–820.

Marschallinger J., Iram T., Zardeneta M., Lee S. E., Lehallier B., Haney M. S., Pluvinage J. V., et al. (2020) Lipid droplet accumulating microglia represent a dysfunctional and pro-inflammatory state in the aging brain. *Nat. Neurosci.* **23**, 194–208.

Martin G. S., Mannino D. M., Eaton S., Moss M. (2003) The Epidemiology of Sepsis in the United States from 1979 through 2000. *N. Engl. J. Med.* **348**, 1546–54.

Matschke J., Lütgehetmann M., Hagel C., Sperhake J. P., Schröder A. S., Edler C., Mushumba H., et al. (2020) Neuropathology of patients with COVID-19 in Germany: a post-mortem case series. *Lancet Neurol.* **19**, 919–929.

McManus R. M., Higgins S. C., Mills K. H. G., Lynch M. A. (2014) Respiratory infection promotes T cell infiltration and amyloid-β deposition in APP/PS1 mice. *Neurobiol. Aging* **35**, 109–121.

Mecocci P., MacGarvey U., Kaufman A. E., Koontz D., Shoffner J. M., Wallace D. C., Beal M. F. (1993) Oxidative damage to mitochondrial DNA shows marked age-dependent increases in human brain. *Ann. Neurol.* **34**, 609–616.

Mei J., Riedel N., Grittner U., Endres M., Banneke S., Emmrich J. V. (2018) Body temperature measurement in mice during acute illness: implantable temperature transponder versus surface infrared thermometry. *Sci. Rep.* **8**, 3526.

Meilandt W. J., Ngu H., Gogineni A., Lalehzadeh G., Lee S.-H., Srinivasan K., Imperio J., et al. (2020) Trem2 Deletion Reduces Late-Stage Amyloid Plaque Accumulation, Elevates the Aβ42:Aβ40 Ratio, and Exacerbates Axonal Dystrophy and Dendritic Spine Loss in the PS2APP Alzheimer's Mouse Model. *J. Neurosci.* **40**, 1956–1974.

Meinhardt J., Radke J., Dittmayer C., Franz J., Thomas C., Mothes R., Laue M., et al. (2021) Olfactory transmucosal SARS-CoV-2 invasion as a port of central nervous system entry in individuals with COVID-19. *Nat. Neurosci.* **24**, 168–175.

Merlini M., Rafalski V. A., Rios Coronado P. E., Gill T. M., Ellisman M., Muthukumar G., Subramanian K. S., et al. (2019) Fibrinogen Induces Microglia-Mediated Spine Elimination and Cognitive Impairment in an Alzheimer's Disease Model. *Neuron* **101**, 1099-1108.e6.

Mingam R., De Smedt V., Amédée T., Bluthé R.-M., Kelley K. W., Dantzer R., Layé S. (2008) In vitro and in vivo evidence for a role of the P2X7 receptor in the release of IL-1β in the murine brain. *Brain Behav. Immun.* **22**, 234–244.

Miyamoto A., Wake H., Ishikawa A. W., Eto K., Shibata K., Murakoshi H., Koizumi S., Moorhouse A. J., Yoshimura Y., Nabekura J. (2016) Microglia contact induces synapse formation in developing somatosensory cortex. *Nat. Commun.* **7**, 12540.

Montagne A., Barnes S. R., Sweeney M. D., Halliday M. R., Sagare A. P., Zhao Z., Toga A. W., et al. (2015) Blood-Brain Barrier Breakdown in the Aging Human Hippocampus. *Neuron* **85**, 296–302.

Montagne A., Nation D. A., Sagare A. P., Barisano G., Sweeney M. D., Chakhoyan A., Pachicano M., et al. (2020) APOE4 leads to blood–brain barrier dysfunction predicting cognitive decline. *Nature* **581**, 71–76.

Mouton P. R., Kelley-Bell B., Tweedie D., Spangler E. L., Perez E., Carlson O. D., Short R. G., et al. (2012) The effects of age and lipopolysaccharide (LPS)-mediated peripheral inflammation on numbers of central catecholaminergic neurons. *Neurobiol. Aging* **33**, 423.e27–36.

Mullaly S. C., Kubes P. (2006) The Role of TLR2 In Vivo following Challenge with Staphylococcus aureus and Prototypic Ligands. *J. Immunol.* **177**, 8154–8163.

Muñoz-Planillo R., Kuffa P., Martínez-Colón G., Smith B. L., Rajendiran T. M., Núñez G. (2013) K+ efflux is the Common Trigger of NLRP3 inflammasome

Activation by Bacterial Toxins and Particulate Matter. *Immunity* **38**, 1142–1153.

Munster B. C. van, Korevaar J. C., Zwinderman A. H., Levi M., Wiersinga W. J., De Rooij S. E. (2008) Time-course of cytokines during delirium in elderly patients with hip fractures. *J. Am. Geriatr. Soc.* **56**, 1704–1709.

Musi N., Valentine J. M., Sickora K. R., Baeuerle E., Thompson C. S., Shen Q., Orr M. E. (2018) Tau protein aggregation is associated with cellular senescence in the brain. *Aging Cell* **17**, e12840.

Mutterer J., Zinck E. (2013) Quick-and-clean article figures with FigureJ. *J. Microsc.* **252**, 89–91.

Nabulsi N. B., Mercier J., Holden D., Carré S., Najafzadeh S., Vandergeten M.-C., Lin S., et al. (2016) Synthesis and Preclinical Evaluation of 11C-UCB-J as a PET Tracer for Imaging the Synaptic Vesicle Glycoprotein 2A in the Brain. *J. Nucl. Med.* **57**, 777–784.

Nakagawa T., Ohnishi K., Kosaki Y., Saito Y., Horlad H., Fujiwara Y., Takeya M., Komohara Y. (2017) Optimum immunohistochemical procedures for analysis of macrophages in human and mouse formalin fixed paraffin-embedded tissue samples. *J. Clin. Exp. Hematop.* **57**, 31–36.

Nation D. A., Sweeney M. D., Montagne A., Sagare A. P., D'Orazio L. M., Pachicano M., Sepehrband F., et al. (2019) Blood–brain barrier breakdown is an early biomarker of human cognitive dysfunction. *Nat. Med.* **25**, 270–276.

Netea M. G., Kullberg B. J., Joosten L. A., Sprong T., Verschueren I., Boerman O. C., Amiot F., Berg W. B. van den, Van der Meer J. W. (2001) Lethal Escherichia coli and Salmonella typhimurium endotoxemia is mediated through different pathways. *Eur. J. Immunol.* **31**, 2529–2538.

Olmos-Alonso A., Schetters S. T. T., Sri S., Askew K., Mancuso R., Vargas-Caballero M., Holscher C., Perry V. H., Gomez-Nicola D. (2016) Pharmacological targeting of CSF1R inhibits microglial proliferation and prevents the progression of Alzheimer's-like pathology. *Brain* **139**, 891–907.

Orhun G., Tüzün E., Bilgiç B., Ergin Özcan P., Sencer S., Barburoğlu M., Esen F. (2020) Brain Volume Changes in Patients with Acute Brain Dysfunction Due to Sepsis. *Neurocrit. Care* **32**, 459–468.

Ormerod B. K., Hanft S. J., Asokan A., Haditsch U., Lee S. W., Palmer T. D. (2013) PPARγ activation prevents impairments in spatial memory and neurogenesis following transient illness. *Brain Behav. Immun.* **29**, 28–38.

Paloneva J., Autti T., Raininko R., Partanen J., Salonen O., Puranen M., Hakola P., Haltia M. (2001) CNS manifestations of Nasu-Hakola disease: a frontal dementia with bone cysts. *Neurology* **56**, 1552–1558.

Paloneva J., Manninen T., Christman G., Hovanes K., Mandelin J., Adolfsson R., Bianchin M., et al. (2002) Mutations in Two Genes Encoding Different Subunits of a Receptor Signaling Complex Result in an Identical Disease Phenotype. *Am. J. Hum. Genet.* **71**, 656–662.

Parhizkar S., Arzberger T., Brendel M., Kleinberger G., Deussing M., Focke C., Nuscher B., et al. (2019) Loss of TREM2 function increases amyloid seeding but reduces plaque-associated ApoE. *Nat. Neurosci.* **22**, 191–204.

Parsey M. V., Tuder R. M., Abraham E. (1998) Neutrophils Are Major Contributors to Intraparenchymal Lung IL-1β Expression After Hemorrhage and Endotoxemia. *J. Immunol.* **160**, 1007–1013.

Peters van Ton A. M., Verbeek M. M., Alkema W., Pickkers P., Abdo W. F. (2020) Downregulation of synapse-associated protein expression and loss of

homeostatic microglial control in cerebrospinal fluid of infectious patients with delirium and patients with Alzheimer's disease. *Brain Behav. Immun.* **89**, 656–667.

Poll T. van der, Veerdonk F. L. van de, Scicluna B. P., Netea M. G. (2017) The immunopathology of sepsis and potential therapeutic targets. *Nat. Rev. Immunol.* **17**, 407–420.

Prescott H. C., Angus D. C. (2018) Enhancing Recovery From Sepsis: A Review. *JAMA* **319**, 62–75.

Prescott H. C., Langa K. M., Iwashyna T. J. (2015) Readmission Diagnoses After Hospitalization for Severe Sepsis and Other Acute Medical Conditions. *JAMA* **313**, 1055–1057.

Qin L., Wu X., Block M. L., Liu Y., Breese G. R., Hong J.-S., Knapp D. J., Crews F. T. (2007) Systemic LPS causes chronic neuroinflammation and progressive neurodegeneration. *Glia* **55**, 453–462.

Rautanen A., Mills T. C., Gordon A. C., Hutton P., Steffens M., Nuamah R., Chiche J.-D., et al. (2015) Genome-wide association study of survival from sepsis due to pneumonia: an observational cohort study. *Lancet Respir. Med.* **3**, 53–60.

Reichenberg A., Yirmiya R., Schuld A., Kraus T., Haack M., Morag A., Pollmächer T. (2001) Cytokine-Associated Emotional and Cognitive Disturbances in Humans. *Arch. Gen. Psychiatry* **58**, 445–452.

Rivest S. (2009) Regulation of innate immune responses in the brain. *Nat. Rev. Immunol.* **9**, 429–439.

Rodriguez-Loureiro I., Latza V. M., Fragneto G., Schneck E. (2018) Conformation of Single and Interacting Lipopolysaccharide Surfaces Bearing O-Side Chains. *Biophys. J.* **114**, 1624–1635.

Rooij S. E. de, Munster B. C. van, Korevaar J. C., Levi M. (2007) Cytokines and acute phase response in delirium. *J. Psychosom. Res.* **62**, 521–525.

Rudd K. E., Johnson S. C., Agesa K. M., Shackelford K. A., Tsoi D., Kievlan D. R., Colombara D. V., et al. (2020) Global, regional, and national sepsis incidence and mortality, 1990–2017: analysis for the Global Burden of Disease Study. *Lancet* **395**, 200–211.

Safaiyan S., Kannaiyan N., Snaidero N., Brioschi S., Biber K., Yona S., Edinger A. L., Jung S., Rossner M. J., Simons M. (2016) Age-related myelin degradation burdens the clearance function of microglia during aging. *Nat. Neurosci.* **19**, 995–998.

Saito T., Matsuba Y., Mihira N., Takano J., Nilsson P., Itohara S., Iwata N., Saido T. C. (2014) Single App knock-in mouse models of Alzheimer's disease. *Nat. Neurosci.* **17**, 661–663.

Sandiego C. M., Gallezot J.-D., Pittman B., Nabulsi N., Lim K., Lin S.-F., Matuskey D., et al. (2015) Imaging robust microglial activation after lipopolysaccharide administration in humans with PET. *Proc. Natl. Acad. Sci. U.S.A.* **112**, 12468–12473.

Sauerbeck A. D., Gangolli M., Reitz S. J., Salyards M. H., Kim S. H., Hemingway C., Gratuze M., et al. (2020) SEQUIN Multiscale Imaging of Mammalian Central Synapses Reveals Loss of Synaptic Connectivity Resulting from Diffuse Traumatic Brain Injury. *Neuron* **107**, 257-273.e5.

Savva G. M., Wharton S. B., Ince P. G., Forster G., Matthews F. E., Brayne C. (2009) Age, Neuropathology, and Dementia. *N. Engl. J. Med.* **360**, 2302–2309.

Schafer D. P., Lehrman E. K., Heller C. T., Stevens B. (2014) An Engulfment Assay: A Protocol to Assess Interactions Between CNS Phagocytes and Neurons. *J. Vis. Exp.* 88, 51482.

Schafer D. P., Lehrman E. K., Kautzman A. G., Koyama R., Mardinly A. R., Yamasaki R., Ransohoff R. M., Greenberg M. E., Barres B. A., Stevens B. (2012) Microglia Sculpt Postnatal Neural Circuits in an Activity and Complement-Dependent Manner. *Neuron* **74**, 691–705.

Scheff S. W., Price D. A., Schmitt F. A., DeKosky S. T., Mufson E. J. (2007) Synaptic alterations in CA1 in mild Alzheimer disease and mild cognitive impairment. *Neurology* **68**, 1501–1508.

Schilling T., Eder C. (2015) Microglial K+ Channel Expression in Young Adult and Aged Mice. *Glia* **63**, 664–672.

Schindelin J., Arganda-Carreras I., Frise E., Kaynig V., Longair M., Pietzsch T., Preibisch S., et al. (2012) Fiji: an open-source platform for biological-image analysis. *Nat. Methods.* **9**, 676–682.

Scott-Hewitt N., Perrucci F., Morini R., Erreni M., Mahoney M., Witkowska A., Carey A., et al. (2020) Local externalization of phosphatidylserine mediates developmental synaptic pruning by microglia. *EMBO J.* **39**, e105380.

Semmler A., Frisch C., Debeir T., Ramanathan M., Okulla T., Klockgether T., Heneka M. T. (2007) Long-term cognitive impairment, neuronal loss and reduced cortical cholinergic innervation after recovery from sepsis in a rodent model. *Exp. Neurol.* **204**, 733–740.

Semmler A., Hermann S., Mormann F., Weberpals M., Paxian S. A., Okulla T., Schäfers M., Kummer M. P., Klockgether T., Heneka M. T. (2008) Sepsis causes neuroinflammation and concomitant decrease of cerebral metabolism. *J. Neuroinflammation* **5**, 38.

Semmler A., Widmann C. N., Okulla T., Urbach H., Kaiser M., Widman G., Mormann F., et al. (2013) Persistent cognitive impairment, hippocampal atrophy and EEG changes in sepsis survivors. *J. Neurol. Neurosurg. Psychiatry* **84**, 62–69.

Shah F. A., Pike F., Alvarez K., Angus D., Newman A. B., Lopez O., Tate J., et al. (2013) Bidirectional Relationship between Cognitive Function and Pneumonia. *Am. J. Respir. Crit. Care Med.* **188**, 586–592.

Shalova I. N., Lim J. Y., Chittezhath M., Zinkernagel A. S., Beasley F., Hernández-Jiménez E., Toledano V., et al. (2015) Human monocytes undergo functional re-programming during sepsis mediated by hypoxia-inducible factor-1α. *Immunity* **42**, 484–498.

Sharshar T., Annane D., Grandmaison G. L. de la, Brouland J. P., Hopkinson N. S., Françoise G. (2004) The neuropathology of septic shock. *Brain Pathol.* **14**, 21–33.

Sharshar T., Gray F., Lorin de la Grandmaison G., Hopkinson N. S., Ross E., Dorandeu A., Orlikowski D., Raphael J.-C., Gajdos P., Annane D. (2003) Apoptosis of neurons in cardiovascular autonomic centres triggered by inducible nitric oxide synthase after death from septic shock. *Lancet* **362**, 1799–1805.

Shi Q., Colodner K. J., Matousek S. B., Merry K., Hong S., Kenison J. E., Frost J. L., et al. (2015) Complement C3-Deficient Mice Fail to Display Age-Related Hippocampal Decline. *J. Neurosci.* **35**, 13029–13042.

Shoji H., Takao K., Hattori S., Miyakawa T. (2016) Age-related changes in behavior in C57BL/6J mice from young adulthood to middle age. *Mol. Brain* **9**, 11.

Sims R., Lee S. J. van der, Naj A. C., Bellenguez C., Badarinarayan N., Jakobsdottir J., Kunkle B. W., et al. (2017) Rare coding variants in PLCG2, ABI3 and TREM2 implicate microglial-mediated innate immunity in Alzheimer's disease. *Nat. Genet.* **49**, 1373–1384.

Singer B. H., Newstead M. W., Zeng X., Cooke C. L., Thompson R. C., Singer K., Ghantasala R., et al. (2016a) Cecal Ligation and Puncture Results in Long-Term Central Nervous System Myeloid Inflammation. *PLoS One* **11**, e0149136.

Singer M., Deutschman C. S., Seymour C. W., Shankar-Hari M., Annane D., Bauer M., Bellomo R., et al. (2016b) The Third International Consensus Definitions for Sepsis and Septic Shock (Sepsis-3). *JAMA* **315**, 801–810.

Singh-Manoux A., Dugravot A., Brunner E., Kumari M., Shipley M., Elbaz A., Kivimaki M. (2014) Interleukin-6 and C-reactive protein as predictors of cognitive decline in late midlife. *Neurology* **83**, 486–493.

Song E., Zhang C., Israelow B., Lu-Culligan A., Prado A. V., Skriabine S., Lu P., et al. (2021) Neuroinvasion of SARS-CoV-2 in human and mouse brain. *J. Exp. Med.* **218**, e20202135.

Sonneville R., Montmollin E. de, Poujade J., Garrouste-Orgeas M., Souweine B., Darmon M., Mariotte E., et al. (2017) Potentially modifiable factors contributing to sepsis-associated encephalopathy. *Intensive Care Med.* **43**, 1075–1084.

Sonneville R., Verdonk F., Rauturier C., Klein I. F., Wolff M., Annane D., Chretien F., Sharshar T. (2013) Understanding brain dysfunction in sepsis. *Ann. Intensive Care* **3**, 15.

Southeast Asia Infectious Disease Clinical Research Network (2017) Causes and outcomes of sepsis in southeast Asia: a multinational multicentre cross-sectional study. *Lancet Glob. Health* **5**, e157–e167.

Spangenberg E. E., Lee R. J., Najafi A. R., Rice R. A., Elmore M. R. P., Blurton-Jones M., West B. L., Green K. N. (2016) Eliminating microglia in Alzheimer's mice prevents neuronal loss without modulating amyloid-β pathology. *Brain* **139**, 1265–1281.

Sparkman N. L., Buchanan J. B., Heyen J. R. R., Chen J., Beverly J. L., Johnson R. W. (2006) Interleukin-6 Facilitates Lipopolysaccharide-Induced Disruption in Working Memory and Expression of Other Proinflammatory Cytokines in Hippocampal Neuronal Cell Layers. *J. Neurosci.* **26**, 10709–10716.

Stephan A. H., Madison D. V., Mateos J. M., Fraser D. A., Lovelett E. A., Coutellier L., Kim L., et al. (2013) A Dramatic Increase of C1q Protein in the CNS during Normal Aging. *J. Neurosci.* **33**, 13460–13474.

Stevens B., Allen N. J., Vazquez L. E., Howell G. R., Christopherson K. S., Nouri N., Micheva K. D., et al. (2007) The classical complement cascade mediates CNS synapse elimination. *Cell* **131**, 1164–1178.

Stortz J. A., Mira J. C., Raymond S. L., Loftus T. J., Ozrazgat-Baslanti T., Wang Z., Ghita G. L., et al. (2018) Benchmarking clinical outcomes and the immunocatabolic phenotype of chronic critical illness after sepsis in surgical intensive care unit patients. *J. Trauma Acute Care Surg.* **84**, 342–349.

Stubbs D. J., Yamamoto A. K., Menon D. K. (2013) Imaging in sepsis-associated encephalopathy--insights and opportunities. *Nat. Rev. Neurol.* **9**, 551–561.

Taveira da Silva A. M., Kaulbach H. C., Chuidian F. S., Lambert D. R., Suffredini A. F., Danner R. L. (1993) Brief report: shock and multiple-organ dysfunction

after self-administration of Salmonella endotoxin. *N. Engl. J. Med.* **328**, 1457–1460.

Tejera D., Mercan D., Sanchez-Caro J. M., Hanan M., Greenberg D., Soreq H., Latz E., Golenbock D., Heneka M. T. (2019) Systemic inflammation impairs microglial Aβ clearance through NLRP3 inflammasome. *EMBO J.* **38**, e101064.

Terry R. D., Masliah E., Salmon D. P., Butters N., DeTeresa R., Hill R., Hansen L. A., Katzman R. (1991) Physical basis of cognitive alterations in alzheimer's disease: Synapse loss is the major correlate of cognitive impairment. *Ann. Neurol.* **30**, 572–580.

Tremblay M.-È., Lowery R. L., Majewska A. K. (2010) Microglial interactions with synapses are modulated by visual experience. *PLoS Biol.* **8**, e1000527.

Vanhaute H., Ceccarini J., Michiels L., Koole M., Sunaert S., Lemmens R., Triau E., Emsell L., Vandenbulcke M., Laere K. V. (2020) In vivo synaptic density loss is related to tau deposition in amnestic mild cognitive impairment. *Neurology* **95**, e545–e553.

Varatharaj A., Galea I. (2017) The blood-brain barrier in systemic inflammation. *Brain Behav. Immun.* **60**, 1–12.

Veerhuis R., Nielsen H. M., Tenner A. J. (2011) Complement in the brain. *Mol. Immunol.* **48**, 1592–1603.

Venegas C., Heneka M. T. (2017) Danger-associated molecular patterns in Alzheimer's disease. *J. Leukoc. Biol.* **101**, 87–98.

Venegas C., Kumar S., Franklin B. S., Dierkes T., Brinkschulte R., Tejera D., Vieira-Saecker A., et al. (2017) Microglia-derived ASC specks cross-seed amyloid-β in Alzheimer's disease. *Nature* **552**, 355–361.

Viggiano D., Wagner C. A., Martino G., Nedergaard M., Zoccali C., Unwin R., Capasso G. (2020) Mechanisms of cognitive dysfunction in CKD. *Nat. Rev. Nephrol.* **16**, 452–469.

Vincent J. L., Moreno R., Takala J., Willatts S., De Mendonça A., Bruining H., Reinhart C. K., Suter P. M., Thijs L. G. (1996) The SOFA (Sepsis-related Organ Failure Assessment) score to describe organ dysfunction/failure. On behalf of the Working Group on Sepsis-Related Problems of the European Society of Intensive Care Medicine. *Intensive Care Med.* **22**, 707–710.

Walton A. H., Muenzer J. T., Rasche D., Boomer J. S., Sato B., Brownstein B. H., Pachot A., et al. (2014) Reactivation of Multiple Viruses in Patients with Sepsis. *PLoS One* **9**, e98819.

Wang Y., Cella M., Mallinson K., Ulrich J. D., Young K. L., Robinette M. L., Gilfillan S., et al. (2015) TREM2 Lipid Sensing Sustains the Microglial Response in an Alzheimer's Disease Model. *Cell* **160**, 1061–1071.

Wang Y., Ulland T. K., Ulrich J. D., Song W., Tzaferis J. A., Hole J. T., Yuan P., et al. (2016) TREM2-mediated early microglial response limits diffusion and toxicity of amyloid plaques. *J. Exp. Med.* **213**, 667–675.

Wardlaw J. M., Makin S. J., Valdés Hernández M. C., Armitage P. A., Heye A. K., Chappell F. M., Muñoz-Maniega S., et al. (2017) Blood-brain barrier failure as a core mechanism in cerebral small vessel disease and dementia: evidence from a cohort study. *Alzheimers. Dement.* **13**, 634–643.

Weberpals M., Hermes M., Hermann S., Kummer M. P., Terwel D., Semmler A., Berger M., Schäfers M., Heneka M. T. (2009) NOS2 gene deficiency protects from sepsis-induced long-term cognitive deficits. *J. Neurosci.* **29**, 14177–14184.

Weinhard L., Bartolomei G. di, Bolasco G., Machado P., Schieber N. L., Neniskyte U., Exiga M., et al. (2018) Microglia remodel synapses by presynaptic trogocytosis and spine head filopodia induction. *Nat. Commun.* **9**, 1228.

Wendeln A.-C., Degenhardt K., Kaurani L., Gertig M., Ulas T., Jain G., Wagner J., et al. (2018) Innate immune memory in the brain shapes neurological disease hallmarks. *Nature* **556**, 332–338.

West M. J. (1993) Regionally specific loss of neurons in the aging human hippocampus. *Neurobiol. Aging* **14**, 287–293.

West M. J., Gundersen H. J. G. (1990) Unbiased stereological estimation of the number of neurons in the human hippocampus. *J. Comp. Neurol.* **296**, 1–22.

Whitfield C., Williams D. M., Kelly S. D. (2020) Lipopolysaccharide O-antigens—bacterial glycans made to measure. *J. Biol. Chem* **295**, 10593–10609.

Widmann C. N., Heneka M. T. (2014) Long-term cerebral consequences of sepsis. *Lancet Neurol.* **13**, 630–636.

Wijasa T. S., Sylvester M., Brocke-Ahmadinejad N., Schwartz S., Santarelli F., Gieselmann V., Klockgether T., Brosseron F., Heneka M. T. (2020) Quantitative proteomics of synaptosome S-nitrosylation in Alzheimer's disease. *J. Neurochem.* **152**, 710–726.

Wu L., Feng Q., Ai M.-L., Deng S., Liu Z.-Y., Huang L., Ai Y.-H., Zhang L. (2020) The dynamic change of serum S100B levels from day 1 to day 3 is more associated with sepsis-associated encephalopathy. *Sci. Rep.* **10**, 7718.

Xia D., Lianoglou S., Sandmann T., Calvert M., Suh J. H., Thomsen E., Dugas J., et al. (2021) Fibrillar Aβ causes profound microglial metabolic perturbations in a novel APP knock-in mouse model. *bioRxiv*.

Yang D., He Y., Muñoz-Planillo R., Liu Q., Núñez G. (2015) Caspase-11 Requires the Pannexin-1 Channel and the Purinergic P2X7 Pore to Mediate Pyroptosis and Endotoxic Shock. *Immunity* **43**, 923–932.

Yang Y., Zhang P., Lv R., He Q., Zhu Y., Yang X., Chen J. (2011) Mitochondrial DNA haplogroup R in the Han population and recovery from septic encephalopathy. *Intensive Care Med.* **37**, 1613–1619.

Yende S., Kellum J. A., Talisa V. B., Peck Palmer O. M., Chang C.-C. H., Filbin M. R., Shapiro N. I., et al. (2019) Long-term Host Immune Response Trajectories Among Hospitalized Patients With Sepsis. *JAMA Netw. Open* **2**, e198686.

Yirmiya R., Goshen I. (2011) Immune modulation of learning, memory, neural plasticity and neurogenesis. *Brain Behav. Immun.* **25**, 181–213.

Yoshiyama Y., Higuchi M., Zhang B., Huang S.-M., Iwata N., Saido T. C., Maeda J., Suhara T., Trojanowski J. Q., Lee V. M.-Y. (2007) Synapse loss and microglial activation precede tangles in a P301S tauopathy mouse model. *Neuron* **53**, 337–351.

Youm Y.-H., Grant R. W., McCabe L. R., Albarado D. C., Nguyen K. Y., Ravussin A., Pistell P., et al. (2013) Canonical Nlrp3 inflammasome links systemic low-grade inflammation to functional decline in aging. *Cell Metab.* **18**, 519–532.

Youm Y.-H., Kanneganti T.-D., Vandanmagsar B., Zhu X., Ravussin A., Adijiang A., Owen J. S., et al. (2012) The NLRP3 Inflammasome Promotes Age-Related Thymic Demise and Immunosenescence. *Cell Rep.* **1**, 56–68.

Young K., Morrison H. (2018) Quantifying Microglia Morphology from Photomicrographs of Immunohistochemistry Prepared Tissue Using ImageJ. *J. Vis. Exp.* 136.

Yuan P., Condello C., Keene C. D., Wang Y., Bird T. D., Paul S. M., Luo W., Colonna M., Baddeley D., Grutzendler J. (2016) TREM2 Haplodeficiency in

Mice and Humans Impairs the Microglia Barrier Function Leading to Decreased Amyloid Compaction and Severe Axonal Dystrophy. *Neuron* **90**, 724–739.

Zhang S., Wang X., Ai S., Ouyang W., Le Y., Tong J. (2017) Sepsis-induced selective loss of NMDA receptors modulates hippocampal neuropathology in surviving septic mice. *PLoS One* **12**, e0188273.

Zhou F., Yu T., Du R., Fan G., Liu Y., Liu Z., Xiang J., et al. (2020) Clinical course and risk factors for mortality of adult inpatients with COVID-19 in Wuhan, China: a retrospective cohort study. *Lancet* **395**, 1054–1062.

Zrzavy T., Höftberger R., Berger T., Rauschka H., Butovsky O., Weiner H., Lassmann H. (2019) Pro-inflammatory activation of microglia in the brain of patients with sepsis. *Neuropathol. Appl. Neurobiol.* **45**, 278–290.

Acknowledgements

Firstly and foremost, I would like to express the sincerest gratitude to my supervisor Prof Michael Heneka for providing the opportunity to work with his team throughout the PhD project.

Secondly, I would like to thank Dr Ildikó Rácz for her support from the beginning to the end of my PhD by designing the experiments, reviewing the manuscripts and writing the experiment allowance for this project. My sincerest gratitude also goes to my collaborators, Dr Jonas Neher and Dr Julius Emmrich, for their insightful discussions throughout this project and for reviewing the manuscript. I would like to acknowledge Dr Christina Ising and Ms Stephanie Schwartz for reviewing the experiment allowance and providing their patient supports.

Furthermore, my colleagues kindly supported me during this doctoral study. I would particularly like to thank Dr Nàdia Villacampa-Pérez and Dr Sergio Castro-Gomez for all the stimulating discussions and technical feedbacks. I would also like to acknowledge Ms Ana Vieira-Saecker, Mr Francesco Santarelli, Ms Paula Martorell and Mr Deniz Karabag for their technical supports for analysis and experiments.

I am also thankful to Dr Hannes Beckert in the Microscopy Core Facility at the Medical Faculty of the University of Bonn and Dr Hans Fried in the Light Microscope Facility at DZNE for their continuous supports to use the microscopes and analysis software.

Last but not least, I would like to thank my parents for their unconditional support and belief to allow me to pursue a scientific career.